UNIVERSITY OF ROCHESTER
LABORATORY FOR LASER ENERGETICS

Volume 76
July–September 1998
DOE/SF/19460-264

LLE Review

Quarterly Report

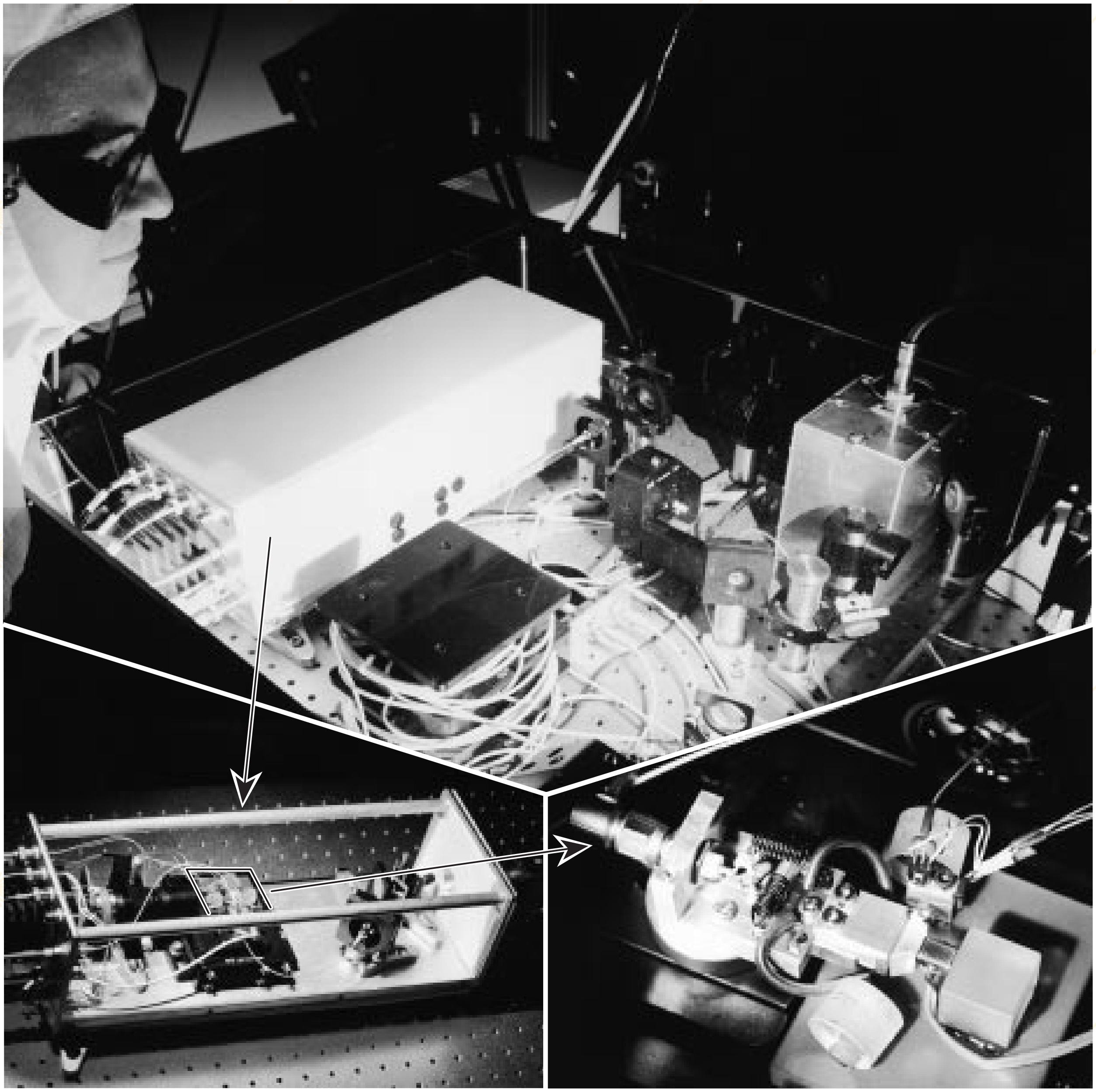

About the Cover:

Scientist Andrey Okishev is shown examining the new diode-pumped master oscillator for the OMEGA laser system. The master oscillator, including the pump-laser diode, the conditioning optics, the Nd:YLF laser, the amplitude feedback pickoff, and the thermal stabilization systems, is housed in the large white thermally insulated box seen closed near the left side of the picture and open in the lower left inset. The holes in the optical table form a one-inch grid, which serves as a scale. The main components of the diode-pumped laser are shown magnified in the lower right inset. One can see the cavity mirrors, the thermally stabilized active element, the acousto-optic modulator, and a prism mounted on the piezoelectric translator. These key elements are recognizable in the corresponding block diagram in the lead article of this volume, where the oscillator is described in detail.

The work described in this volume includes current research at the Laboratory for Laser Energetics, which is supported by New York State Energy Research and Development Authority, the University of Rochester, the U.S. Department of Energy Office of Inertial Confinement Fusion under Cooperative Agreement No. DE-FC03-92SF19460, and other agencies.

Printed in the United States of America
Available from
National Technical Information Services
U.S. Department of Commerce
5285 Port Royal Road
Springfield, VA 22161

Price codes: Printed Copy A04
Microfiche A01

For questions or comments, contact Reuben Epstein, *Editor*, Laboratory for Laser Energetics, 250 East River Road, Rochester, NY 14623-1299, (716) 275-5405.

Worldwide-Web Home Page: http://www.lle.rochester.edu/

UNIVERSITY OF ROCHESTER
LABORATORY FOR LASER ENERGETICS

Volume 76
July–September 1998
DOE/SF/19460-264

LLE Review

Quarterly Report

Contents

In Brief

This volume of the LLE Review, covering the period July–September 1998, includes reports on two of the newest subsystems in the OMEGA laser facility. A. V. Okishev, M. D. Skeldon, and W. Seka have developed a highly stable, diode-pumped Nd:YLF master oscillator for the OMEGA laser system. This new master oscillator produces either single-frequency *Q*-switched pulses or cw radiation for the OMEGA pulse-shaping system. The switch-over between these two regimes requires no laser realignment. The new master oscillator is completely computer controlled and has been operating continuously in OMEGA for six months without operator intervention. A. Babushkin, W. Bittle, S. A. Letzring, M. D. Skeldon, and W. Seka have designed a negative-feedback–controlled regenerative amplifier that has been part of the OMEGA laser system for the past two years. The negative feedback makes the energy output of the regenerative amplifier stable and insensitive to the variations in pulse energy. This amplifier's long-term output energy stability is the highest ever demonstrated for a millijoule-level laser system, either flashlamp pumped or diode pumped.

Additional research highlights reported in this issue are

- K. Green, W. Donaldson, R. Keck, A. V. Okishev, M. D. Skeldon, W. Seka, and R. Sobolewski have expanded the pulse-shape bandwidth of OMEGA's driver line from approximately 3 GHz to over 5 GHz by using a novel measurement scheme that takes into account the transient carrier dynamics of the photoconductive switches used in the pulse-shaping subsystem.

- J. Marozas has performed calculations of near-field intensity modulations in high-intensity laser beams due to self- and cross-phase modulation between the orthogonally polarized laser beams emerging from KDP wedges placed into the OMEGA laser beamlines. Such wedges produce a reduction in the far-field speckle nonuniformity by polarization smoothing and are not expected to be a significant source of intensity modulation under expected operating conditions.

- V. A. Smalyuk, T. R. Boehly, D. K. Bradley, J. P. Knauer, and D. D. Meyerhofer have characterized an x-ray radiographic system for measuring mass modulations in planar laser-driven targets. Using the known sensitivity, resolution, and noise characteristics of this system, they have formulated a Wiener filter that reduces noise, compensates for detector resolution, and facilitates measurement of perturbations imprinted on targets by laser nonuniformity.

- R. W. Short and A. Simon have found a plausible explanation for observations of stimulated Raman scattering (SRS) that have been at odds with theoretical predictions. By calculating the collisionless damping rate of plasma waves confined within a small cylinder, they have found that plasma waves confined within small-radius filaments damp much more slowly than plane plasma waves in a homogeneous plasma. Predictions using these corrected rates, rather than rates obtained using the usual Landau theory for plane waves in homogeneous plasmas, provide a viable explanation of the anomalous SRS observations.

- This volume concludes with the Summer High School Program Report, the Laser Facility Report, and the National Laser Users' Facility News.

Reuben Epstein
Editor

Highly Stable, Diode-Pumped Master Oscillator for the OMEGA Laser Facility

The OMEGA facility is a 60-beam, 30-kJ (UV) laser system for performing inertial confinement fusion (ICF) experiments. One of the main features of the OMEGA laser is an optical pulse–shaping system capable of producing flexible temporal pulse shapes[1] (Fig. 76.1). The recently developed diode-pumped Nd:YLF master oscillator[2] is capable of satisfying the basic OMEGA requirements, such as single-frequency, long-pulse, *Q*-switched operation with high amplitude stability. Some OMEGA operational issues (modulator minimization procedures, bandwidth characterization, increased repetition rate, and temporal diagnostic calibration), however, have motivated the development of a new diode-pumped, multipurpose laser. The new laser is capable of serving as the OMEGA master oscillator (stable, single-frequency, *Q*-switched operation), as well as a source of stable, single-frequency cw radiation (for modulator characterization and minimization) and stable, sinusoidally modulated radiation (for temporal diagnostics calibration).

OMEGA Pulse-Shaping System

The heart of the OMEGA optical pulse–shaping system is an integrated-optic (IO) modulator. To obtain high-contrast, high-precision, shaped optical pulses, the modulator must be biased to provide zero transmission in the absence of an electrical waveform (modulator minimization procedure). To accomplish this on OMEGA, cw laser radiation from a different laser source than the master oscillator (the cw mode-locked laser) is manually directed to the modulator. This operator intervention is time consuming and places unnecessary stress on fiber-optic connectors and components. This operator intervention is eliminated with a master oscillator that can be easily switched to cw operation.

By increasing the laser repetition rate in *Q*-switched operation, precision pulse-shape and bandwidth measurements can be made with a high-bandwidth sampling oscilloscope. In addition, with careful laser-cavity-length control the laser can

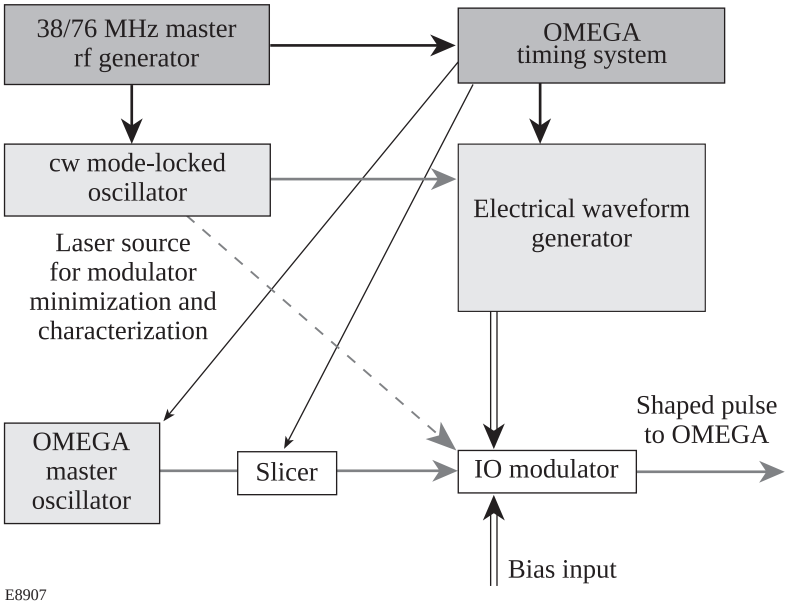

Figure 76.1
Block diagram of the OMEGA pulse-shaping system.

lase simultaneously on two adjacent cavity modes and provide a precise, temporally modulated signal for temporal diagnostics calibration (streak cameras, photodetectors, etc.).

Laser Characteristics

The basic design of the laser (Fig. 76.2) is similar to the one described earlier.[2] As a pump source we have chosen a single-stripe, 1.2-W, cw SDL-2326-P1 laser diode (a modification from the previous design) with a thermoelectric cooler that eliminates the need for water cooling. The diode wavelength is temperature tuned to 797 nm to provide maximum pump absorption in the active element. The polarization of the pump radiation is parallel to the *c*-axis of the active element, which increases pump absorption to approximately 80%.

Beam-conditioning optics for the diodes consist of an AR-coated aspherical lens (NA~0.68) and an AR-coated cylindrical lens. The pump radiation is focused into the active element through the dichroic end mirror. Transmission of the conditioning optics, focusing lens, and dichroic mirror is ~90% at 797 nm. The active element is a 4-mm-diam by 5-mm, 1.1% Nd:YLF wedged and AR-coated rod oriented with the Brewster prism to provide 1053-nm lasing. The acousto-optic modulator (AOM) used as *Q*-switch (GOOCH & HOUSEGO, QS080-2G-RU2) is wedged and AR coated for 1053 nm. In the cw operation regime (no rf power applied to the AOM) the laser generates a total of 260 mW of cw power (in both counter-propagating beams) with an optical-to-optical efficiency >21% at 1053 nm (Fig. 76.3).

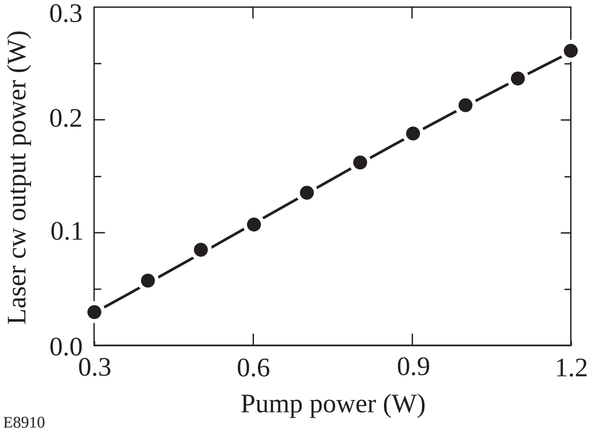

Figure 76.3
Laser cw output power versus diode pump power for bidirectional operation.

Unidirectional single-frequency operation is achieved by applying a low (<200-mW) rf power to the AOM.[3] By removing the rf power from the AOM we obtain *Q*-switched, 50- to 200-ns (FWHM) pulses [Fig. 76.4(a)] at a repetition rate of up to 10 kHz. The energy content of the sliced, flat-top portion of the pulse [Fig. 76.4(b)] is 0.2 to 1.5 μJ, depending on the pulse width. Without removing the rf power to the AOM (*Q*-switch trigger off), the laser generates up to 100 mW of single-frequency cw power (optical-to-optical efficiency is ~13%).

The spatial laser beam profile is close to TEM$_{00}$ and is launched into a single-mode optical fiber delivery system for all our applications. We routinely achieve a single-mode fiber launching efficiency of the order of 85%, which indicates a high-quality beam profile.

Laser Parameter Control and Stabilization

To achieve single-frequency, highly stable (in terms of amplitude, timing jitter, wavelength) laser operation we employ several feedback loops:

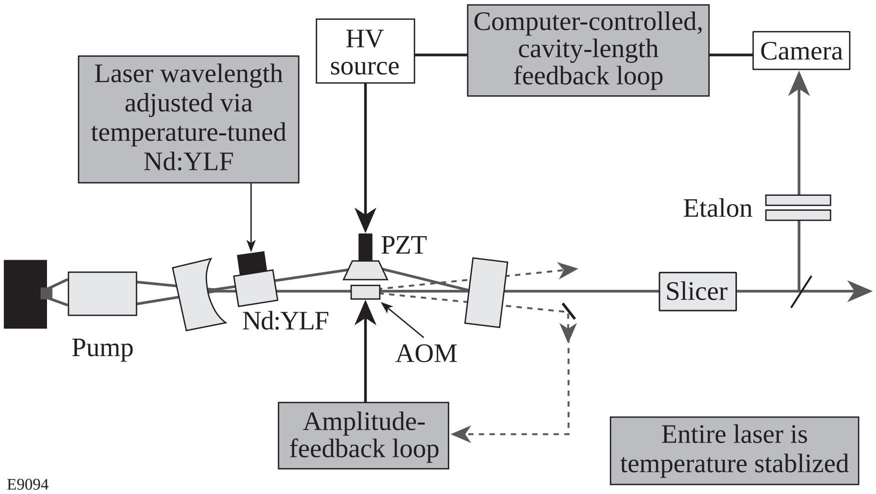

Figure 76.2
Block diagram of the multipurpose Nd:YLF laser.

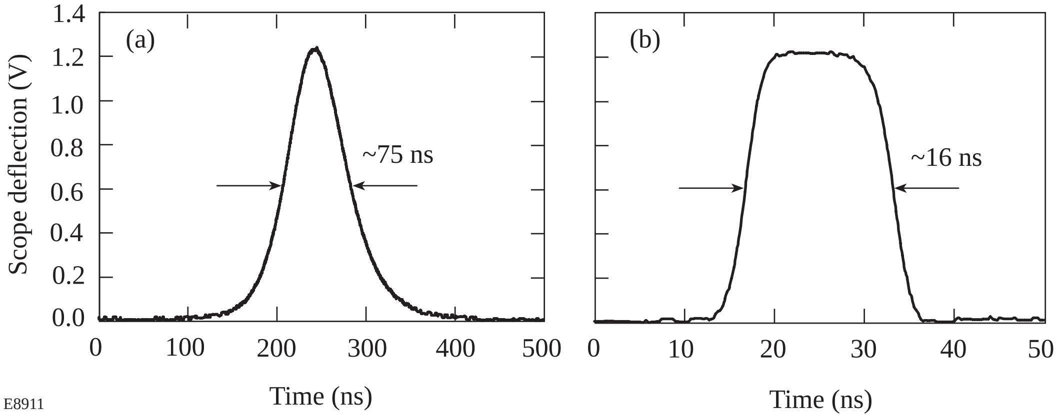

Figure 76.4
(a) The *Q*-switched pulse envelope and (b) sliced central flat-top portion of the pulse to be sent to the modulator.

- amplitude-feedback loop
- wavelength control and stabilization
- frequency-feedback loop
- overall laser temperature stabilization
- two-mode operation

1. Amplitude-Feedback Loop

To damp relaxation oscillations and stabilize the prelase phase, the rf power applied to the AOM is controlled with a circuit that provides negative amplitude feedback. One of the beams diffracted by the AOM is coupled into a 0.4-mm multimode fiber and sent to a diode that generates a feedback signal (Fig. 76.2). For a high (low) feedback signal the rf power to the AOM is increased (decreased), thus increasing (decreasing) the cavity losses and stabilizing the cw laser output power. With amplitude-feedback stabilization, a very smooth prelase phase with no relaxation oscillations is observed (Fig. 76.5), and the externally triggerable *Q*-switch leads to high amplitude stability and low temporal jitter of the output pulse. Amplitude fluctuations of the *Q*-switched pulse are 0.5% rms and the timing jitter is 3 to 5 ns rms depending on the *Q*-switched optical pulse duration.

2. Wavelength Control and Stabilization

Due to the large longitudinal mode spacing and the absence of wavelength-tuning elements (such as etalons, gratings, etc.) the laser is operating at the peak of the gain curve; thus, the only way to adjust and stabilize the lasing wavelength is to adjust the peak position of the Nd:YLF gain curve by changing and stabilizing the temperature of the active element. The operating temperature of the active element is 34°C to 36°C with no temperature control. Adjustment of the laser wavelength for OMEGA requires additional heating up to 39°C to 45°C. We have developed a miniaturized heater–sensor feedback loop that is mounted on the active element heat sink and can maintain its temperature to within 0.1°C. Figure 76.6 shows the wavelength tuning and stabilization by adjusting and maintaining the temperature of the active element. We have found the thermal wavelength coefficient $\Delta\lambda/\Delta T$ to be +0.08 Å/°C.

3. Frequency-Feedback Loop and Overall Temperature Stabilization

To ensure single-frequency operation we have developed a computerized wavelength-feedback loop. The laser spectrum is measured with an air-spaced etalon and analyzed by a computer equipped with a CCD camera and framegrabber. If the fringe peak moves, the computer produces a driving voltage to change the high voltage on the piezoelectric translator (PZT)

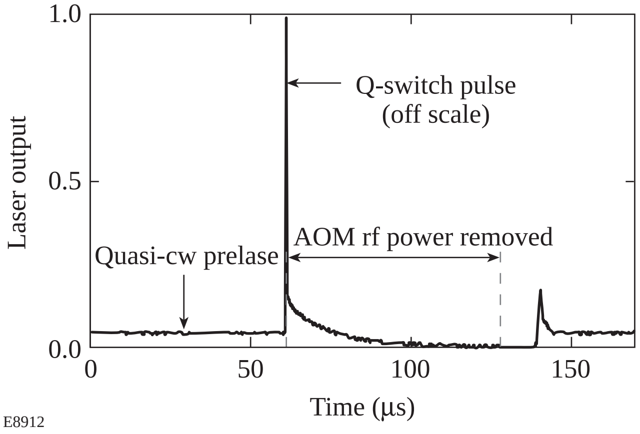

Figure 76.5
Amplitude feedback provides constant prelase for higher amplitude stability of the *Q*-switched pulse with lower timing jitter.

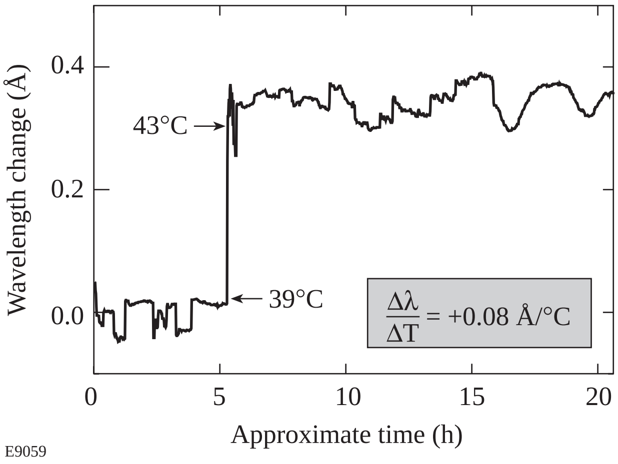

Figure 76.6
The laser output wavelength is adjusted and stabilized by controlling the temperature of the active element.

to correct the laser cavity length and bring the fringe peak to its initial position. The following procedure locates the correct fringe position (reset): The computer scans the PZT driver voltage until the two-mode operation is detected; it then reverses the scan to find the next two-mode operation voltage; and finally, it sets the voltage between these two-mode operation voltages. This reset procedure is repeated every 0.5 h and ensures single-frequency operation [Fig. 76.7(a)]. The thermal drift due to room-temperature changes, however, causes an undesirable wavelength drift. When the laser housing and active element are temperature stabilized [Fig. 76.7(b)], the laser runs single frequency with a residual wavelength drift of 0.01 Å rms over 15 h of operation (Fig. 76.8).

We have taken the envelope of the sliced flat-top pulse using a 20-ps-resolution streak camera. This envelope is extremely smooth (Fig. 76.9), indicating a high single-frequency contrast.

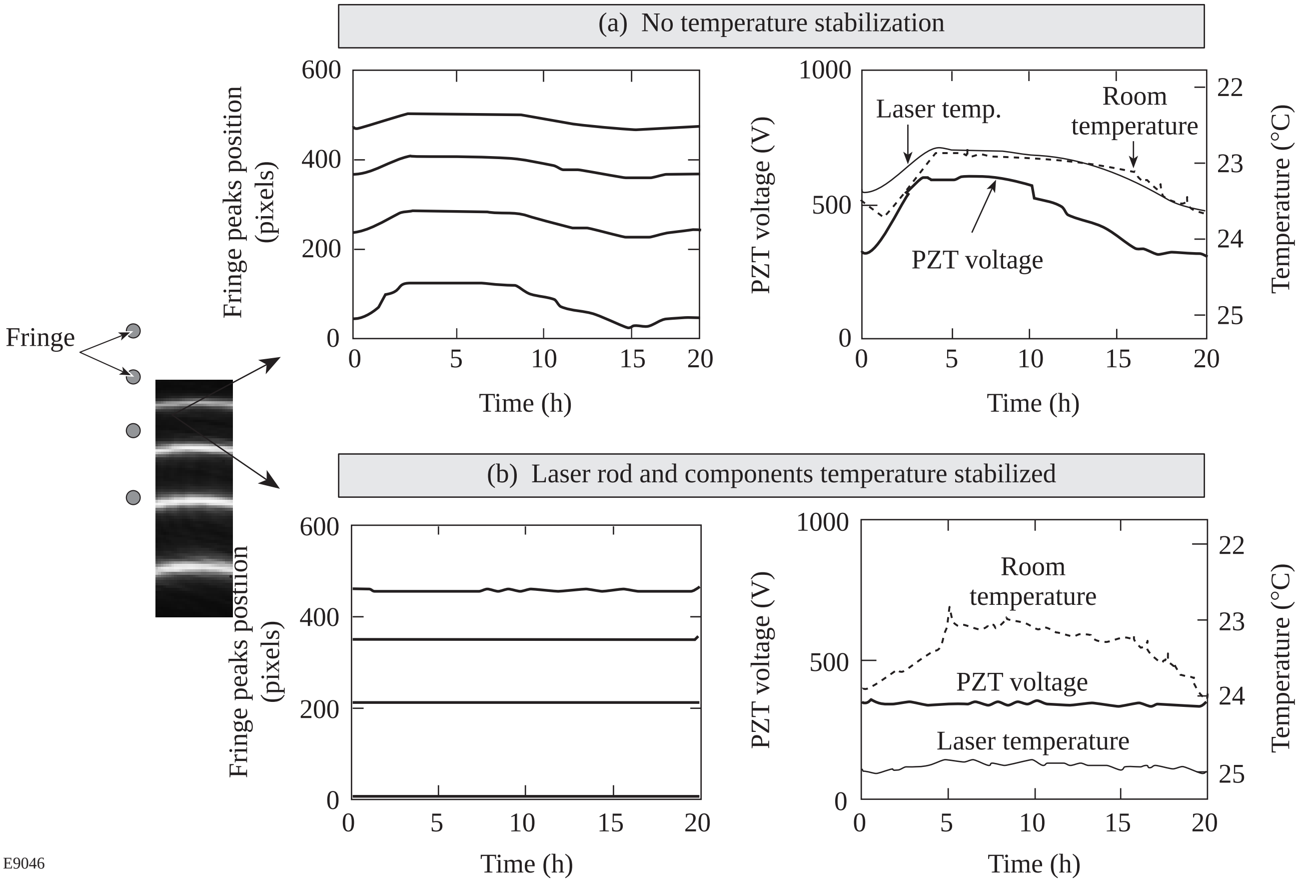

Figure 76.7
The laser operates with a single frequency; however, with no temperature stabilization the frequency drifts over time and follows the room temperature (a). Temperature stabilization of the active element and laser components significantly improves wavelength stability (b).

4. Two-Mode Operation

By applying the appropriate computer-controlled feedback to the PZT-mounted prism in the laser cavity, the laser can be forced to operate over many hours on two adjacent longitudinal modes with approximately equal amplitudes [Fig. 76.10(a)]. In this case the pulse's temporal structure is a deeply modulated sinusoidal signal with a 267-ps period [Fig. 76.10(b)]. This signal can be particularly useful for OMEGA temporal diagnostics calibration such as streak camera sweep speeds, etc.

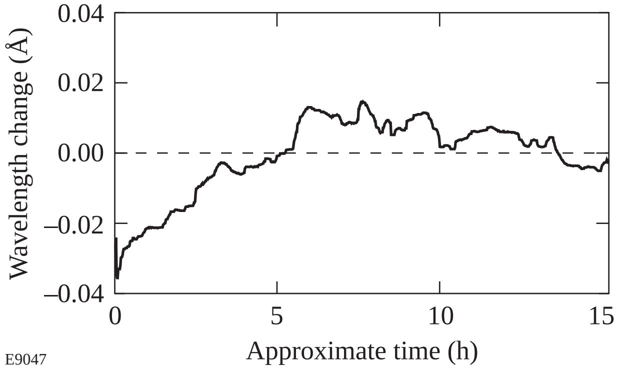

Figure 76.8
The laser wavelength stability is 0.01 Å over 15 h.

Conclusion

We have developed a diode-pumped, multipurpose Nd:YLF laser for the OMEGA laser facility that is suitable for our pulse-shaping applications, including modulator minimization and characterization, as well as temporal diagnostics calibration. The laser combines three functions without realignment:

- *Q*-switched, single-frequency master oscillator for the OMEGA laser,
- cw single-frequency operation for pulse-shaping applications, and
- the source of a stable sinusoidal optical signal for diagnostics applications.

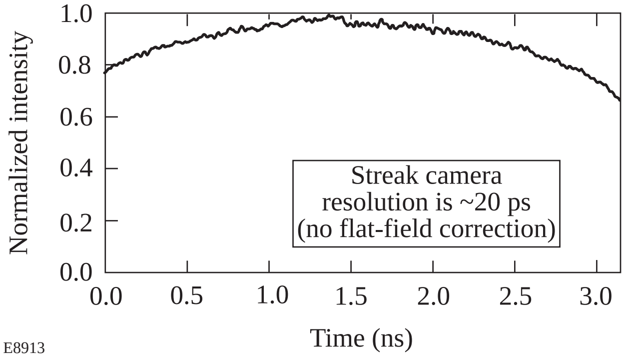

Figure 76.9
Streak camera measurement of the pulse envelope (no flat-field correction) showing high single-frequency contrast.

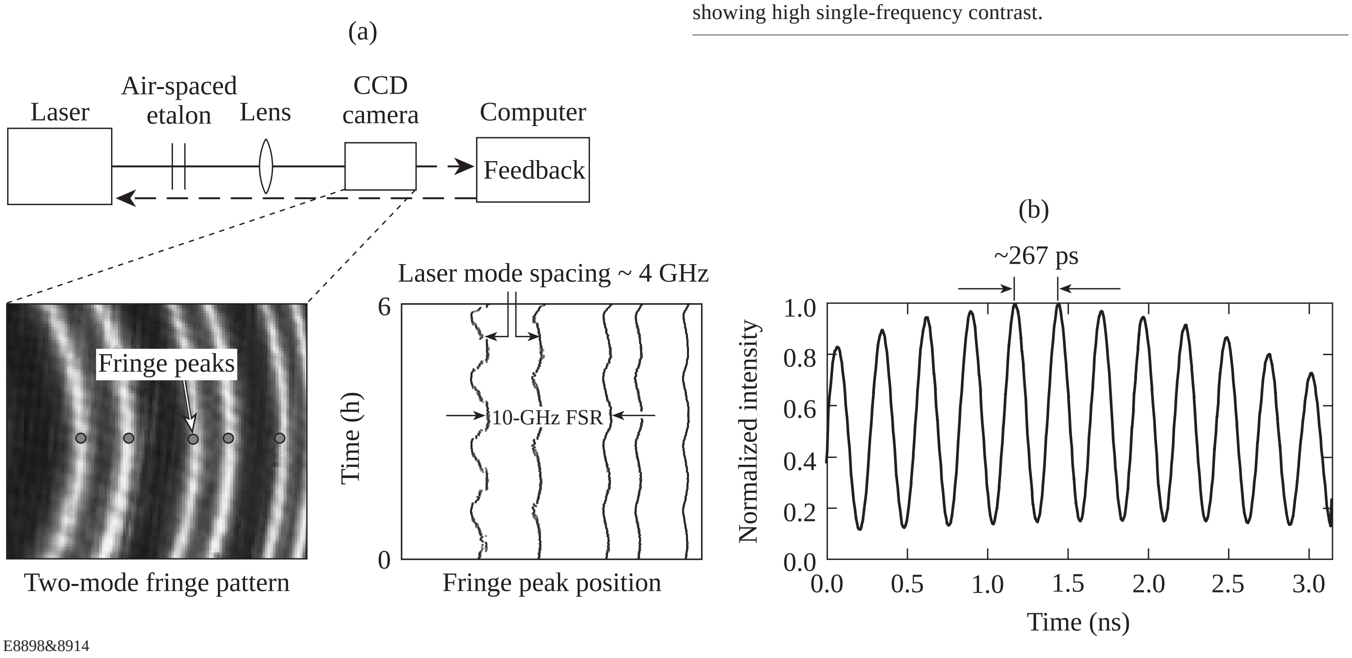

Figure 76.10
(a) Long-term, two-mode operation and (b) streak camera measurement of the optical sinusoidal signal (no flat-field correction).

The laser output is either up to 100 mW of cw single-frequency radiation or *Q*-switched pulses with a smooth or sinusoidally modulated envelope at a repetition rate of ≤10 kHz. Changeover requires no laser realignment.

ACKNOWLEDGMENT

This work was supported by the U.S. Department of Energy Office of Internal Confinement Fusion under Cooperative Agreement No. DE-FC03-92SF19460 and the University of Rochester. The support of DOE does not constitute an endorsement by DOE of the views expressed in this article.

REFERENCES

1. A. V. Okishev, W. Seka, J. H. Kelly, S. F. B. Morse, J. M. Soures, M. D. Skeldon, A. Babushkin, R. L. Keck, and R. G. Roides, in *Conference on Lasers and Electro-Optics*, Vol. 11, 1997 OSA Technical Digest Series (Optical Society of America, Washington, DC, 1997), p. 389.
2. A. V. Okishev and W. Seka, IEEE J. Sel. Top. Quantum Electron. **3**, 59 (1997).
3. W. A. Clarkson, A. B. Neilson, and D. C. Hanna, IEEE J. Quantum Electron. **32**, 311 (1996).

Regenerative Amplifier for the OMEGA Laser System

The 60-beam OMEGA Nd:glass laser is a direct-drive inertial confinement fusion (ICF) laser facility capable of achieving 30-kJ UV energy with an arbitrary temporal pulse shape predetermined by the target design. The initial low-energy, temporally shaped pulse is generated by the pulse-shaping system[1] (similar to a design developed at the Lawrence Livermore National Laboratory[2]), followed by multistage amplification with splitting, resulting in 60 laser beams with 1-kJ IR energy per beam. At the first amplification stage a negative-feedback-controlled, Nd:YLF regenerative amplifier (regen) is used. In this regen, the shaped pulse is amplified up to nine orders of magnitude to the submillijoule level.

In this article we present the requirements, design, and experimental results for the regens currently in use on OMEGA. These externally synchronizable regens boost the energy of the temporally shaped pulses to the submillijoule level with long-term energy variations of ~0.2% and with the output parameters of the amplified pulse insensitive to the injected pulse energy. The temporal distortions of the amplified pulse caused by the negative feedback are immeasurable. Four regenerative amplifiers equipped with this negative feedback system have operated flawlessly on OMEGA for the past two years.

Regenerative Amplifier Requirements for the OMEGA Laser System

The pulse-shaping system on OMEGA must meet a number of specifications[3] with a large safety margin to allow stable and reliable OMEGA operation. The low-energy pulses generated by this system must be amplified to an ~400-μJ energy with better-than-2% stability; the output pulses must be externally synchronizable; and the amplification process should introduce minimum and predictable temporal-pulse-shape distortions.

Multipass regens have been shown to provide high gains.[4,5] Flash-lamp-pumped regens, however, have typical output energy fluctuations[5,6] in the range of 5% to 10% for externally synchronized laser pulses. These fluctuations are caused primarily by an intrinsic flash-lamp instability. The relative variation in the flash-lamp output $\delta E_{\text{pump}}/E_{\text{pump}}$ leads to a variation of the amplified pulse energy $\delta E_{\text{out}}/E_{\text{out}}$ as[7]

$$\delta E_{\text{out}}/E_{\text{out}} \approx \ln\left(G_{\text{tot}}\right)\delta E_{\text{pump}}/E_{\text{pump}}, \qquad (1)$$

where G_{tot} is the total small-signal gain. For a standard regen, $G_{\text{tot}} \approx 10^7$ to 10^9; therefore, for $\delta E_{\text{out}}/E_{\text{out}} \approx 2\%$, the pump energy variation must be $\delta E_{\text{pump}}/E_{\text{pump}} \le 0.1\%$. For a standard flash-lamp–pumped regen, this is difficult, if not impossible, to achieve.[6,7] In addition, fluctuations in the pulse energy injected into the regen can also affect the regen output stability. For an externally synchronizable pulse, 2% regen output stability requires approximately the same stability for the injected pulse. This is difficult to achieve since the efficiency of injecting an optical pulse into the regen is affected by many factors that are difficult to control. A negative feedback can enhance the stability and external synchronizability of the regen,[8] but the time-dependent losses introduced by that negative feedback can cause undesirable temporal-pulse-shape distortions of the injected pulse during amplification. These distortions are difficult to model accurately, which seriously hampers the generation of a desired pulse shape at the regen output.

We developed a flash-lamp–pumped Nd:YLF regen with a redesigned negative-feedback system that completely satisfies OMEGA requirements. This feedback system introduces no temporal-pulse distortions, apart from pulse distortion due to gain saturation, that can be accurately modeled and compensated for. In the following sections we will discuss practical aspects of this regen design and present results of our numerical modeling and experimental measurements.

Negative-Feedback System for the Regenerative Amplification of Temporally Shaped Pulses

A negative feedback renders the regen output insensitive to input variations as well as to gain and loss fluctuations inside the regen cavity. The feedback signal is derived from the intracavity pulse energy and controls the intracavity losses. A block diagram of this regen is shown in Fig. 76.11. The instantaneous intracavity pulse energy is sensed by a photodiode whose signal is amplified by feedback electronics and applied to the Pockels cell electrode; thus, the losses increase as the circulating pulse energy increases, resulting in a steady-state round-trip gain near unity. After the feedback (pre-lase) phase, all cavity losses are eliminated, and the pulse is amplified as in a standard *Q*-switched oscillator.

The pre-lase phase is crucial for stabilizing the output pulse energy. Pulses injected into the regen above the average energy reach the steady-state phase early in time, while injected pulses with less energy reach the steady-state phase later. In the steady-state phase, the circulating intracavity pulse energy is constant and independent of the injected pulse energy (Fig. 76.12); thus, the regen with negative feedback is very insensitive to input fluctuations, in contrast to a regen without feedback.

The steady-state phase also compensates for gain fluctuations caused by flash-lamp fluctuations. During the steady-state phase the circulating-pulse energy remains approximately constant while the gain continuously decreases due to the energy dissipated by the feedback losses. The rate at which gain is reduced after each round-trip depends on the ratio of the intracavity pulse fluence to the saturation fluence. The exact value of the intracavity pulse energy in the pre-lase phase can be controlled externally to minimize the regen output fluctuations due to gain or loss variations (Fig. 76.12).

Successful implementation of this distortionless negative-feedback system places stringent requirements on the feedback electronics. Our intracavity Pockels cells are KD*P crystals that require the feedback electronics to deliver high-voltage electrical signals in the 2- to 3-kV range in order to introduce noticeable intracavity losses. Past experience has

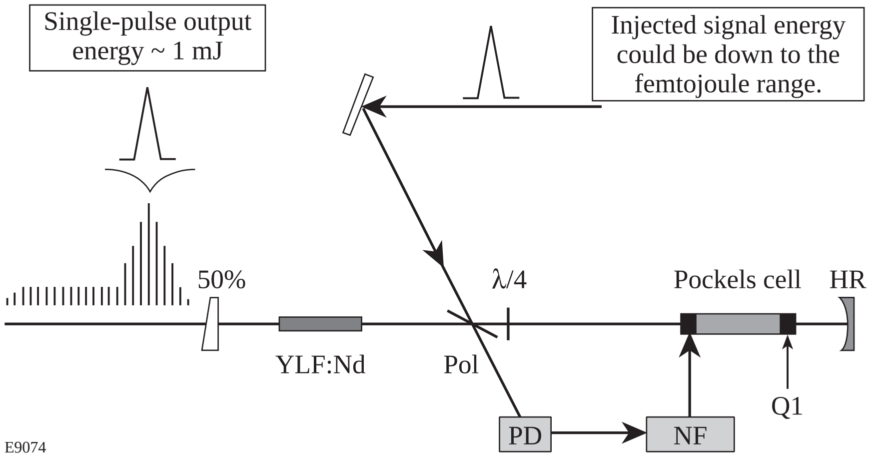

Figure 76.11
Block diagram of the regen with negative feedback.

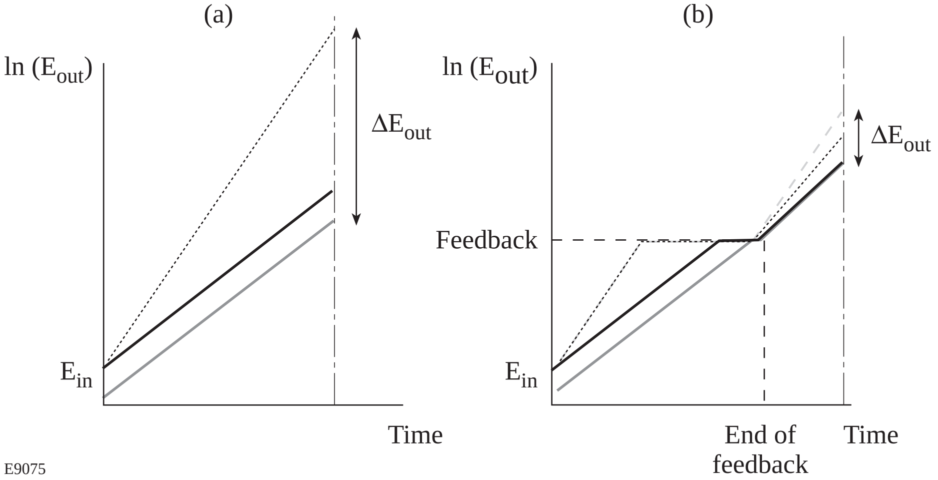

Figure 76.12
Semilog schematic plot of the energy evolution in the regen (a) without feedback and (b) with negative feedback. Negative feedback mitigates effects of shot-to-shot gain and loss fluctuations and injected-pulse energy variation. The solid curve represents the average injected energy and the average regen gain. The dotted curves represent the average injected energy and a regen gain higher than the average gain. The shaded curve represents a case where the injected energy is less than average and the regen gain is average.

shown[9] that the negative-feedback electronics must have a delay time shorter than 2 to 3 regen cavity round-trips. To stabilize the intracavity pulse energy, the feedback electronics must respond faster than the relaxation-oscillation frequency[10]

$$\omega_0 = \sqrt{(r-1)\gamma_c\gamma_{\mathrm{YLF}}}\,, \tag{2}$$

where γ_c is the inverse photon lifetime in the regen cavity, γ_{YLF} is the inverse relaxation time of the upper laser level of Nd:YLF, and r is the pumping rate. These feedback requirements are difficult, if not impossible, to fulfill with standard electronics.

Typical fast, high-voltage feedback electronics strongly distort the output pulse shape because of small feedback-induced intracavity loss variations during the time the circulating pulse propagates through the Pockels cell. Although the single-pass distortions are small, their effect is cumulative, and after many round-trips the distortions become severe. To eliminate these distortions the negative-feedback signal applied to the Pockels cell must be constant while the shaped pulse propagates through the Pockels cell. This requires that the negative-feedback signal have no fast-frequency components, which contradicts Eq. (2).

This problem can be circumvented with a two-component, negative-feedback signal. The first component is a high dc voltage that introduces a time-independent constant loss and brings the regen very close to the steady-state phase. In this phase the relaxation-oscillation frequency of the regen is very small [see Eq. (2) with $r \approx 1$]; thus, the circulating pulse energy can be held constant with a second low-voltage, low-frequency electrical-feedback signal. Due to the low voltage and slow temporal variation of the second feedback component, the temporal shape of the amplified pulse is not distorted.

Regen Modeling

The regen dynamics were modeled in a manner similar to that published in Ref. 11. Using an ideal four-level amplifying medium, neglecting fluorescence depumping, and assuming that the pulse fluence J is much smaller than the saturation fluence J_s of the gain medium ($J_{s,\mathrm{Nd:YLF}} \approx 0.8$ J/cm^2 at 1053 nm), one obtains a pair of simplified recurrent rate equations:[4]

$$J_{k+1} = T_k \exp\left(g_k\right) J_k\,, \tag{3}$$

$$g_{k+1} = g_k - \left[\exp\left(g_k\right) - 1\right] J_k / J_s\,. \tag{4}$$

Here k is the index for the resonator round-trip; T_k, g_k, and J_k are the resonator transmission, gain coefficient, and pulse fluence during the k^{th} round-trip, respectively; and $g_k = \ln\left(G^{\mathrm{ss}}{}_k\right)$, where $G^{\mathrm{ss}}{}_k$ is the small-signal gain of the k^{th} round-trip. We have also assumed that the $G^{ss}\,J_k/J_s << 1$. The gain coefficient at the time of injection, g_0, is proportional to the pump energy E_{pump}. The calculated intracavity fluence of the regen is shown in Fig. 76.13(a) for an initial net round-trip gain $G_0 = 2.1$, which is typical for OMEGA regens. The dependence of the output pulse train (pulse energy and build-

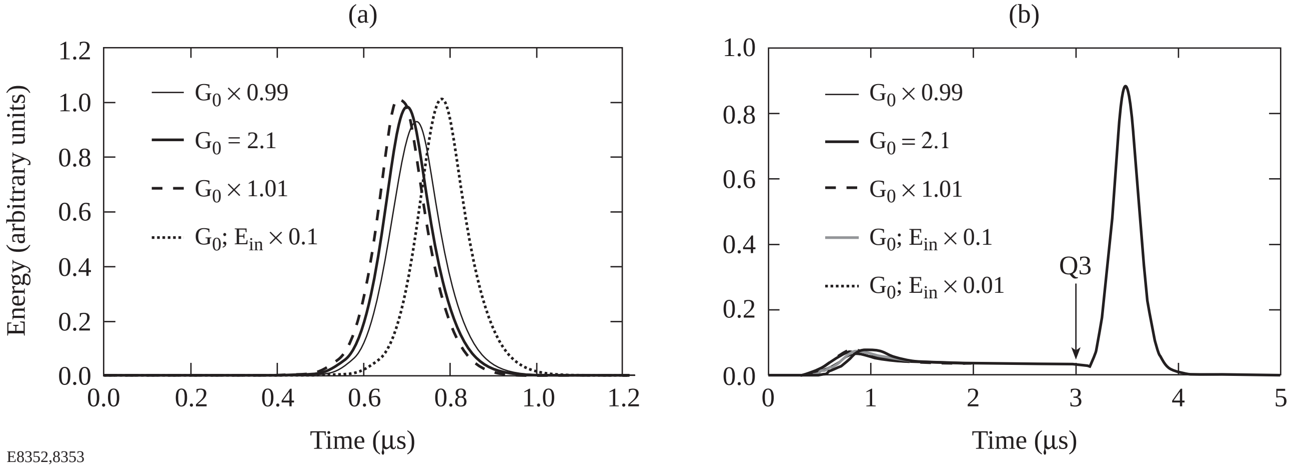

Figure 76.13
Numerical simulations clearly demonstrate the stabilizing effect of the negative feedback on the output energy of the regen: (a) thick solid line—standard regen output; dashed/thin solid lines—pumping energy varied by ±1%; dotted line—10× less injected pulse fluence; (b) same as (a) but with negative feedback.

up time) on variations in net round-trip gain G_0 and injected pulse energy E_{in} are also shown in this figure.

The two-component negative feedback is modeled by multiplying the right side of Eq. (3) by the transmission functions T_{dc} and T_{ac}. The former models the time-independent loss while the latter accounts for the modulated feedback losses required to maintain constant circulating pulse energy. The actual value of T_{dc} is adjusted in such a way that the regen operates just slightly above threshold. In the steady-state phase, T_{ac} is inversely proportional to the difference between the intracavity pulse fluence and the threshold fluence J_{th} of the pulse at the time when the dc feedback losses were introduced. In Fig. 76.13(b), modeling results for the regen with the feedback are presented for the same initial conditions as in Fig. 76.13(a). The negative-feedback stabilization of the regen output is clearly apparent by the insignificant variations in maximum amplitude of the train envelope as well as by the constant build-up time beyond the externally triggered *Q*-switch [Q3 in Fig. 76.13(b)].

Experimental Results

The block diagram for the regen with negative feedback is shown in Fig. 76.14. A temporally shaped optical pulse is injected into the regen through a polarization-maintaining, single-mode fiber and a Faraday isolator. At the time of injection, a step-like quarter-wave voltage (~4.1 kV) is applied to the Pockels cell, and the injected pulse experiences small losses and relatively high round-trip gain. When the energy of the amplified pulse reaches a predetermined level (~10 μJ), a second step of ~2 kV applied to the second Pockels cell electrode changes the differential voltage applied across the Pockels cell, adding a time-independent constant intracavity loss. As a result, the net round-trip gain is reduced to just slightly above threshold, preventing further rapid buildup of the laser pulse. At this time, a small feedback voltage applied to the Pockels cell is sufficient to control and maintain a constant steady-state pulse energy over periods of a few microseconds. Furthermore, since the regen operates close to the threshold, the response time of the regen (equal to the inverse of the relaxation-oscillation frequency) is very long compared to the regen round-trip time of 26 ns. This completely eliminates pulse distortions caused by the negative feedback. At a predetermined time [Q3 in Fig. 76.13(b)], a third *Q*-switch voltage step is applied to the Pockels cell, which compensates the losses caused by the previous loss-producing voltages. This process produces a train of highly stable pulses under a *Q*-switched envelope as shown in Fig. 76.15. Single shaped pulses of ~1 mJ and exceptional energy stability (~0.2% rms) have been generated over periods exceeding 4 h of continuous 5-Hz operation [$\sim 7.7 \times 10^4$ shots (see Fig. 76.16)]. A 0.5% rms energy stability was observed over a 9-h period ($>1.6 \times 10^5$ shots). In addition to its excellent energy stability, the regen output is also very insensitive to the injected energy (see Fig. 76.17).

Injection of a square pulse confirms that the only measurable distortions of the temporal pulse shape are due to gain saturation. These distortions can be modeled precisely by simple rate equations[11] and can be effectively precompensated (see Fig. 76.18). With the present system we have experimentally demonstrated the generation of kilojoule-level laser pulses from the OMEGA laser system with prescribed temporal pulse shapes (see Fig. 76.19).

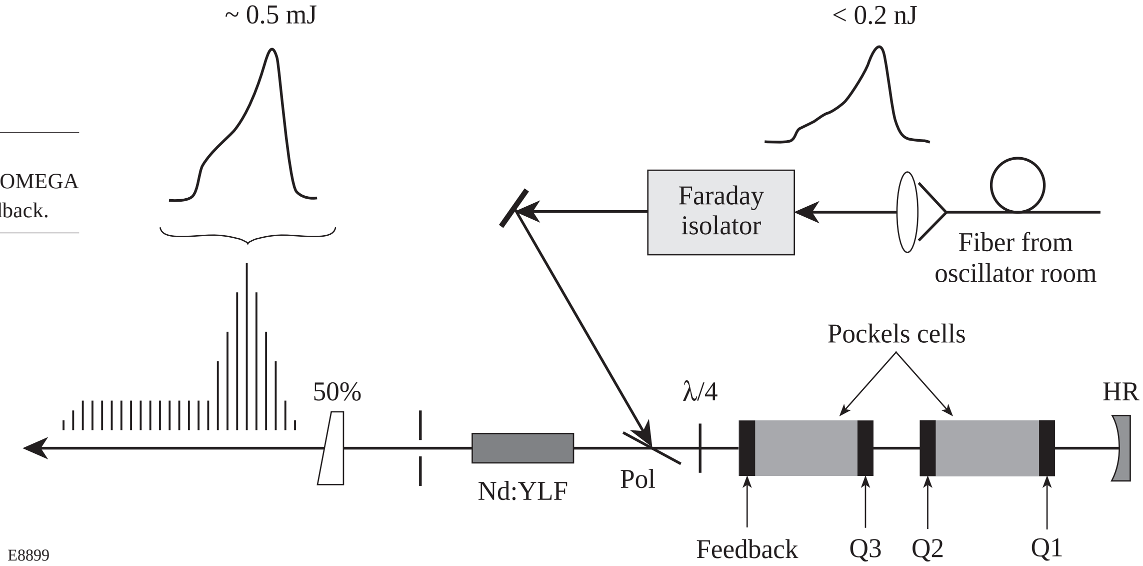

Figure 76.14
Block diagram of the OMEGA regen with negative feedback.

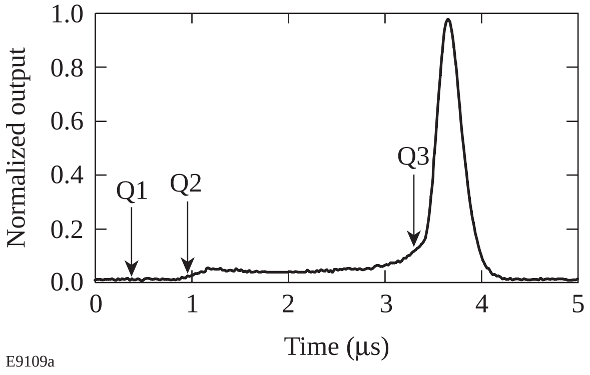

Figure 76.15
Measured envelope of the output pulse train from the regen with negative feedback.

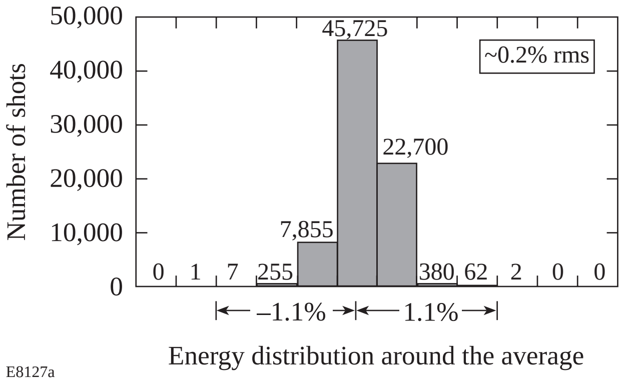

Figure 76.16
Stability histogram for the single-pulse energy distribution at the regen output. Data were collected over 4 h of continuous operation at a 5-Hz repetition rate.

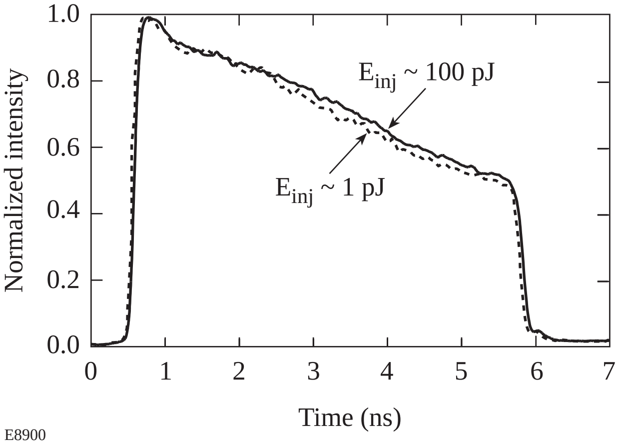

Figure 76.17
IR streak camera measurements of the regen output. Solid line—the injected pulse at nominal energy; dashed line—the injected pulse energy attenuated by a factor of 100.

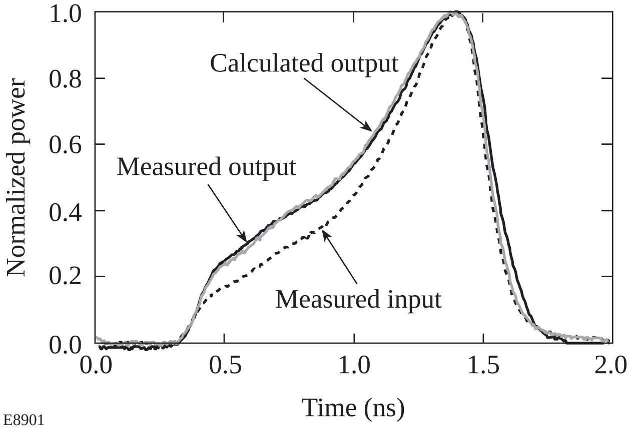

Figure 76.18
Measured and simulated regen output pulse shapes.

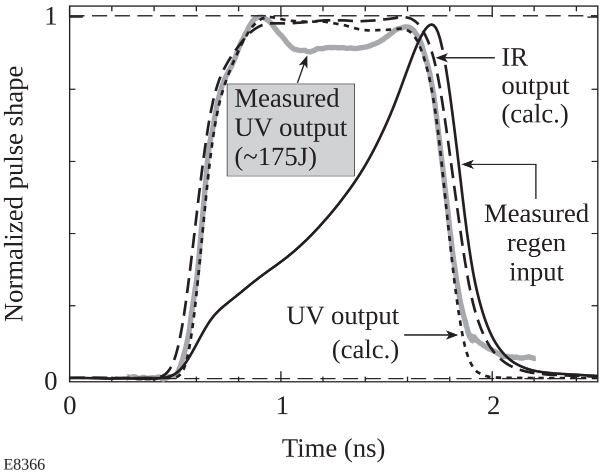

Figure 76.19
Measured and simulated UV output pulse shapes for a 10-kJ UV OMEGA laser shot. The simulated UV pulse shape uses the measured regen input pulse shape. The calculated IR pulse shape at the input to the frequency triplers is also shown.

Conclusion

In conclusion, we have developed a negative-feedback–controlled and externally synchronizable Nd:YLF regenerative amplifier capable of amplifying shaped optical pulses to the millijoule level. Long-term, shot-to-shot energy fluctuations of ~0.2% rms represent, to our knowledge, the best energy stability ever demonstrated for a millijoule-level laser system, either flash lamp pumped or diode pumped. In addition to superior stability and reproducibility, the current OMEGA regen output is very insensitive to the injected energy, and the temporal distortions due to the negative feedback are immeasurable. Four regens equipped with this negative-feedback system have operated flawlessly on OMEGA for over two years.

ACKNOWLEDGMENT

This work was supported by the U.S. Department of Energy Office of Inertial Confinement Fusion under Cooperative Agreement No. DE-FC03-92SF19460, the University of Rochester, and the New York State Energy Research and Development Authority. The support of DOE does not constitute an endorsement by DOE of the views expressed in this article.

REFERENCES

1. R. L. Keck, A. Okishev, M. D. Skeldon, A. Babushkin, and W. Seka, in *Laser Interaction and Related Plasma Phenomena*, edited by G. H. Miley and E. M. Campbell (American Institute of Physics, New York, 1997), Vol. 406, pp. 333–340.

2. R. B. Wilcox *et al.*, in *Laser Coherence Control: Technology and Applications*, edited by H. T. Powell and T. J. Kessler (SPIE, Bellingham, WA, 1993), Vol. 1870, pp. 53–63.

3. T. R. Boehly, D. L. Brown, R. S. Craxton, R. L. Keck, J. P. Knauer, J. H. Kelly, T. J. Kessler, S. A. Kumpan, S. J. Loucks, S. A. Letzring, F. J. Marshall, R. L. McCrory, S. F. B. Morse, W. Seka, J. M. Soures, and C. P. Verdon, Opt. Commun. **133**, 495 (1997).

4. W. H. Lowdermilk and J. E. Murray, J. Appl. Phys. **51**, 2436 (1980).

5. J. E. Murray and W. H. Lowdermilk, J. Appl. Phys. **51**, 3548 (1980).

6. S. C. Burkhart *et al.*, in *First Annual International Conference on Solid State Lasers for Application to Inertial Confinement Fusion*, edited by M. André and H. T. Powell (SPIE, Bellingham, WA, 1995), Vol. 2633, pp. 48–58.

7. B. M. Van Wonterghem, J. T. Salmon, and R. W. Wilcox, *ICF Annual Report 1995*, Lawrence Livermore National Laboratory, Livermore, CA, UCRL-LR-105821-95-1, 42 (1996).

8. D. L. Brown, I. Will, R. G. Roides, C. K. Merle, M. D. Skeldon, and W. Seka, in *1993 Optical Society of America Annual Meeting*, 1993 OSA Technical Digest Series, Vol. 16 (Optical Society of America, Washington, DC, 1993), p. 250.

9. I. M. Bayanov *et al.*, Sov. J. Quantum Electron. **19**, 994 (1989).

10. A. E. Siegman, *Lasers* (University Science Books, Mill Valley, CA, 1986).

11. M. D. Skeldon, A. Babushkin, W. Bittle, A. V. Okishev, and W. Seka, IEEE J. Quantum Electron. **34**, 286 (1998).

Transient Bandwidth Analysis of Photoconductive Microwave Switches Implemented in the OMEGA Pulse-Shaping System

The OMEGA laser fusion program at LLE calls for complex, temporally shaped optical pulses incident on fusion targets.[1] The pulse-duration and rise-time specifications of these optical pulses dictate an electrical pulse–shaping system bandwidth of approximately 0.1 to 10 GHz. The optical pulses are created by imprinting an electrical equivalent of the desired optical envelope onto an optical square pulse, using an integrated-optics Mach–Zehnder interferometric electro-optic modulator as shown in Fig. 76.20. The electrical pulse shape is generated by the reflection of an electrical square pulse from a distributed variable-impedance microstrip transmission line. The electrical square pulse is generated by illuminating a photoconductive semiconducting (PCS) switch in a series–gap configuration, which discharges a microstrip transmission line charged with a dc voltage. Assuming the PCS switch is saturated by the illumination, the rise time of the electrical pulse corresponds to the rise time of the optical illumination trigger pulse, and the switch conductivity remains roughly constant for the duration of the electrical pulse. The fall time is computed by convolving the rise time with the reflection impulse response of the second, unilluminated switch.[2] The resulting propagating square pulse has an amplitude of half the dc voltage and a duration of twice the charge-line's round-trip time.[3]

Measurements of the shaped electrical signal before and after the PCS switches, as shown in Fig. 76.21, indicate that the frequency response of the shaped laser pulse is strongly limited by the transmission of the shaped electrical pulse through the PCS switches. Time-gated microwave measurements of the switch attenuation did not reveal the source of the switch's bandwidth limitations.[4] In this latter case, however, the optical illumination conditions were significantly different from the actual OMEGA operating conditions, and the measurements were performed using a simple time-windowed,

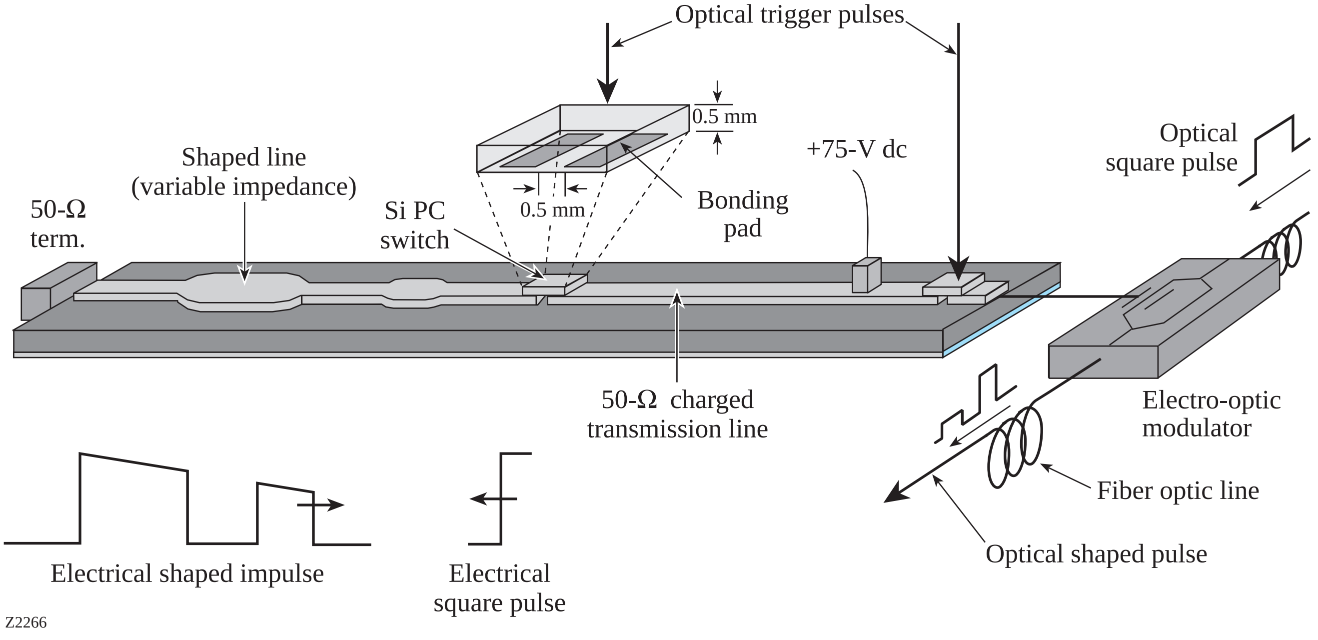

Figure 76.20
The microwave signal reflected from the shaped variable impedance line must pass through two PCS switches before reaching the electro-optic modulator.

power-detection technique. Also, phase/dispersion variations and decay of the PCS switch transmission within the measurement time window could not be detected with this technique. These limitations motivated the design and implementation of the improved measurement scheme described in this article.

(a)

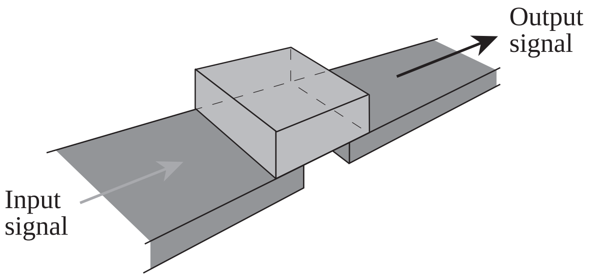

(b) Input and output signal and spectra (inset)

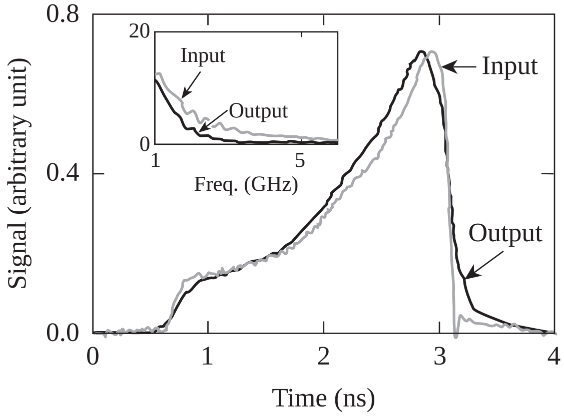

(c) PCS switch frequency response

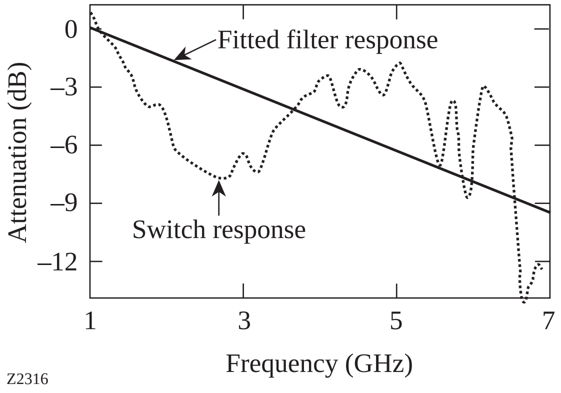

Figure 76.21
The PCS switch, microstrip line, and input and output signals are shown graphically in (a). These signals were (b) measured and their spectra found (inset). The (c) switch response was computed by a ratio of the spectra and compared to a single-pole low-pass filter.

PCS switches, unlike conventional diode or transistor microwave switches, do not operate in a steady-state “on/closed” condition. After optical illumination, the carrier recombination dynamics cause the switch transmission to decay to an “off/open” state. For example, the PCS switches used on OMEGA are typically driven to their highest (saturated) charge-carrier density by a 500-ps, 100-μJ optical pulse. After illumination, the carrier density decays monotonically, meaning that the PCS switch’s on-state is transient in nature since it depends on the carrier recombination dynamics. This imposes requirements beyond the capabilities of conventional microwave test equipment (e.g., network analyzers, modulation analyzers): PCS switches as implemented in the OMEGA pulse-shaping system cannot be modeled as exclusively filters or modulators. The modulator model breaks down because PCS switches transmit signals with a bandwidth comparable to the transmission bandwidth of the switch, and they don’t fit the filter model well because of their time-varying properties. Note that due to thermal damage issues at the metal–semiconductor (soldered-contact) interface, cw optical illumination for the purpose of creating a time-invariant device in the saturated regime is not possible.[5] This means that it is necessary to use transmission equations for a linear device that are more general than those for filters and modulators and to develop a measurement system capable of measuring a generalized transmission function.

We describe a method for measuring the transient complex (amplitude and phase) frequency response of a microwave device, and we give results for PCS switch measurements. These measurements were performed with PCS switch excitation conditions identical to those used on OMEGA, and over temporal durations and frequency ranges of interest to OMEGA pulse-shaping experiments. With this system, microwave devices whose transient bandwidths were previously only approximated can now be characterized and compared with a more general, multiport microwave device theory. This measurement scheme is compatible with triggerable microwave devices that have a deterministic time evolution; other examples aside from photoconductive devices are amplifier and active filter turn-on/turn-off transients and atmospheric multipath fading due to relative antenna motion.

Theoretical Background

From a linear-system viewpoint, the relationship between the input and output voltage signals of the device under test (DUT) shown in Fig. 76.22(a) is

$$V_n(\omega) = S(\omega) \cdot V_m(\omega), \tag{1}$$

where $V_m(\omega)$ and $V_n(\omega)$ are the total voltages across ports m and n and $S(\omega)$ is the DUT (filter) frequency response. Equation (1) can be Fourier transformed to

$$v_n(t) = \int_{\tau=-\infty}^{\tau=\infty} h(t-\tau) \cdot v_m(\tau)\, d\tau \,, \tag{2}$$

where $v_m(t)$ and $v_n(t)$ are the total instantaneous voltage signals and $h(t)$ is the impulse response.

Measurements of microwave devices conventionally involve either scalar or vector network analysis of scattering or S parameters, where $a_n(\omega)$ and $b_n(\omega)$ are the incident and scattered signals from a port n, which has a characteristic impedance Z_0, also shown in Fig. 76.22.[6] These microwave signals a and b are related to the total voltage across the port by the incident and reflected voltages V^+ and V^-:

$$a = \frac{V^+}{\sqrt{Z_0}}, \quad b = \frac{V^-}{\sqrt{Z_0}} \tag{3}$$

and are related to each other (for a two-port DUT) by the relationship

$$\begin{bmatrix} b_1 \\ b_2 \end{bmatrix} = \begin{bmatrix} S_{11} & S_{12} \\ S_{21} & S_{22} \end{bmatrix} \begin{bmatrix} a_1 \\ a_2 \end{bmatrix}. \tag{4}$$

Since the PCS switches operate in the transmission mode, we will focus on the S_{21} parameter. The S_{21} parameter relates the signal transmitted from port 2 (output) to the signal incident on port 1 (input) in the frequency domain; this relation is similar to Eq. (1) and is given by

$$b_2(\omega) = S_{21}(\omega) \cdot a_1(\omega). \tag{5}$$

The transmission parameter S_{21} is defined in the spectral domain because of the assumed linear time invariance of the DUT. The assumption of a linear time-invariant (LTI) device is only appropriate, however, when the DUT response approaches an ideal filter (i.e., does not vary in time).

A linear device such as an ideal amplitude or phase modulator is not time invariant. Modulators are typically measured with spectrum or modulation analyzers in the linear small-signal regime with narrow-band (cw) input signals, so that the assumption of an infinite-bandwidth ideal modulator introduces negligible error. The equations characterizing a modulator's input–output relationship is then exactly complementary to Eqs. (1) and (2):

$$v_n(t) = k(t) \cdot v_m(t) \tag{6}$$

$$V_n(\omega) = \int_{\xi=-\infty}^{\xi=\infty} K(\omega-\xi) \cdot V_m(\xi)\, d\xi \,, \tag{7}$$

where $k(t)$ and $K(\omega)$ are the modulation function and its transform.[7]

If a linear device cannot be approximated as either time invariant or as having infinite bandwidth, then none of the above equations is appropriate. Test systems that are based on these equations (such as spectrum, modulation, and network analyzers) are unable to measure the transfer function of such a device; therefore, a more general input–output relationship has been developed. This was done by recognizing that any linear device can be characterized by the generalized form of the filter and modulator Eqs. (2) and (7):

$$v_n(t) = \int_{\omega=-\infty}^{\omega=\infty} G(t,\omega) \cdot V_m(\omega)\, d\omega \,, \tag{8}$$

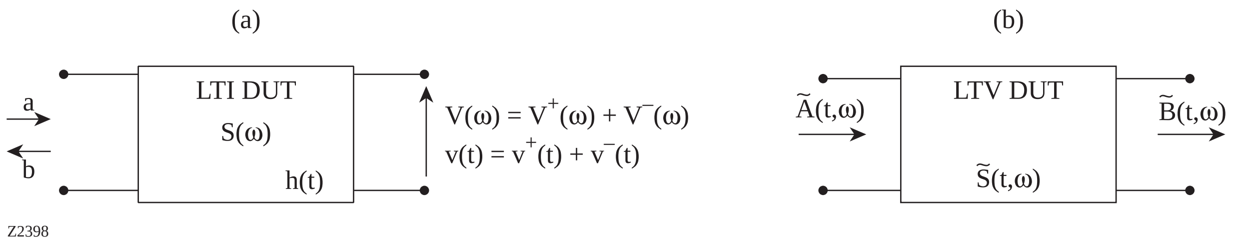

Figure 76.22
(a) Conventional LTI (filter) two-port microwave devices use a scattering matrix to define input–output relationships between the signals, while (b) LTV microwave devices relate input to output via a more general $\tilde{S}(t,\omega)$ matrix.

where $G(t,\omega)$ is the (more general) input–output relation, now a function of both time and frequency.[8] This function $G(t,\omega)$ has a simple extension to conventional microwave measurements if it is viewed as a generalized $S(\omega)$ parameter and renamed $\tilde{S}(t,\omega)$, as shown in Fig. 76.22(b). The input–output transmission function is similar to Eq. (5):

$$\tilde{B}_2(t;\omega) = \tilde{S}_{21}(t,\omega) \cdot \tilde{A}_1(t;\omega), \qquad (9)$$

where $\tilde{A}$ and $\tilde{B}$ are joint time-frequency distributions of one-dimensional functions (indicated by the semicolon between the variables) related to v^+ and v^- by the Wigner time-frequency (WTF) distribution[9]

$$\tilde{A}(t;\omega) = \frac{1}{Z_0} \int_{-\infty}^{\infty} v^+(t+\tau/2)\, v^{+*}(t-\tau/2)\, e^{-j\omega\tau} d\tau, \qquad (10)$$

and $\tilde{B}$ is defined similarly for v^-.

This input–output relationship of Eq. (9) is simpler than the integral function of Eq. (8) and has the further advantage that in the microwave regime the signals a and b are more easily measured than the total transmission-line voltages $V_m(\omega)$ and $v_n(t)$. Any $\tilde{S}$ parameter can be determined from Eq. (9) and from measurements of the input and output microwave signals at the appropriate ports. For example, in a two-port microwave device such as a PCS switch, if the microwave signal is incident on port 1 and the response measured at port 2, the $\tilde{S}_{21}$ parameter can be determined by dividing the WTF distribution of the output (port 2) signal by the WTF distribution of the input (port 1) signal. Comparing Eqs. (9), (1), and (5), the parameter $\tilde{S}_{21}(t,\omega)$ can be seen as a time-varying frequency response $S(\omega)$.

Note that $\tilde{S}$ is the (complex) time-varying frequency response of the microwave device and is to be distinguished from the time-varying spectrum of a signal $\tilde{A}$, a joint time-frequency distribution generated from a one-dimensional (complex) signal by Eq. (10). To make this difference between $\tilde{A}$ and $\tilde{S}$ apparent, one can Fourier transform $\tilde{S}$ in the second variable (ω to τ), which results in $\tilde{S}(t,\tau)$. A magnitude surface plot of this two-dimensional function shows the temporal change of the impulse response "$h(\tau)$" with time t. In contrast, transforming $\tilde{A}$ in either variable will result in a surface plot of a one-dimensional function multiplied by itself along each axis, i.e., if $\tilde{A}(t;\omega)$ was Fourier transformed in the second variable (ω to τ), the resulting function $\tilde{A}(t;\tau)$ would by definition be proportional to $v^+(t) \cdot v^+(\tau)$. This is simply $v^+(t)$ multiplied by itself in the second, dummy variable τ and therefore not a function of two independent variables, as $\tilde{S}(t,\tau)$ is. Thus, the time-varying bandwidth $\tilde{S}$ of a device is distinct from the time-varying spectrum of a signal $\tilde{A}$.[10,11]

Experimental Design

The system we created to measure the time and frequency variations of the switch's transfer function is based on a microwave interferometric measurement and is shown in block-diagram form in Fig. 76.23. The DUT for which we measure the two-dimensional transfer function $\tilde{S}(t,\omega)$ is shown at the center of the figure (in our case, a PCS switch). The DUT is triggered (in our case, by a laser pulse), causing a single-frequency microwave signal of known power and phase from the microwave generator to propagate through the DUT and also through a separate, parallel reference arm consisting of an amplifier and a phase shifter. The two arms, after splitting at the directional coupler, are recombined and compared to one another in amplitude (at the diode detectors) and phase (at the mixer/phase detector). Alternatively, the signal from each arm can be measured directly by an oscilloscope of sufficiently high bandwidth and subsequently compared. Both measurements are shown in Fig. 76.23. The timing system synchronizes the triggering of the DUT with the phase of the microwave signal incident on it, so that each trigger occurs at the same phase of the microwave signal. This allows sampling oscilloscope measurements, which improves the measurement resolution over single-shot digitizing oscilloscopes.

The signal-measurement process proceeds in the following step-and-dwell manner: The microwave generator is set to a single given frequency of known phase and amplitude. The DUT is then triggered, and the evolution of the transmitted signal is measured and compared with the reference arm signal for the temporal duration of interest. The microwave generator then steps to the next microwave frequency, and the process repeats for the range of frequencies of interest. The recorded data is then reduced to two sets of complex (amplitude and phase), two-dimensional arrays of incident and transmitted signals corresponding to $\tilde{A}$ and $\tilde{B}$. Using Eq. (9) we calculate the transfer function $\tilde{S}(t,\omega)$, which can then be analyzed for bandwidth and modulation features. For a PCS switch, the transfer function is expected to show an exponentially decaying modulation due to carrier recombination and a (possibly changing) bandwidth, which can be modeled by a lumped-element circuit consisting, in general, of a time-changing reactance and a time-changing resistance. The values of these elements can then be associated with switch properties such as carrier lifetime, non-ohmic contacts, thickness and gap length,

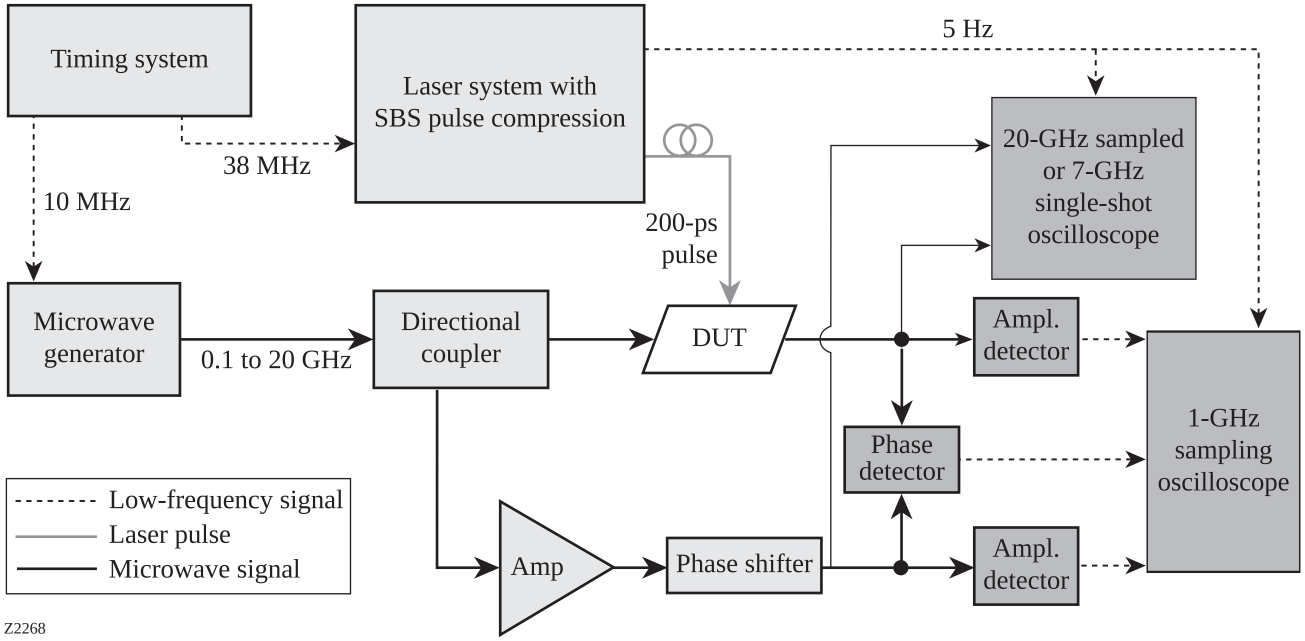

Figure 76.23
Signal flow of system capable of analyzing transient-bandwidth devices.

and the bandwidth of the switch can be optimized by appropriately modifying these switch properties. For example, the metal–semiconductor interface can be made Schottky or ohmic-like by selective ion implantation and dopant diffusion, which affects carrier recombination, surface velocity, trapping states, and contact resistance. Switch thickness and switch-gap width and length will affect capacitive coupling and series resistance and should be selected so as to minimize the switch RC time constant and maximize photon absorption.

Experimental Results

A representative magnitude plot of the two-dimensional transfer function $\tilde{S}(t,\omega)$ of a PCS switch is shown in Fig. 76.24. As explained in the **Theoretical Background** section, $\tilde{S}(t,\omega)$ is necessary to describe the transmission response of a PCS switch [$S(\omega)$ is inadequate] because the switch modulates a signal whose spectral content is comparable to its bandwidth. Features of the transfer function, such as the conductive carrier decay along the temporal axis and frequency-dependent attenuation along the spectral axis due to bandwidth limitations, are readily observed. By numerically fitting a linear lumped-element model having both filtering and modulating components to the measured transfer function, values of various microwave components can be extracted. The fitted model, shown in Fig. 76.25, is a simple low-pass filter in series with an exponentially decaying resistive element. The switch's 3-dB bandwidth is approximately 5 GHz, which agrees well with the observed bandwidth loss of shaped pulses propagating through the OMEGA pulse-shaping system (Fig. 76.26).

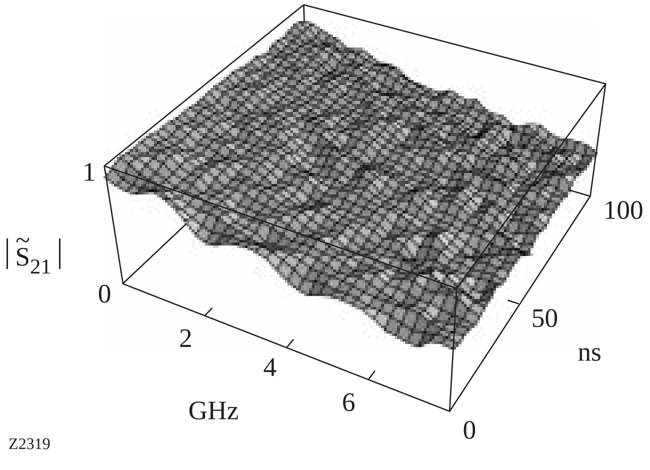

Figure 76.24
Measured $\tilde{S}_{21}(t,\omega)$ shows carrier decay along the temporal axis and bandwidth limitations along the spectral axis.

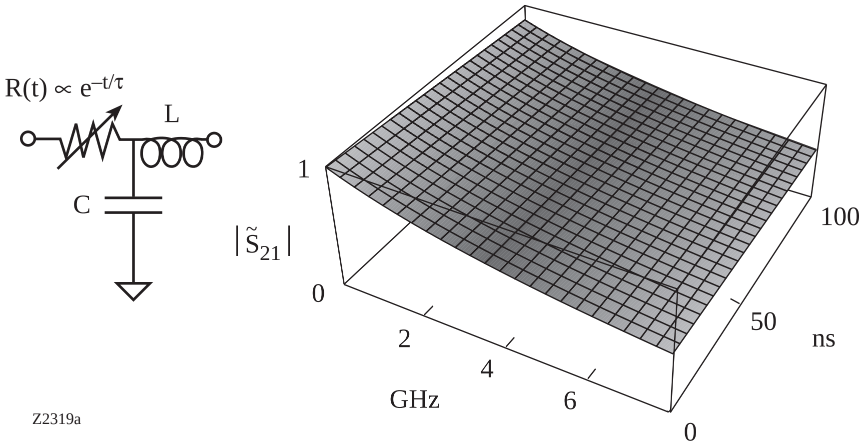

Figure 76.25
Modeled $\tilde{S}_{21}(t,\omega)$ accurately fits an exponentially decaying resistance in series with a low-pass filter to the measured data.

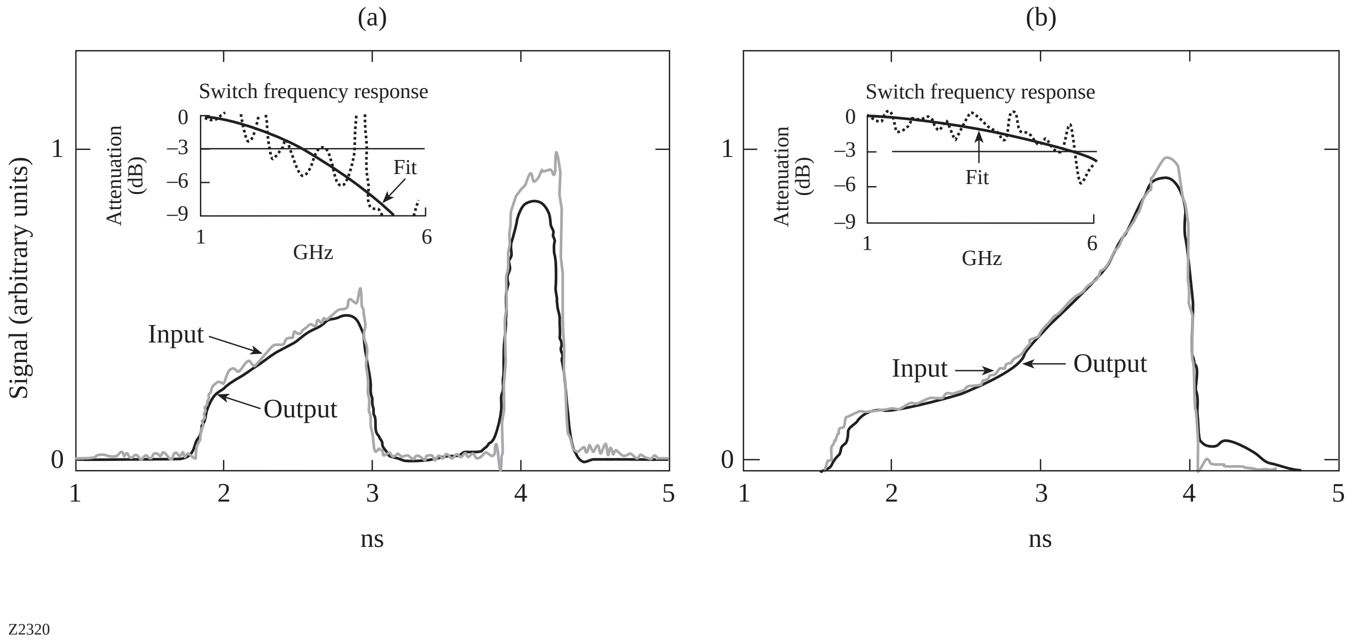

Figure 76.26
By optimizing switch parameters, transmission bandwidth on OMEGA pulse shaping has been improved from (a) mid-1995, the beginning of OMEGA's pulse shaping, to (b) early 1998.

Conclusions

Measurements of optical and electrical temporal pulse shapes at different locations in our pulse-shaping system indicate that the primary bandwidth limitations occur during transmission of our electrical pulse shapes through the PCS switches. When pulse shaping was first implemented on OMEGA, the measured attenuation at 10 GHz (corresponding to 30-ps pulse rise- and fall-times) was more than 12 dB through the switch, and the 3-dB bandwidth was near 3 GHz. This frequency response is significantly worse than the other components in the pulse-shaping system: e.g., microstrip transmission line, connectors, and electro-optic modulator. Modeling of photoconductive switches[12] indicates that a much larger bandwidth is theoretically possible; thus, efforts were taken to isolate and comprehensively measure the microwave transmission bandwidth of our PCS switches. This characterization made possible the systematic optimization of the many parameters of the switch, such as gap length, microwave skin depth versus optical absorption depth, and metal–semiconductor contact preparation. Since conventional network analyzers were incapable of determining the bandwidth of a device that varied in time, a measurement system was designed and built tailored to such time-varying devices. This measurement system allowed determination of the relationship between the properties of the switch and its frequency response characteristics. By improving the physical switch properties, the 3-dB bandwidth of the OMEGA pulse-shaping PCS switches has been increased to over 5 GHz. The full bandwidth of the implemented PCS switches is now as broad as the next-most-limiting device in the pulse-shaping system (believed to be the electro-optic modulator) and is sufficient for current OMEGA optical-pulse-shape requirements.

ACKNOWLEDGMENT

This work was supported by the U.S. Department of Energy Office of Inertial Confinement Fusion under Cooperative Agreement No. DE-FC03-92SF19460 and the University of Rochester. The support of DOE does not constitute an endorsement by DOE of the views expressed in this article. The author also acknowledges the support of the Frank Horton Graduate Fellowship Program.

REFERENCES

1. M. D. Skeldon, A. Okishev, S. A. Letzring, W. R. Donaldson, K. Green, W. Seka, and L. Fuller, in *Optically Activated Switching IV*, edited by W. R. Donaldson (SPIE, Bellingham, WA, 1994), Vol. 2343, pp. 94–98.
2. G. H. Owyang, *Foundations for Microwave Circuits* (Springer-Verlag, New York, 1989).
3. S. C. Burkhart and R. B. Wilcox, IEEE Trans. Microwave Theory Tech. **38**, 1514 (1990).
4. K. Green, W. R. Donaldson, R. Sobolewski, A. Okishev, M. D. Skeldon, S. A. Letzring, and W. Seka, in *First Annual International Conference on Solid State Lasers for Application to Inertial Confinement Fusion*, edited by M. André and H. T. Powell (SPIE, Bellingham, WA, 1995), Vol. 2633, pp. 615–621.
5. W. C. Nunnally, in *High-Power Optically Activated Solid-State Switches*, edited by A. Rosen and F. Zutavern (Artech House, Boston, 1994), pp. 29–42.
6. K. Kurokawa, IEEE Trans. Microw. Theory Tech. **MTT-13**, 194 (1965).
7. H. D'Angelo, *Linear Time-Varying Systems: Analysis and Synthesis*, The Allyn and Bacon Series in Electrical Engineering (Allyn and Bacon, Boston, 1970).
8. L. A. Zadeh, J. Appl. Phys. **21**, 642 (1950).
9. M. A. Poletti, J. Audio Eng. Soc. **36**, 457 (1988).
10. D. J. Kane and R. Trebino, Opt. Lett. **18**, 823 (1993).
11. F. T. S. Yu and G. Lu, Appl. Opt. **33**, 5262 (1994).
12. S. S. Gevorgian, IEE Proc. J, Optoelectron. **139**, 153 (1992).

Simulations of Near-Field Intensity Modulations in High-Intensity Laser Beams due to Self- and Cross-Phase Modulation Between Orthogonally Polarized Laser Beams Emerging from a Diamond-Turned KDP Wedge

The near-field intensity modulation due to a diamond-turned KDP wedge is investigated through computer simulations within the framework of its application to LLE's OMEGA laser system. KDP wedges will be installed on each OMEGA beamline and mounted 12 m away from the final focusing optics. The wedges will improve the direct-drive inertial confinement fusion uniformity by a process known as polarization smoothing. Diamond turning is the finishing process of choice due to the greater cost incurred by installing polished KDP crystals on every beamline.

The Nova laser facility at the Lawrence Livermore National Laboratory (LLNL) reported blast-shield damage that was linked to the mid-range spatial wavelengths (1 to 4 mm) of scratch marks on diamond-turned KDP crystals in use at the time. This motivated LLE to employ polished KDP crystals for frequency tripling on OMEGA during its 24- to 60-beam upgrade (completed in 1995) because polishing produces a smoother distribution of spatial wavelengths of lower amplitude. While diamond-turning technology has improved recently, residual concern has existed regarding the potential damaging effects of installing diamond-turned KDP crystals. This has prompted an investigation, both theoretical and experimental, into the potential effects of the scratch or milling marks left behind by diamond turning.

This article represents part of the theoretical investigation of this problem. In particular, the simulations model the nonlinear effects that result from (1) the beam propagation through the 12 m of air that separates the KDP wedge from the final focusing optics, (2) the initial phase perturbation of the beam due to the residual scratch marks on the diamond-turned KDP surface, and (3) the nonlinear index's polarization dependence. The danger here is that small-scale self-focusing might develop high-intensity spikes leading to filamentation damage in the final focusing optics. The simulations reported here demonstrate that KDP wedges, diamond-turned or smooth, are not a significant source of intensity modulation under OMEGA laser conditions. In addition, for a beam with a varying polarization state, these simulations exhibit an intensity enhancement in the vicinity of linear polarization due to the nonlinear effect of cross-phase modulation.

Diamond-Turned KDP Wedge

1. Polarization Smoothing

The concept of polarization smoothing originated from Kato[1] who recognized the uniformity that would result from rotating the polarization through 90° on half of the individual phase-plate elements chosen at random. A more practical device, first described in Ref. 2, is a wedge of birefringent material such as KDP. A linearly polarized beam incident upon the KDP wedge is split into two orthogonally polarized beams of equal intensity when the incident beam's polarization vector is oriented at 45° with respect to the slow and fast axes of the crystal (see Fig. 76.27). The resultant two orthogonal beams co-propagate at a slight angle of separation with respect to each other, determined by the wedge angle and the refractive indexes for the slow and fast waves. The current requirements for OMEGA set the wedge angle to 4.5 min. This causes a separation angle of 44 μrad between the two orthogonal beams and a relative offset of 80 μm after focusing on target. The relative offset of 80 μm achieves an instantaneous theoretical $1/\sqrt{2}$ reduction of the nonuniformity through spatial averaging, which complements the uniformity achieved by SSD alone.[3]

As a consequence of the separation angle, the combined polarization state of the two orthogonally polarized beams continuously cycles through all elliptical states along any transverse plane. The rate of change is determined by the transverse components of the wave vectors. Since the separation angle is small, the wavelength of the cycle is given by

$$\lambda_{\mathrm{pol}} = \frac{\lambda}{\sin(\theta)} = \frac{351\ \mathrm{nm}}{\sin\left(44\ \mu\mathrm{rad}\right)} = 8\ \mathrm{mm}, \qquad (1)$$

where $\lambda = 351$ nm is the UV operating wavelength of OMEGA. The resultant $\lambda_{\mathrm{pol}} = 8$ mm is the transverse distance required to cycle the polarization state from right-handed circular, to

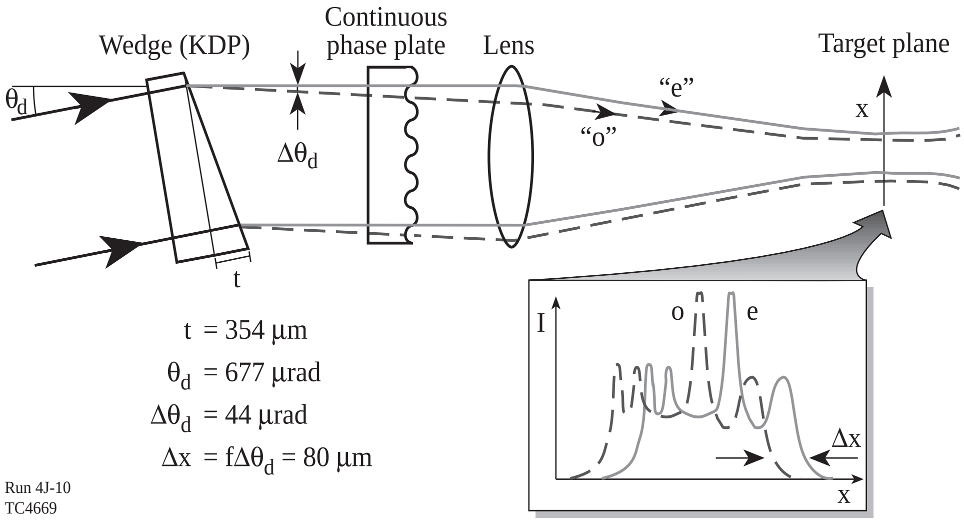

Figure 76.27
A birefringent KDP wedge achieves polarization smoothing and a theoretical $1/\sqrt{2}$ reduction in nonuniformity.

linear, to left-handed circular, back to linear, and returning to right-handed circular.

2. Induced Phase Perturbations

Two types of phase perturbation result from the introduction of a diamond-turned KDP wedge. The first is due to the residual scratch marks left behind by the diamond-turning process. The scratch marks cause a beam to acquire a pseudorandom phase perturbation as the beam passes through the front and back faces of the crystal. The pseudorandom phase perturbation can be described by a thin-optic transformation

$$\Phi_{\text{mill}} = k_0\left(n_{\text{KDP}} - 1\right) S(y), \tag{2}$$

where $S(y)$ is the depth of the scratch mark as a function of the transverse position y, $k_0 \equiv 2\pi/\lambda$ is the vacuum wave number, and n_{KDP} represents the refractive index for either the slow or fast wave.

The second type of phase perturbation arises during propagation because the nonlinear refractive index is a function of polarization state and intensity (see subsection 1 of the **Ellipticity** section) together with the fact that the KDP wedge produces a beam whose combined polarization state varies as a function of transverse position y. The nonlinear refractive index is a maximum for linear polarization and a minimum for circular polarization. Therefore, both orthogonally polarized beams accumulate a periodic phase perturbation during propagation that is greatest in the vicinity of linear polarization.

Both types of phase perturbation affect the beams by introducing spatial phase modulation that can then be converted into intensity modulation by virtue of the diffractive process that occurs during propagation. Intense beams can develop high-intensity spikes leading to filamentation damage through the coupled process of phase modulation and diffraction.

3. Model of Scratch Marks

The pseudorandom behavior of the residual scratch marks is modeled in this article by bandpass filtering a white noise source, viz.

$$S(y) = F^{-1}\left\{F\left[\Xi(\mathrm{y})\right] \bullet \operatorname{rect}\left(\frac{k_y - k_{y_0}}{k_{y_{\max}} - k_{y_{\min}}}\right)\right\},$$

$$\operatorname{rect}(x) = \begin{cases} 1; & |x| \le \dfrac{1}{2} \\ 0; & |x| > \dfrac{1}{2} \end{cases}, \tag{3}$$

where F represents the spatial Fourier transform, $\Xi(y)$ is the noise source, k_{y_0} is the central spatial wave number, and $k_{y_{\max}}$ and $k_{y_{\min}}$ represent the maximum and minimum passed spatial wave numbers. This result is sometimes referred to as "colored" noise.^{4} Figure 76.28 illustrates an example in which the passband was set to $2\pi/(4\text{ mm}) \le k_y \le 2\pi/(2\text{ mm})$. These data are used in the subsequent illustrative numerical simulations given in the **Numerical Results** section. This passband was selected since it covers the troublesome spatial frequencies identified by LLNL. Also, these data closely resemble surface profile measurements on a qualitative basis. An alternative function that completely describes the power spectral density of the scratch marks could be used in place of the

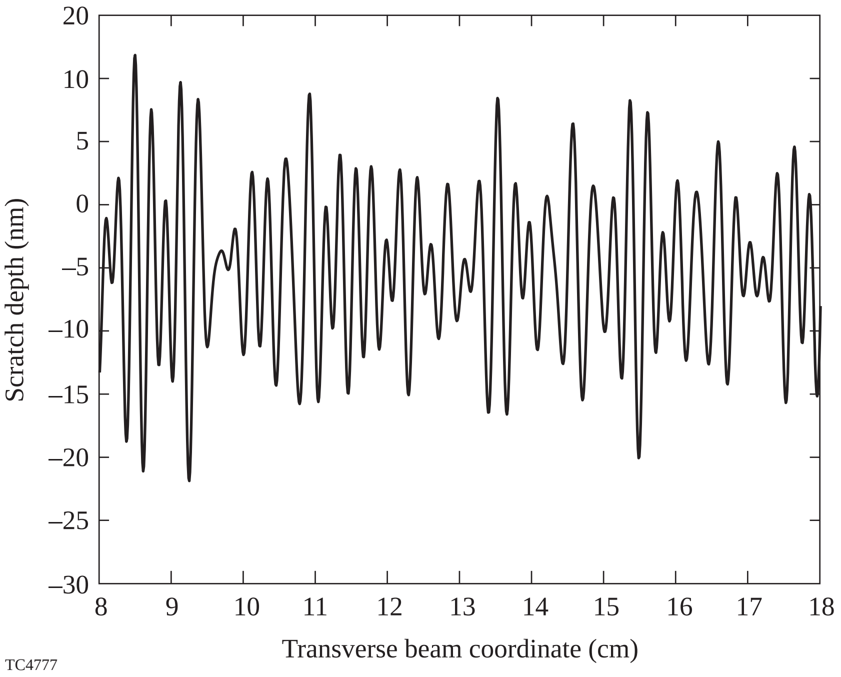

Figure 76.28
A bandpass-filtered pseudorandom noise source where the passband is set to $2\pi/(4\text{ mm}) \le k_y \le 2\pi/(2\text{ mm})$ and the peak-to-valley scratch depth is 40 nm.

rect(k_y) function. However, an adequate statistical description of the diamond-turned scratch marks is unavailable at this time. The rect(k_y) can be viewed as a worse-case situation that emphasizes the higher spatial frequencies since the actual power spectral density would go to zero in a continuous manner as the spatial frequency increases.

Nonlinear Wave Equation

The analysis of beam propagation for this problem assumes that the optical field is monochromatic and the bandwidth of the spatial spectrum is small relative to the vacuum wave number $k_0 = \omega_0/c$, where ω_0 is the angular frequency and c is the vacuum speed of light. This permits the slowly varying amplitude to be separated from the rapidly varying part, such that the electric field vector is given by

$$\mathbf{E}(y,z,t) = \frac{1}{2}\left[\hat{\mathbf{p}}E(y,z)\,e^{-i(\omega_0 t - k_0 n_0 z)} + c.c.\right], \tag{4}$$

where $E(y,z)$ is the slowly varying complex amplitude as a function of both the transverse distance y and propagation distance z, $\hat{\mathbf{p}}$ is the polarization vector, n_0 is the refractive index, and $c.c.$ indicates the complex conjugate. An arbitrary elliptical polarization state decomposes naturally into a weighted vector sum of right-handed and left-handed circular polarization states, viz.

$$\begin{aligned}\mathbf{E}&(y,z,t)\\ &= \frac{1}{2}\left\{\left[\hat{\mathbf{p}}_{\mathrm{RH}}E_{\mathrm{RH}}(y,z) + \hat{\mathbf{p}}_{\mathrm{LH}}E_{\mathrm{LH}}(y,z)\right]e^{-i(\omega_0 t - k_0 n_0 z)}\right.\\ &\quad \left. + \; c.c.\right\},\end{aligned} \tag{5}$$

where $E_{\mathrm{RH}}(y,z)$ and $E_{\mathrm{LH}}(y,z)$ are the complex amplitudes of the right-handed and left-handed circular polarization states, which are defined in terms of Cartesian components as

$$\begin{aligned} E_{\mathrm{RH}}(y,z) &= \frac{1}{\sqrt{2}}\left[E_x(y,z) - E_y(y,z)\right],\\ E_{\mathrm{LH}}(y,z) &= \frac{1}{\sqrt{2}}\left[E_x(y,z) + E_y(y,z)\right],\end{aligned} \tag{6}$$

and the polarization vectors are defined as

$$\hat{\mathbf{p}}_{\mathrm{RH}} \equiv \frac{1}{\sqrt{2}}(\hat{\mathbf{x}} + i\hat{\mathbf{y}}), \qquad \hat{\mathbf{p}}_{\mathrm{LH}} \equiv \frac{1}{\sqrt{2}}(\hat{\mathbf{x}} - i\hat{\mathbf{y}}). \tag{7}$$

The optical field is assumed to propagate in a lossless, isotropic nonlinear Kerr-like medium, where the nonlinear refractive index is given by

$$n = n_0 + \Delta n . \tag{8}$$

The quantity Δn represents the change in the refractive index beyond the low-intensity value n_0 and exhibits a linear dependence on the optical field intensity. The scalar nonlinear wave equation for each vector component is then given by

$$\frac{\partial E_{\mathrm{RH}}(y,z)}{\partial z} = \frac{i}{2k} \nabla_T^2 E_{\mathrm{RH}}(y,z) + ik_0\, \Delta n_{\mathrm{RH}}\, E_{\mathrm{RH}}(y,z), \tag{9}$$

$$\frac{\partial E_{\mathrm{LH}}(y,z)}{\partial z} = \frac{i}{2k} \nabla_T^2 E_{\mathrm{LH}}(y,z) + ik_0\, \Delta n_{\mathrm{LH}}\, E_{\mathrm{LH}}(y,z), \tag{10}$$

where $k = k_0 n_0$ and[5]

$$\Delta n_{\mathrm{RH}} = \frac{3}{4n_0}\Big[\chi_{xyxy}^{(3)} \left|E_{\mathrm{RH}}(y,z)\right|^2 + \left(\chi_{xyxy}^{(3)} + \chi_{xxyy}^{(3)}\right)\left|E_{\mathrm{LH}}(y,z)\right|^2\Big], \tag{11}$$

$$\Delta n_{\mathrm{LH}} = \frac{3}{4n_0}\Big[\chi_{xyxy}^{(3)} \left|E_{\mathrm{LH}}(y,z)\right|^2 + \left(\chi_{xyxy}^{(3)} + \chi_{xxyy}^{(3)}\right)\left|E_{\mathrm{RH}}(y,z)\right|^2\Big], \tag{12}$$

and it has been assumed that $\partial^2 E(y,z)/\partial z^2 = 0$, i.e., the slowly varying envelope approximation. The first terms in Eqs. (11) and (12) represent self-phase modulation, and the second group of terms represents cross-phase modulation. The vector components are coupled through the cross-phase modulation terms. Due to the symmetry of centrosymmetric Kerr-like media and the fact that both vector components share the same frequency ω_0, there are only two independent third-order susceptibility constants $\chi_{xyxy}^{(3)}$ and $\chi_{xxyy}^{(3)}$ that obey the relation $\chi_{xxxx}^{(3)} = 2\chi_{xyxy}^{(3)} + \chi_{xxyy}^{(3)}$ and follow the frequency convention $\chi_{xyxy}^{(3)}(-\omega,-\omega,\omega,\omega)$. (Notice that it is this convention that causes the subtle notational deviation from that of Sutherland.[5]) Either scalar nonlinear wave equation, Eq. (9) or Eq. (10), can be written in operator form as[6]

$$\frac{\partial E(y,z)}{\partial z} = \left(\hat{D} + \hat{N}\right) E(y,z), \tag{13}$$

where the operator $\hat{D}$ accounts for diffraction and is defined as

$$\hat{D} \equiv \frac{i}{2k} \nabla_T^2 , \tag{14}$$

the operator $\hat{N}$ governs media nonlinearities and is defined as

$$\hat{N} \equiv ik_0 \Delta n , \tag{15}$$

the quantity $E(y,z)$ represents either the right-handed or left-handed complex amplitude, and Δn represents either Eq. (11) or Eq. (12). The formally exact solution of Eq. (13) is given by

$$E(y, z + \Delta z) = e^{i\left(\hat{D}+\hat{N}\right)\Delta z}\, E(y,z).$$

An important merit of decomposing an arbitrary elliptical polarization state into right-handed and left-handed circular polarization states is that

$$\frac{\partial \left|E_{\mathrm{RH}}(y,z)\right|^2}{\partial z} = 0 \quad \text{and} \quad \frac{\partial \left|E_{\mathrm{LH}}(y,z)\right|^2}{\partial z} = 0 .$$

This implies that the intensities of the vector components and therefore the quantity Δn are all constants of motion. This is not true for a Cartesian decomposition, due to the well-known cross-phase modulation effect of ellipse rotation, which causes the magnitudes along the Cartesian components to change with propagation distance.[7]

1. Ellipticity and the Nonlinear Refractive Index

The ellipticity parameter η covers the range $-\pi/4 \le \eta \le \pi/4$, where $\tan(\eta)$ describes the ratio of the minor and major axes of the polarization ellipse with the sign defining its handedness [positive (+) indicates right-handed and negative (–) indicates left-handed].[7] When $\eta = 0$, the polarization state is linear and, when $|\eta| = \pi/4$, the polarization state is circular. Equations to calculate the lengths of the major and minor axes can be found in Oughstun[8] (see Ref. 8, Sec. 4.2.1) and are governed by the complex amplitudes $E_{\mathrm{RH}}(y,z)$ and $E_{\mathrm{LH}}(y,z)$. Consequently, the ellipticity parameter η is also a function of the complex amplitudes $E_{\mathrm{RH}}(y,z)$ and $E_{\mathrm{LH}}(y,z)$. The quantities Δn_{RH} and Δn_{LH} depend on the magnitudes $\left|E_{\mathrm{RH}}(y,z)\right|$ and $\left|E_{\mathrm{LH}}(y,z)\right|$ and are indirectly functions of the polarization state.

The extrema of the quantities Δn_{RH} and Δn_{LH} occur when the polarization state is either linear or circular. If the polarization state is linear, then $|E_{\mathrm{lin}}|^2 = 2|E_{\mathrm{LH}}|^2 = 2|E_{\mathrm{RH}}|^2$ (where the factor of 2 comes from the equal intensity split into both polarization states), and the change in the nonlinear refractive index becomes

$$\Delta n_{\mathrm{lin}} = \frac{3}{8n_0}\left[\chi^{(3)}_{xxyy} + 2\chi^{(3)}_{xyxy}\right]|E_{\mathrm{lin}}|^2 . \tag{16}$$

If the polarization state is circular, either right-handed or left-handed, then

$$\Delta n_{\mathrm{cir}} = \frac{3}{4n_0}\chi^{(3)}_{xyxy}|E_{\mathrm{cir}}|^2 . \tag{17}$$

In either of these two degenerate states $|E_{\mathrm{lin}}|^2 = |E_{\mathrm{cir}}|^2$ so that

$$\Delta n_{\mathrm{lin}} > \Delta n_{\mathrm{cir}} . \tag{18}$$

In a more general sense, the nonlinear refractive index is larger in the vicinity surrounding, or in the immediate neighborhood of, the points of linear polarization relative to the minimum values attained at the points of right-handed or left-handed circular polarization.

2. Angular Spectrum Representation

If nonlinear effects can be neglected, the vector components become decoupled and obey the scalar Helmholtz wave equations given by

$$\nabla^2 E(y,z) + k_0^2\, n^2\, E(y,z) = 0 , \tag{19}$$

which has an exact solution at any exit plane $z+\Delta z$ given by the angular spectrum representation (see Ref. 9, Sec. 3.7), viz.

$$E(y,z+\Delta z) = \frac{1}{2}\pi \int_{-\infty}^{\infty} \tilde{E}(k_y,z)\, e^{i\Delta z\sqrt{k_0^2 n^2 - k_y^2}}\; e^{ik_y y}\, dk_y , \tag{20}$$

where $\tilde{E}(k_y,z)$ is the spatial Fourier transform at the entrance plane z and is defined by

$$\tilde{E}(k_y,z) = \int_{-\infty}^{\infty} E(y,z)e^{-ik_y y}dy . \tag{21}$$

3. Self- and Cross-Phase Modulation

If diffraction can be neglected, the scalar nonlinear wave equation for either vector component has the simple form

$$\frac{\partial E(y,z)}{\partial z} = \hat{N}E(y,z), \tag{22}$$

which has a solution given by

$$E(y,z+\Delta z) = E(y,z)e^{ik_0\Delta n\Delta z} , \tag{23}$$

because the quantity Δn is not a function of the propagation distance for a circular-polarization decomposition. As a result, the nonlinear effects of self- and cross-phase modulation, acting alone, induce a simple phase accumulation that is a function of both the polarization state and intensity. This is a generalization of the well-known *B*-integral.

Numerical Approach

The numerical split-step Fourier method (see Ref. 6, Sec. 2.4.1) is used to solve the differential Eq. (13), where the total required distance of propagation is divided into small steps over which the linear effects of diffraction are treated separately from the nonlinear effects of self- and cross-phase modulation. This permits the solutions given by Eqs. (20) and (23) to be used if the chosen step size is sufficiently small that the linear and nonlinear effects are approximately independent over that step.

The numerical calculation over one small step Δz is referred to as a propagation step. One propagation step entails the independent calculation of diffraction using the results of Eq. (20) and the independent calculation of the nonlinear phase accumulation as described by Eq. (23). The detailed manner in which this is carried out greatly affects the overall error achieved and directly affects the required number of steps needed to obtain a suitable level of accuracy. For example, if a full diffraction step is followed by a full nonlinear step, the error is $O\{\Delta z^2\}$, which is equivalent to solving Eq. (13) as

$$E(y,z+\Delta z) \cong e^{i\Delta z\hat{D}}e^{i\Delta z\hat{N}}E(y,z). \tag{24}$$

However, if a half diffraction step is followed by a full nonlinear step and then by another half diffraction step, the error is $O\{\Delta z^3\}$, which is equivalent to solving Eq. (13) as

$$E(y,z+\Delta z) \cong e^{i\frac{\Delta z}{2}\hat{D}}e^{i\Delta z\hat{N}}e^{i\frac{\Delta z}{2}\hat{D}}E(y,z). \tag{25}$$

The errors associated with Eqs. (24) and (25) are found by comparing these approximate solutions to the formally exact solution to Eq. (13) and applying the Baker–Hausdorff formula for two noncommuting operators.[6] The method described by Eq. (25), known as the symmetrized split-step Fourier method, is employed for the numerical simulations in the subsequent section. Figure 76.29 graphically represents this particular approach over two small steps of Δz.

Numerical Results

The intent of this investigation is to isolate the effects caused by the nonlinear propagation in air, the scratch marks, and the wedged shape of the KDP crystal, while ignoring the nonlinear index of KDP. To this end, only the exit face of the KDP crystal is considered to be scratched, and the initial beam shape is regarded as infinitely smooth. As a consequence, the nonlinear ripple growth within the KDP crystal can be neglected.

The beam shape is modeled by using spatially offset hyperbolic-tangent step functions, viz.

$$E(y) = \frac{1}{2}\left\{\tanh\left[100(y+0.14)\right] - \tanh\left[100(y-0.14)\right]\right\}, \qquad (26)$$

which yields an infinitely smooth, 28-cm-diam beam. The nominal intensity level for OMEGA equal to 1.3 GW/cm^2 is used. Also, an unrealistic value of 10.3 GW/cm^2 is used to demonstrate a regime where the nonlinear effects dominate since, as it will be shown, the nonlinear effects are small for the nominal OMEGA intensity level. The measure of intensity modulation used in this paper is the contrast defined as

$$\text{Contrast} = \frac{\max\{I(y)\}}{\text{mean}\{I(y)\}}, \qquad (27)$$

where the transverse position y, for this formula only, covers the region where $I(y)$ was initially at full value; thus, the region where the beam intensity tapers to zero is not considered for this statistic.

1. Material Parameters

The material parameters used in the simulations are given in this subsection. The linear refractive indices for the KDP crystal are $n_{\text{KDP}_o} = 1.532498$ for the ordinary wave and $n_{\text{KDP}_e} = 1.498641$ for the extraordinary wave, which propagates at 59° to the optic axis. The third-order nonlinear susceptibility constants for air are

$$\chi^{(3)}_{xyxy}(-\omega,-\omega,\omega,\omega) = 28.16 \times 10^{-19} \text{ esu}$$

and

$$\chi^{(3)}_{xxyy}(-\omega,-\omega,\omega,\omega) = 172.4 \times 10^{-19} \text{ esu}\cdot$$

The third-order susceptibility constants are four times those given in Ref. 10, due to the particular definitions they used for the polarization vector and intensity, as noted by Sutherland [see Ref. 5, p. 298]. There is a compensatory factor of 1/4 in the definition of Δn used in this article, which effectively balances this deviation.

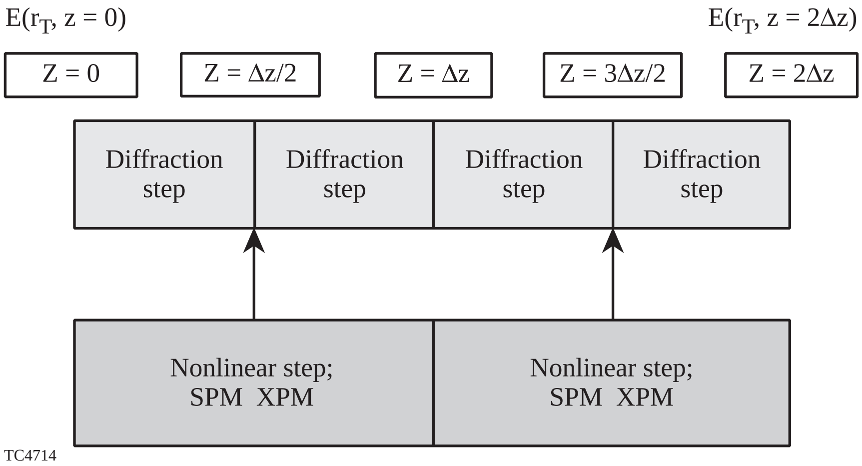

Figure 76.29
Two propagation steps of the symmetrized split-step Fourier method covering a distance of $2\Delta z$.

2. Enhancement of Linear Polarization

As was mentioned in subsection 1 of the **Nonlinear Wave Equation** section, the phase accumulation is greatest in the vicinity surrounding points of linear polarization. When diffraction is included, these areas tend to focus and correspond to peaks of intensity modulation. To illustrate this effect, a simulation was carried out modeling a KDP wedge with an optically smooth surface, i.e., without an initial pseudorandom phase perturbation. Due to the wedge and the dependence of the nonlinear refractive index on the polarization state, a ripple is introduced with a wavelength 1/2 λ_{pol} (where the factor of 1/2 emphasizes that the overall phase perturbation of both orthogonal beams has extrema at the transverse positions corresponding to linear or circular polarization that are independent of the handedness), which can lead to small-scale self-focusing if the beam intensity is high enough. This is contrary to what would be expected in the absence of a wedge; with a perfectly smooth beam and an optically smooth KDP surface, one would observe only a rotation of the polarization ellipse (except in the degenerate cases when the whole beam is either linearly or circularly polarized) and possibly whole-beam self-focusing. This simulation was run with an input intensity of 10.3 GW/cm^2 and yielded a contrast of 1.31. These results are presented in Fig. 76.30, where a correlation between the peak intensities and the linear polarization is evident by the location of the square symbols. If the intensity were lowered to the nominal OMEGA level, a small contrast of only 1.04 would be calculated.

The enhancement of linear polarization may be amplified or seeded by the presence of scratch marks on the surface of the KDP wedge. This effect can be understood by running a simulation that accounts only for diffraction. In this situation there is, of course, no correlation between the intensity peaks that develop during propagation and the polarization state. Some intensity peaks, however, are inevitably located in the neighborhood of linear polarization. These intensity peaks seed the nonlinear growth by increasing the associated phase accumulation in these regions as described by Eq. (23) and, as a consequence, induce a greater intensity modulation than observed for the optically smooth wedge.

A simulation for the nominal OMEGA laser intensity, including both linear and nonlinear effects, yielded a contrast of 1.32 and is presented in Fig. 76.31(a). In this case, only a slight correlation exists between the intensity peaks and the linear polarization state due to the weak nonlinear effect. When the intensity level is increased to 10.3 GW/cm^2, however, an appreciable growth is observed in the vicinity of linear polarization [as shown in Fig. 76.31(b)], and, consequently, a

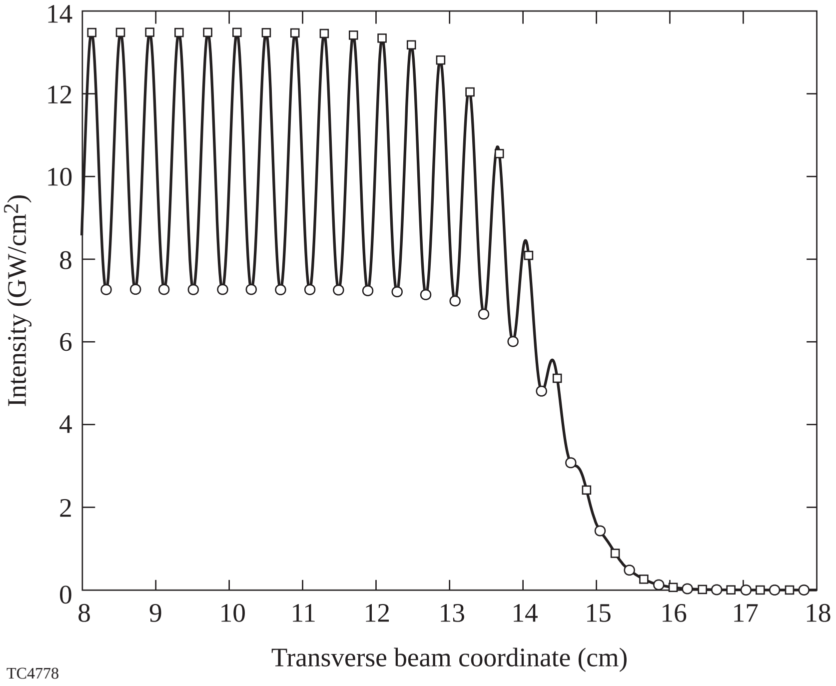

Figure 76.30
The simulation of propagating 12 m past an optically smooth KDP wedge with an incident intensity level of 10.3 GW/cm^2. A contrast of 1.31 is observed. Squares and circles indicate positions of linear and circular polarization, respectively.

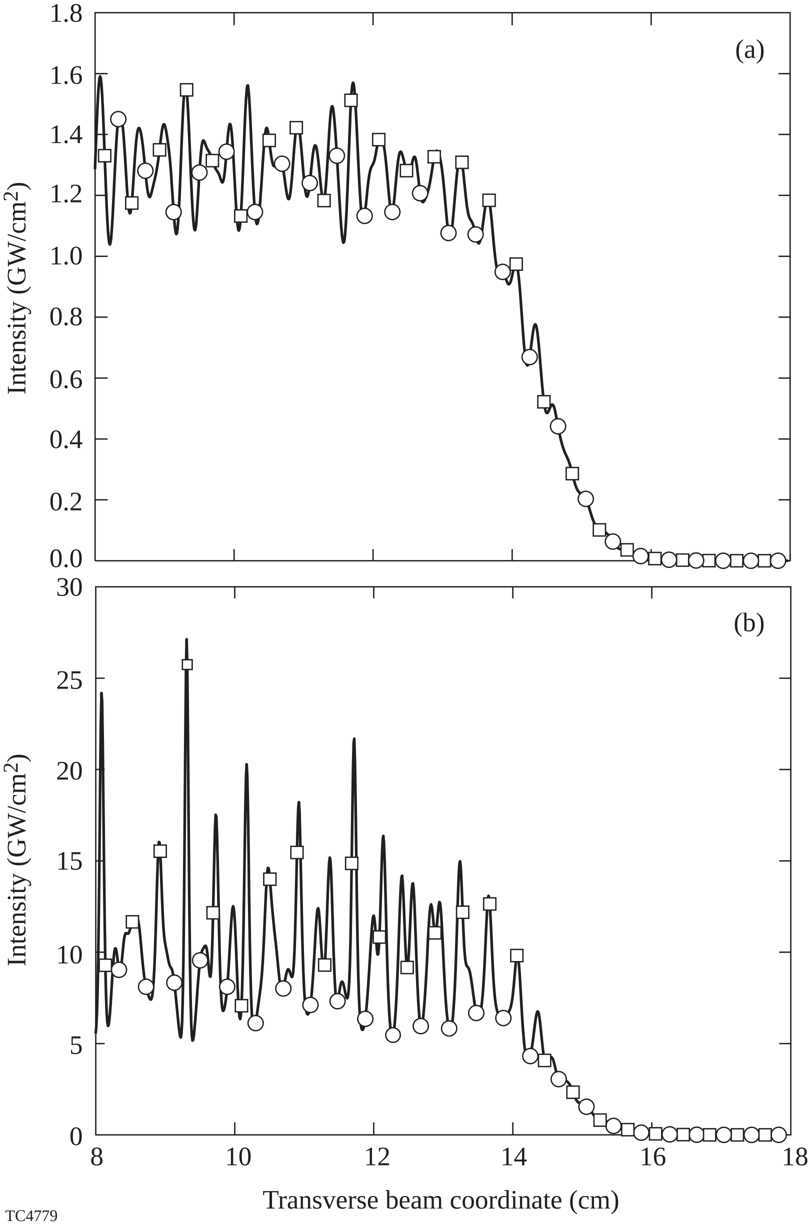

Figure 76.31
The simulation of nonlinear propagation through 12 m of air past a pseudorandomly scratched KDP wedge with 40-nm peak-to-valley scratch depth and a passband of $2\pi/(4\text{ mm}) \le k_y \le 2\pi/(2\text{ mm})$ (a) at 1.3 GW/cm^2 and (b) at 10.3 GW/cm^2. The resulting contrast is 1.32 in (a) and 2.63 in (b). Squares and circles indicate positions of linear and circular polarization, respectively.

significant correlation exists between the intensity peaks and these regions as indicated by the association of the majority of the square symbols with the intensity peaks.

3. Contrast Calculations at the Nominal OMEGA Intensity Level

Tables 76.I and 76.II contain contrast data calculated from simulations of linear and nonlinear propagation, respectively, in which the same scratch-depth data presented in Fig. 76.28 was scaled to cover the 10-nm to 50-nm range for an incident intensity level of 1.3 GW/cm^2. The scratch-depth range presented here was chosen to correspond to the range of surface profile measurements that were taken on diamond-turned KDP crystals, which yielded peak-to-valley scratch depths of 40 nm (worst case) and 15 nm (best case). These tables also include calculated contrast data for three additional passband configurations: the passband is narrowed to $k_y = 2\pi/(3\text{ mm})$, widened to $2\pi/(100\text{ mm}) \le k_y \le 2\pi/(1\text{ mm})$ and widened to a low pass of $k_y \le 2\pi/(1\text{ mm})$.

If the scratch mark model given in Eq. (3) is extended to include another spatial dimension, a 2-D colored noise source is modeled. A 2-D beam is then modeled by extending Eq. (26) to include another dimension. Both of these models are then used to simulate 2-D nonlinear beam propagation in an analogous manner to the 1-D case. The plot presented in Fig. 76.32 shows three lineouts from a 2-D simulation (taken at the center and near the edges of the beam) for a beam with an intensity of 1.3 GW/cm^2, a scratch-mark passband of $2\pi/(4\ \mathrm{mm}) \le k_x, k_y \le 2\pi/(2\ \mathrm{mm})$, and a peak-to-valley scratch depth of 40 nm. The contrast calculated for the whole 2-D beam is 1.35, compared to the value of 1.32 given in Table 76.II for the corresponding 1-D case.

At the nominal OMEGA intensity level of 1.3 GW/cm^2, a contrast ratio of 1.8:1 represents the damage threshold of the final optics. The data in Table 76.II show that the calculated contrast values are well below this threshold even for grating-type sinusoidal scratch marks. Recent linear intensity modulation measurements taken on diamond-turned KDP crystals yielded a range of contrast values between 1.04 to 1.08, which roughly correlates with the linear propagation simulation results for peak-to-valley scratch depths between 10 and 20 nm and a passband of $2\pi/(100\ \mathrm{mm}) \le k_y \le 2\pi/(1\ \mathrm{mm})$ given in Table 76.I. The corresponding contrast range in Table 76.II for nonlinear propagation is 1.07 to 1.11, which represents a small increase due to the nonlinear effects. Near-field images were taken during OMEGA full-power shots on a beamline with and without a diamond-turned KDP plate at an equivalent plane of the final focusing optics. In this experiment, a negligible increase in the intensity modulation was observed, corroborating the results of these numerical simulations.

Conclusion

On the basis of realistic simulations, including diffraction and nonlinear self- and cross-phase modulation, and a realistic representation of scratch marks on diamond-turned KDP, it has been found that KDP wedges, diamond-turned or smooth, are not a significant source of intensity modulation. These results are consistent with experimental results from full-power shots. Accordingly, polarization smoothing will be implemented on OMEGA using diamond-turned rather than polished KDP.

Table 76.I: The calculated value of contrast for linear propagation through 12 m of air past a scratched KDP wedge at an incident intensity level of 1.3 GW/cm^2 for different scratch depths and filter types.

Peak-to-Valley Scratch Depth (nm)	Sinusoidal $k_y = 2\pi/(3\ \mathrm{mm})$	Random Lowpass $k_y \le 2\pi/(1\ \mathrm{mm})$	Random Bandpass $2\pi/(1\ \mathrm{mm}) \le k_y \le 2\pi/(1\ \mathrm{mm})$	Random Bandpass $2\pi/(4\ \mathrm{mm}) \le k_y \le 2\pi/(2\ \mathrm{mm})$
10	1.08	1.03	1.04	1.06
20	1.16	1.07	1.08	1.11
30	1.23	1.11	1.11	1.17
40	1.31	1.14	1.14	1.23
50	1.38	1.18	1.19	1.28

Table 76.II: The calculated value of contrast for nonlinear propagation through 12 m of air past a scratched KDP wedge at an incident intensity level of 1.3 GW/cm^2 for different scratch depths and filter types.

Peak-to-Valley Scratch Depth (nm)	Sinusoidal $k_y = 2\pi/(3\ \mathrm{mm})$	Random Lowpass $k_y \le 2\pi/(1\ \mathrm{mm})$	Random Bandpass $2\pi/(1\ \mathrm{mm}) \le k_y \le 2\pi/(1\ \mathrm{mm})$	Random Bandpass $2\pi/(4\ \mathrm{mm}) \le k_y \le 2\pi/(2\ \mathrm{mm})$
10	1.13	1.07	1.07	1.11
20	1.23	1.09	1.11	1.18
30	1.32	1.13	1.16	1.25
40	1.41	1.17	1.19	1.32
50	1.50	1.20	1.25	1.38

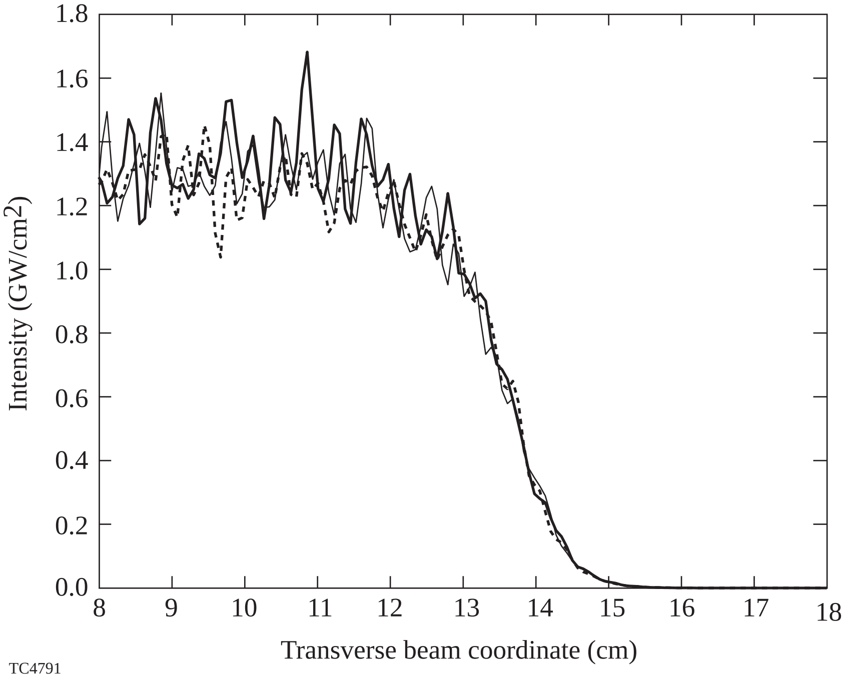

Figure 76.32
Three lineouts from a 2-D simulation (taken at the center and near the edges of the beam) of nonlinear beam propagation with a 1.3 GW/cm^2 intensity, through 12 m of air, past a pseudorandomly scratched KDP wedge with 40-nm peak-to-valley scratch depth and a passband of $2\pi/(4\text{ mm}) \le k_x, k_y \le 2\pi/(2\text{ mm})$. An overall contrast of 1.35 is observed.

ACKNOWLEDGMENT

The author thanks Prof. G. Agrawal for his expert advice and direction, Dr. John Kelly for suggesting this project and the in-depth discussions that followed, and Dr. Stephen Craxton for many useful discussions and time spent editing this manuscript. This research was supported by NSF Grant PHY94-15583. In addition, this work was partially supported by the U.S. Department of Energy Office of Inertial Confinement Fusion under Cooperative Agreement No. DE-FC03-92SF19460, the University of Rochester, and the New York State Energy Research and Development Authority. The support of DOE does not constitute an endorsement by DOE of the views expressed in this article.

REFERENCES

1. K. Kato, unpublished (1984).
2. Laboratory for Laser Energetics LLE Review **45**, 1, NTIS document No. DOE/DP40200-149 (1990). Copies may be obtained from the National Technical Information Service, Springfield, VA 22161.
3. S. Skupsky, R. W. Short, T. Kessler, R. S. Craxton, S. Letzring, and J. M. Soures, J. Appl. Phys. **66**, 3456 (1989).
4. A. B. Carlson, *Communication Systems: An Introduction to Signals and Noise in Electrical Communication*, McGraw-Hill Electrical and Electronic Engineering Series (McGraw-Hill, New York, 1968), p. 154.
5. R. L. Sutherland, *Handbook of Nonlinear Optics*, Optical Engineering, Vol. 52 (Marcel Dekker, New York, 1996).
6. G. P. Agrawal, *Nonlinear Fiber Optics*, Optics and Photonics Series, 2nd ed. (Academic Press, San Diego, 1995).
7. Ts. Gantsog and R. Tanas, J. Mod. Opt. **38**, 1537 (1991).
8. K. E. Oughstun and G. C. Sherman, *Electromagnetic Pulse Propagation in Causal Dielectrics*, Springer Series on Wave Phenomena, Vol. 16 (Springer-Verlag, Berlin, 1994).
9. J. W. Goodman, *Introduction to Fourier Optics* (McGraw-Hill, New York, 1968).
10. R. W. Hellwarth, D. M. Pennington, and M. A. Henesian, Phys. Rev. A **41**, 2766 (1990).

X-Ray Radiographic System Used to Measure the Evolution of Broadband Imprint in Laser-Driven Planar Targets

In an inertial confinement fusion (ICF) implosion, the target is hydrodynamically unstable, and, as a result, mass modulations in the target (either existing or created) can grow to be large enough to disrupt the implosion, thereby reducing its thermonuclear yield.[1] In direct-drive ICF, the nonuniformities in the drive laser can create mass modulations in the target by a process called laser imprinting. As the target accelerates, these mass modulations can grow exponentially, creating large perturbations in the target shell. Understanding and controlling laser imprinting are critical to the successful design of a high-gain ICF target. The primary method of studying imprinting is through-foil x-ray radiography of laser-accelerated targets, where the growth of these mass modulations can be observed.[2] Planar targets are used because they are easily diagnosed and are a reasonable approximation to the early portions of a spherical implosion.

Our experiments use multiple laser beams to drive the subject target and to produce x rays on another target.[3] These x rays are filtered and imaged after they traverse the driven target. Modulations in these images are related to the optical depth (or density–thickness product) of the target. By properly interpreting these images, the character of the imprinted features and their temporal evolution are studied. To accomplish this, the instrumentation must be properly characterized.

A direct measurement of the initial imprinted perturbations is difficult because of their low amplitudes. Additional complications result from the propagation effects of nonuniform shock waves.[4–6] Low-amplitude imprinting has been measured directly using an XUV laser to probe target nonuniformities produced by a laser on very thin (~2 to 3 μm) silicon and aluminum targets.[7] The present experiments use 20-μm-thick CH targets that closely resemble the target shells normally used on OMEGA spherical implosions. These experiments are closely related to those that measure the growth of preimposed mass perturbations,[4] which were well simulated by hydrocodes, providing confidence that both the energy coupling and amount of unstable growth are well modeled for these experiments. This provides a baseline calibration for various hydrodynamic effects that occur in the imprinting experiments. A caveat for these experiments is that imprinting is not directly measured; rather, some unstable RT growth is needed to amplify the perturbations to detectable levels.

It should also be noted that the hydrodynamic instabilities studied here exist primarily at the ablation surface, the point where the steep temperature front meets the overdense material produced by the shock. Perturbations in the target result from both mass modulations (ripples on the ablation surface) and density modulations produced in the bulk of the target. The latter are created primarily by the propagation of nonuniform shocks. Radiographic systems are sensitive to the density–thickness product (optical depth) of the target and, as such, cannot distinguish between mass and density modulations. After about 1 ns of acceleration in these experiments, the variations in optical depth produced by the nonuniform shocks become negligible, compared to those produced by the ablation-front amplitude. At this point, it is reasonable to ascribe most of the measured optical depth to the amplitude of the perturbation at the ablation surface.[4]

The backlighting source typically has multiple spectral components. As a result, simulations of the resultant optical depth of the target are critical to interpreting the data. This worked extremely well for experiments using two-dimensional preimposed sinusoidal perturbations.[4,8] In contrast, the features created by imprinting are three dimensional and significantly more difficult to simulate. It is advantageous, therefore, to obtain experimentally a relationship between measured optical-depth modulations and the amplitude of ablation-surface modulations. We simplify the latter process by establishing several reasonable assumptions about the detection system.

In the following sections, we discuss the radiographic imaging system and methods to recover the target perturbations from the radiographs. We present results of experiments that characterize the sensitivity, resolution, and noise of the system. Using this information, we have formulated a Wiener filter that is designed to enhance the radiographic images. In essence, our analysis provides a way to distinguish signal from noise and to deconvolve the system resolution.

Experimental Configuration

Unperturbed (smooth surface), 20-μm-thick CH (ρ = 1.05 g/cm^3) targets were irradiated at 2×10^{14} W/cm^2 in 3-ns square pulses by five overlapping UV beams (see Fig. 76.33). The targets were backlit with x rays produced by a uranium backlighter, located 9 mm away from the driven target and irradiated at ~1×10^{14} W/cm^2 (using 12 additional beams). X rays transmitted through the target and a 3-μm-thick Al blast shield (located at the center between the backlighter and drive foils) were imaged by 8-μm pinholes on a framing camera filtered with 6 μm of aluminum. This yielded the highest sensitivity for an average photon energy of ~1.3 keV. The framing camera produced eight images of ~80-ps duration, each occurring at different times. The distance between the target and the pinhole array was 2.5 cm, and the distance between the pinhole array and the framing camera was 35 cm, resulting in a magnification of ~14. The use of optical fiducial pulses coupled with an electronic monitor of the framing-camera output produced a frame-timing precision of about 70 ps. The framing-camera output is captured on Kodak T-Max 3200 film, which is then digitized with a Perkin–Elmer PDS microdensitometer with a 20-μm-square scanning aperture.

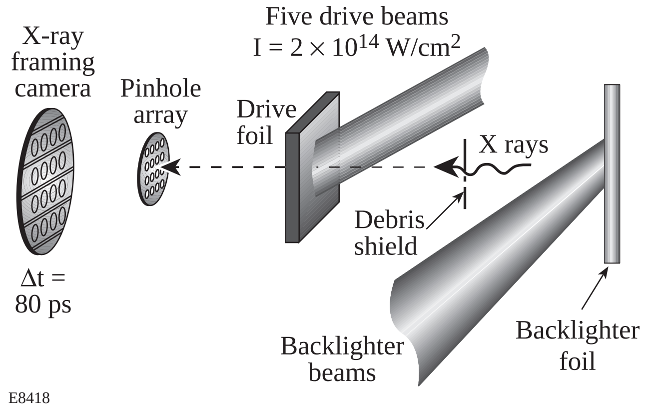

Figure 76.33
Experimental configuration. Five overlapped beams drive a 20-μm CH foil. An additional 12 beams produce x rays from a uranium backlighter foil. X rays traverse the target and are imaged by a pinhole array on a framing camera.

Figure 76.34 shows a block diagram of the entire detection system, which comprises four major parts: an 8-μm pinhole, the framing camera with a microchannel plate (MCP) and phosphor plate, the film, and the digitization process. At each stage of the measurement, noise is added to the signal, and the signal plus noise are convolved with the point spread function (PSF) of each component of the system. In the frequency domain, the spectra of both the signal and the noise are multiplied by a modulation transfer function (MTF) of that subset of the imaging system.

In radiography, x rays with a nominally wide spectrum are attenuated exponentially by the target being probed. In addition to the target, there are filters and imaging devices that affect the transmission of x rays to the detector. Figure 76.35 (thick line) shows a backlighter uranium spectrum used for imaging.[2] The spectral response function of the imaging system (Fig. 76.35, thin line) includes the transmission of

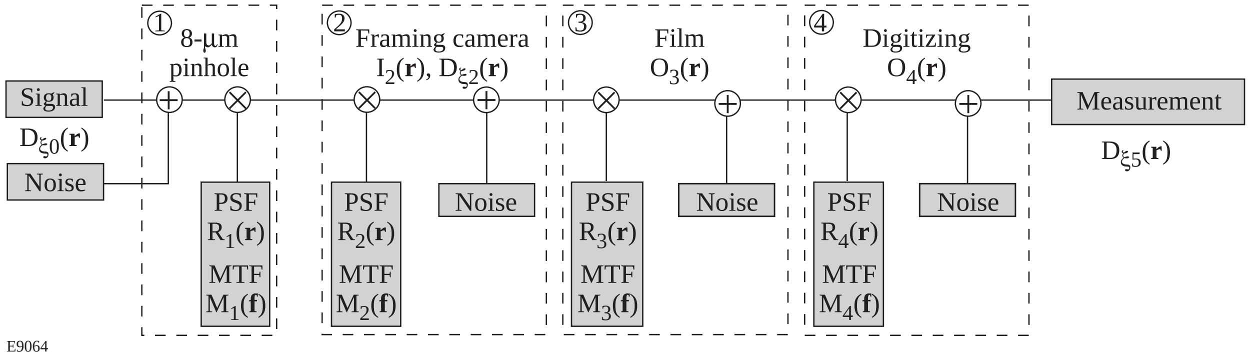

Figure 76.34
Block diagram of the experimental detection system. This system comprises four major parts: an 8-μm pinhole, the framing camera, the film, and the digitization. At each stage of the measurement, noise is added to the signal, and the signal with noise are convolved with the PSF. $D_{\xi 0}(\mathbf{r})$, $D_{\xi 2}(\mathbf{r})$, and $D_{\xi 5}(\mathbf{r})$ are the optical depth modulations in the target, in the framing camera's output, and as measured, respectively. $I_2(\mathbf{r})$ is the light intensity in the framing camera's output. $O_3(\mathbf{r})$ and $O_4(\mathbf{r})$ are the optical density of the film, before and after digitization, respectively.

aluminum filters and mass absorption rate of a gold photocathode on the microchannel plate (MCP) in the framing camera. Figure 76.36 shows the spectrum used for imaging, absorbed and converted into electrons by the MCP. It is obtained by multiplying the two curves in Fig. 76.35 together, taking the attenuation of 20 μm CH into account. The output of the framing camera is proportional to the convolution of the x-ray spectral intensity incident on a target, its attenuation factor, and the PSF's of the pinhole $R_1(\mathbf{r},E,t)$ and the framing camera $R_2(\mathbf{r},E,t)$, including filters, where E represents x-ray energy. Assuming that no saturation occurs in these devices, the output intensity of the framing camera incident on the film is

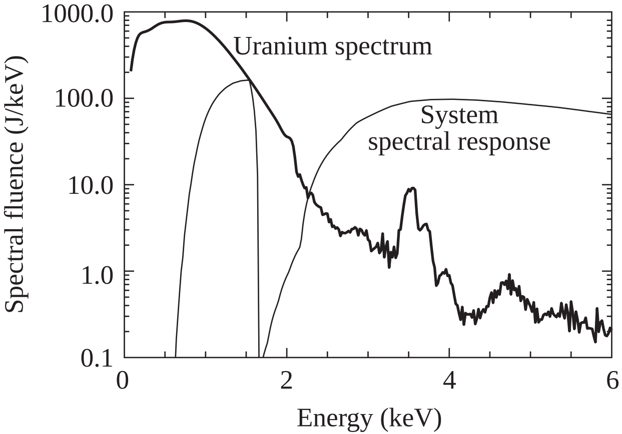

E9172

Figure 76.35
Uranium spectrum (thick solid line) and instrumental response (thin solid line) as functions of x-ray energy.

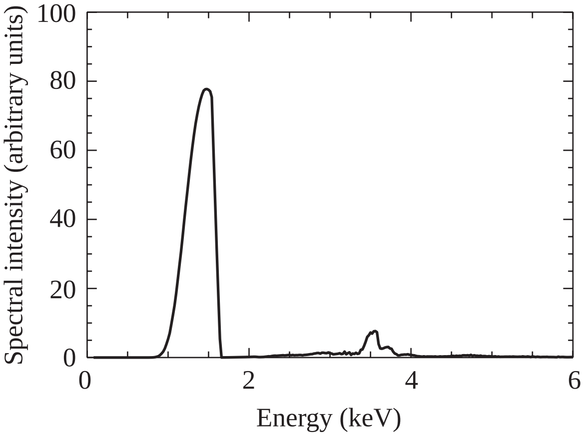

E9183

Figure 76.36
X-ray spectrum propagated through a 3-μm Al blast shield, a 20-μm CH target, and a 6-μm Al filter on the MCP, then absorbed and converted into electrons by the MCP.

$$\begin{aligned} I_2(\mathbf{r},t) &\sim \int dE \int d\mathbf{r}' \\ &\times R_{1,2}(\mathbf{r}-\mathbf{r}',E,t)\, f_{\mathrm{Al}}(E,t)\mu_{\mathrm{Au}}(E)\, S_{\mathrm{bklt}}(\mathbf{r}',E,t) \\ &\times \exp\left[-\int_0^{z_0} dz'\mu_{\mathrm{CH}}(E,t)\,\rho(\mathbf{r}',z',t)\right] \\ &\times \exp\left[-\mu_{\mathrm{CH}}(E,t)\,\rho_{\mathrm{abl}}(t)\,\xi(\mathbf{r}',t)\right]. \end{aligned} \tag{1}$$

In this equation, x rays propagate along the target normal, which is oriented along the z axis. The coordinate $\mathbf{r}$ is the position vector perpendicular to that axis; $I_2(\mathbf{r},t)$ is the output intensity of the framing camera; $R_{1,2}(\mathbf{r},E,t)$ is a point spread function of a pinhole and framing cameras, which is, in general, a function of the x-ray energy E; $f_{\mathrm{Al}}(E,t)$ is the aluminum filter transmission; $\mu_{\mathrm{Au}}(E)$ is the mass absorption rate of the gold photocathode (in the MCP); and $S_{\mathrm{bklt}}(\mathbf{r},E,t)$ is a backlighter spectral intensity. The target density and thickness are $\rho(\mathbf{r},z,t)$ and $z_0(t)$, respectively. The target density and the amplitude of the target thickness modulation at the ablation surface are $\rho_{\mathrm{abl}}(t)$ and $\xi(\mathbf{r},t)$. The mass absorption rate of the CH target is $\mu_{\mathrm{CH}}(E,t)$.

The film converts the incident light intensity $I_2(\mathbf{r},t)$ into the film optical density $O_3(\mathbf{r},t)$ according to its sensitivity [or D log(H)] curve W. Convolving that with the PSF of the film $R_3(\mathbf{r})$ yields

$$\begin{aligned} & O_3(\mathbf{r},t) \\ &= \int d\mathbf{r}' R_3(\mathbf{r}-\mathbf{r}')\, W\left\{\log_{10}\left[\int_{t-\tau/2}^{t+\tau/2} dt' I_2(\mathbf{r}',t')\right]\right\}, \end{aligned} \tag{2}$$

where $\tau = 80$ ps is a time resolution of the framing camera. During film digitization, the optical density $O_3(\mathbf{r},t)$ is convolved with the PSF $R_4(\mathbf{r})$ of the 20-μm-square aperture in the densitometer to give the digitized or measured optical density

$$O_4(\mathbf{r},t) = \int d\mathbf{r}' R_4(\mathbf{r}-\mathbf{r}')\, O_3(\mathbf{r}'). \tag{3}$$

The measured optical density of the film, $O_4(\mathbf{r},\mathrm{t})$, is converted to intensity using the inverse film sensitivity W^{-1}. The measured optical depth $D_5(\mathbf{r},t)$ of the target is obtained by taking the natural logarithm of that intensity-converted image:

$$D_5(\mathbf{r},t) = \ln\left\{10^{W^{-1}[O_4(\mathbf{r},t)]}\right\}. \tag{4}$$

The primary objective of this experiment is to recover the amplitude of the perturbation at the ablation surface using the measured optical depth modulations. To do this rigorously requires significant effort. Several aspects of the imaging system enable assumptions, however, that greatly simplify the analysis of the radiographic images: (1) As a result of Al filters, a relatively narrow band ($\Delta E \simeq 200$ eV) of x rays around 1.3 keV is used for radiography. The effect of the spectral component of uranium *M*-band emission around 3.5 keV (see Fig. 76.36) on system sensitivity and resolution was measured and calculated to be insignificant. (2) The backlighter spectrum and filter transmission remain constant in time during the measurement. (3) The backlighter is produced by 12 beams that have phase plates, resulting in a very uniform and predictable backlighter shape. (4) There is little heating of the solid part of the target (the mass absorption coefficient μ is constant in time). (5) The amplitudes of growing imprinted features are large enough that the propagation of a nonuniform shock contributes little to the total optical depth of the target.^{4} Given these assumptions, Eq. (1) becomes

$$I_2(\mathbf{r},t) \sim I_{\mathrm{env}}(\mathbf{r},t) \int d\mathbf{r}' R_{1,2}(\mathbf{r}-\mathbf{r}') \exp\left[-D_{\xi 0}(\mathbf{r}',t)\right], \tag{5}$$

where the modulation in a target optical depth $D_{\xi 0}(\mathbf{r},t)$ is simply

$$D_{\xi 0}(\mathbf{r},t) = \frac{\xi(\mathbf{r},t)}{\lambda_{\mathrm{CH}}}, \tag{6}$$

and the spectrally weighed attenuation length of the target λ_{CH} is given as

$$\lambda_{\mathrm{CH}} \simeq 1 \big/ \left[\mu_{\mathrm{CH}}(1.3\ \mathrm{keV})\, \rho_{\mathrm{abl}}\right]. \tag{7}$$

$I_{\mathrm{env}}(\mathbf{r},t)$ is the slowly varying envelope of the backlighter.

At this point, the target optical depth can be obtained from the measured optical depth by rigorously working backward through each stage, compensating for noise and system response (PSF) at each stage. However, if the modulation in the target optical density $D_{\xi 0}(\mathbf{r},t)$ is small,

$$D_{\xi 0}(\mathbf{r},t) << 1 \tag{8}$$

(which is the case in all our experiments), the entire imaging system may be considered linear. This greatly simplifies the relation between the measured optical depth and the target optical depth. We introduce a new variable, the optical depth modulation in the output of the framing camera $D_{\xi 2}(\mathbf{r},t)$, through the following equation:

$$I_2(\mathbf{r},t) \sim I_{\mathrm{env}}(\mathbf{r},t) \exp\left[-D_{\xi 2}(\mathbf{r},t)\right]. \tag{9}$$

Next, assuming that $D_{\xi 0}(\mathbf{r},t)$ and $D_{\xi 2}(\mathbf{r},t)$ are small, we expand in Taylor series the exponential functions in Eqs. (5) and (9) and retain only zeroth and first orders in these expansions. We then have

$$D_{\xi 2}(\mathbf{r},t) \cong \int d\mathbf{r}' R_{1,2}(\mathbf{r}-\mathbf{r}',t) D_{\xi 0}(\mathbf{r}',t). \tag{10}$$

Here we used the fact that the point spread function $R_{1,2}(\mathbf{r},t)$ is normalized $\int d\mathbf{r}\, R_{1,2}(\mathbf{r},t) = 1$. The T-MAX 3200 film has a constant MTF up to a spatial frequency ~50 mm^{-1}, the highest spatial frequency considered in our measurements, so the PSF of the film is set to be a $\delta(\mathbf{r})$ function. Since we use only the "linear" part of the $D \log(H)$ curve, the modulations in measured optical depth $D_{\xi 5}(\mathbf{r},t)$ are linearly related to the optical depth modulation in the target $D_{\xi 0}(\mathbf{r},t)$:

$$D_{\xi 5}(\mathbf{r},t) = \int d\mathbf{r}' R_{\mathrm{sys}}(\mathbf{r}-\mathbf{r}') D_{\xi 0}(\mathbf{r}',t), \tag{11}$$

where $R_{\mathrm{sys}}(\mathbf{r})$ is the PSF of the entire system. It is the convolution of PSF's of the pinhole, the framing camera, and the digitizing aperture of the densitometer. In frequency space, the system MTF is the product of the MTF's of each of these components.

In summary, we have used approximations of the system performance to find a straightforward relationship between the measured optical depth and the modulation of the ablation surface. As opposed to requiring detailed computer simulations to interpret experimental results, we find, for a class of experiments, a direct relationship between the measurement and target perturbations. Equation (11) has been derived by assuming that modulations of the target optical depth are small compared to unity. Since Eq. (11) is a linear approximation, it does not treat the generation of harmonics and coupling of modes produced by system nonlinearities. We have simulated these nonlinearities for modulation amplitudes greater than those measured routinely in our experiments and found that nonlinear effects were negligible compared to system noise.

System Sensitivity

Once the modulation in target optical depth is obtained (see above), the perturbation amplitude in the target can be found, provided various criteria are met. Variations in optical depth are produced by changes in either the target density or target thickness. Apparent changes in optical depth can also result from changes in the x-ray spectrum or in the attenuation coefficient of the target material. We performed several experiments to characterize the system performance.

System sensitivity is defined by the spectrally weighted x-ray attenuation length λ_{CH}. This length is inversely proportional to the mass absorption coefficient and the target density [see Eq. (7)]. In practice, λ_{CH} can be constructed using the target compression C_p, calculated by the 1-D hydrocode *LILAC*,[9] and the attenuation length of the undriven target λ_x:

$$\lambda_{\mathrm{CH}} = \frac{\lambda_x}{C_p}. \qquad (12)$$

This relation can be used as long as the driven target maintains a cold value of its mass absorption coefficient. Typically, during our experiments the target temperature is far below the values that could change the mass absorption coefficient.

We measured the attenuation length λ_x in undriven 25-μm CH_2 ($\rho = 0.92$ g/cm^3) targets using backlighter beams only. At the position of the experimental target, a thin strip of CH_2 was mounted so that the radiographic system could view x rays that both miss and traverse the target, as shown on the image taken at some time during the 3-ns backlighter pulse [see Fig. 76.37(a)]. The calculated attenuation length for this material was 11.5 μm, and we measured 10 μm±1 μm from the difference in optical depth in these two regions [lines A and B in Fig. 76.37(b)]. This value was constant for the ~1-mm backlighter spot and did not vary over the duration of the 3-ns backlighter pulse. We also radiographed undriven 20-μm CH ($\rho = 1.05$ g/cm^3) targets that had preimposed, low-amplitude (0.5 μm) sinusoidal modulations with wavelengths of 60 and 30 μm. Using these modulations as control references, λ_x was measured to be 10 μm±2 μm. These experiments showed that both backlighter spectrum and filter transmission remained constant in time during the measurements.

System Resolution

The resolution of the system was characterized by measuring its response to a sharp, opaque edge (machined platinum). Its image is shown in Fig. 76.38(a). The dashed line in Fig. 76.38(b) represents the light intensity incident on the edge, the thin solid line is the measured light intensity propagated through the system (and averaged in the direction parallel to the edge), and the thick solid line is the fit to experimental data assuming the system MTF as a two-Gaussian function:[10]

$$M_{\mathrm{sys}}(f) = 0.955\,\exp\left\{-\left[14.2(\mu\mathrm{m})f\right]^2\right\} + 0.045\,\exp\left\{-\left[248.3(\mu\mathrm{m})f\right]^2\right\}. \qquad (13)$$

The MTF is essentially the product of the responses of three system components: the pinhole camera, the 20-μm digitizing aperture, and the framing camera. The former two are straightforward calculations based on geometry and spectral energy. The MTF of the framing camera was determined by measuring the camera response to a 150-μm-wide slit (placed 1 mm in front of the camera) backlit by x rays [see Fig. 76.39(a)]. This image of the slit was digitized with a 5-μm scanning aperture. The slit width and its proximity to a camera were sufficient to neglect any diffraction effects. The dashed line in Fig. 76.39(b) represents the light intensity incident on the slit. The thin solid

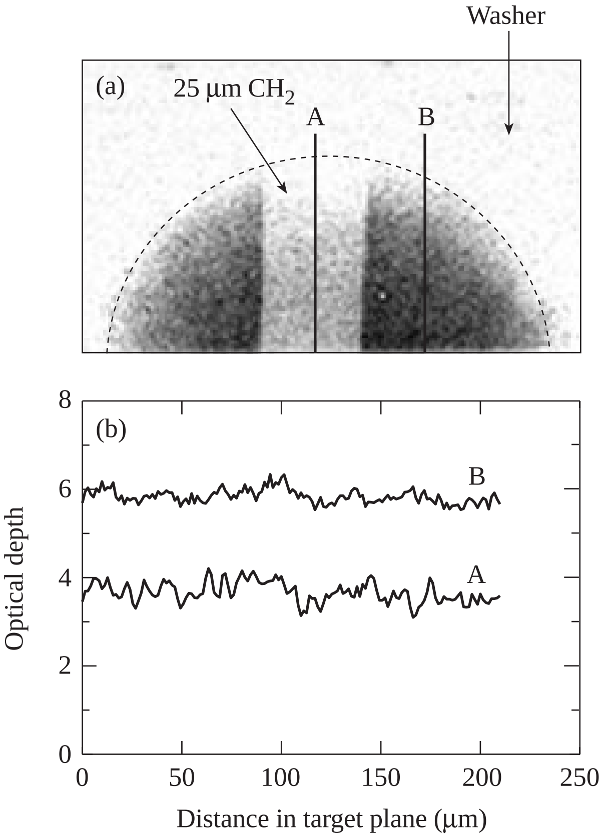

Figure 76.37
(a) Image of the undriven strip target; (b) lineouts of the measured optical depth (shown by lines A and B). Images through both the CH and open areas allow the optical depth to be measured.

line is the measured light intensity propagated through the system (and averaged in the direction parallel to the slit), and the thick solid line is the fit to experimental data assuming the framing camera MTF as a two-Gaussian function:

$$M_2(f) = 1.05\ \exp\left\{-\left[103.8(\mu\mathrm{m})f\right]^2\right\} - 0.05\ \exp\left\{-\left[95.8(\mu\mathrm{m})f\right]^2\right\}. \qquad (14)$$

The measured MTF of the framing camera is shown in Fig. 76.40. This MTF is similar to that measured in other experiments performed at LLNL[11,12] and NRL[13] with aluminized phosphor plates, which have reduced the long-scale-length scattering of photons and electrons between the phosphor and microchannel plates. This scattering resulted in a reduction of the MCP resolution up to about 20% at low spatial frequencies < 5 mm^{-1}. In our experiments, the phosphor plate was not aluminized. We saw, however, no significant reduction of the MTF at low spatial frequencies due to such scattering because of much lower levels of irradiation, compared with above-mentioned experiments.

Figure 76.41 shows the various MTF's discussed above. The thin solid line is the MTF of the entire system as determined by its edge response. The dotted line is the system MTF calculated as the product of the MTF's of the 8-μm pinhole (dot–dashed line), the framing camera (dashed line), and the 20-μm digitizing aperture (thick solid line). These MTF's assumed a system magnification of ~14. It can be seen that for

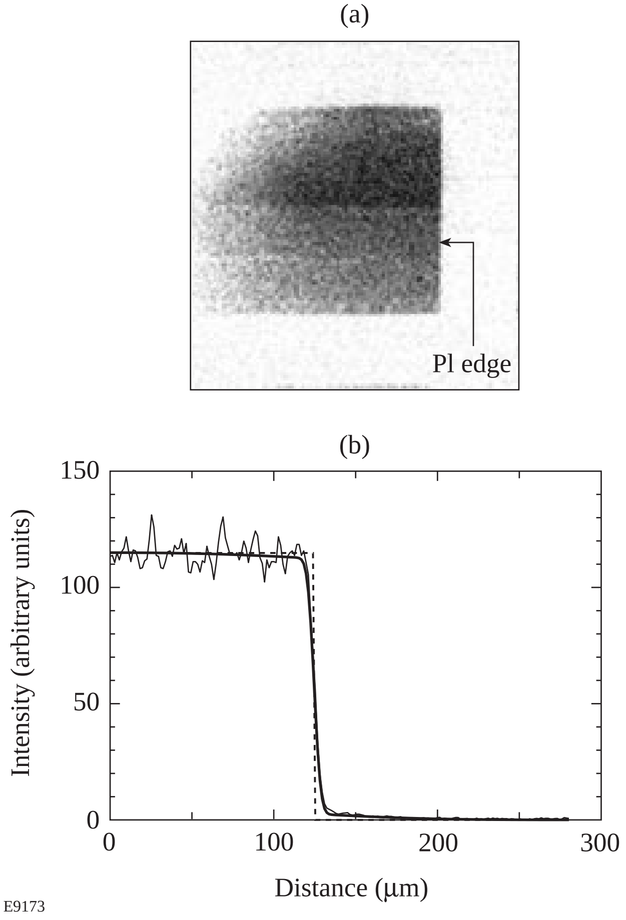

Figure 76.38
(a) Image of the edge target (Pt strip). (b) The dashed line represents the light intensity incident on the edge. The thin solid line is the measured light intensity propagated through the system (and averaged in the direction parallel to the edge), and the thick solid line is the fit to experimental data, assuming the system MTF to be a two-Gaussian function.

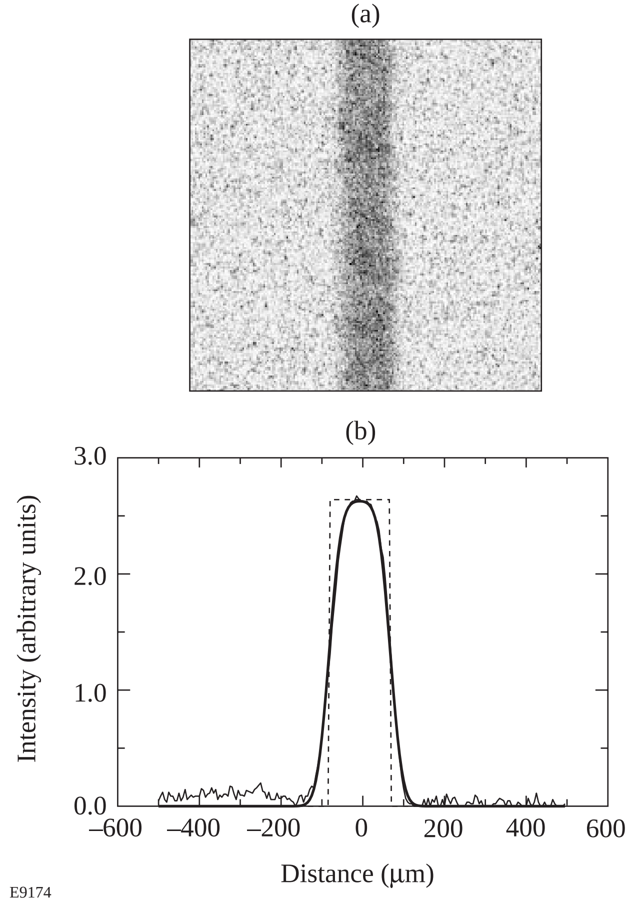

Figure 76.39
(a) Image of the slit target, installed in front of the MCP. (b) The dashed line represents the light intensity incident on the slit, the thin solid line is the measured light intensity propagated through the system (and averaged in the direction parallel to the slit), and the thick solid line is the fit to experimental data, assuming the framing-camera MTF to be a two-Gaussian function.

spatial frequencies below 70 mm^{-1}, the measured system MTF is in reasonable agreement with the aggregate response of the individual components. So in the analysis of target nonuniformity evolution (discussed in the **Wiener Filtering** section), we analyzed the signal only at frequencies below 70 mm^{-1}.

System Noise

Using radiographs of strip targets [see Fig. 76.37(a)], the system noise was characterized. Since the strip targets were uniform with very smooth surfaces, all nonuniformity measured in the radiographs of these targets is noise. The primary noise sources in this system are photon statistical noise of backlighter x rays, noise in the microchannel (MCP) and phosphor plates, film noise, and noise produced during digitization. It is possible to determine the origin of noise based on its spectrum since, in frequency space, the signal and noise at each stage are multiplied by the MTF of that portion of the system.

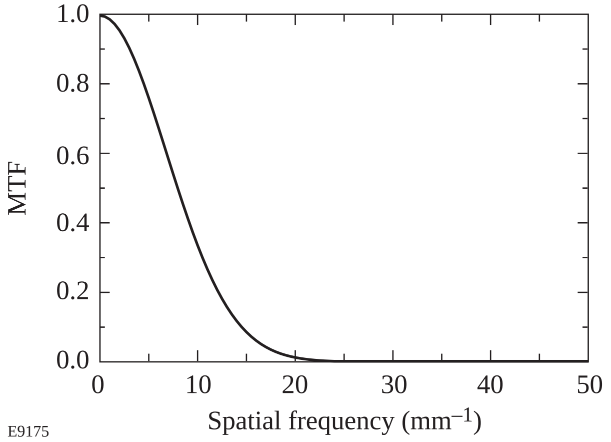

Figure 76.40
Resolution of the framing camera.

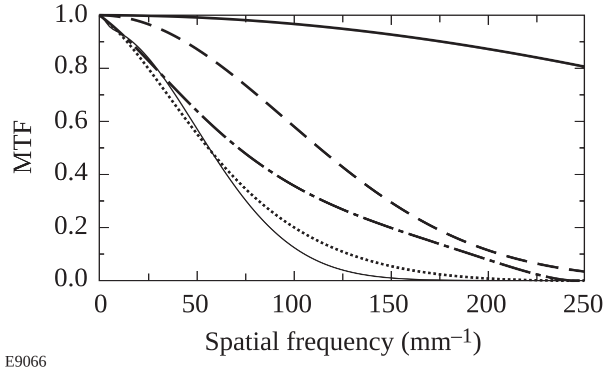

Figure 76.41
Resolution of the system. The thin solid line is the measured MTF of the entire system. The dotted line is the system MTF calculated as the product of the MTF's of the 8-μm pinhole (dot–dashed line), the framing camera (dashed line), and the 20-μm digitizing aperture (thick solid line).

Figure 76.42 depicts the azimuthally averaged Fourier amplitudes of the optical depth for two square regions with 150-μm width, through and around the strip. At high frequencies (>100 mm^{-1}), the averaged noise is nearly constant, indicative of the noise from film and digitization. At lower spatial frequencies the noise amplitude depends on the MTF's of the pinhole camera and MCP. This suggests that the dominant noise source is the photon statistics of the backlighter x rays. In optical-depth space, the noise amplitude is inversely proportional to the square root of the number of photons. There is more noise in the region of the strip with few x-ray photons than in the region out of the strip.

This relationship between noise levels and the photon flux can be explained by the following consideration: If I_1 and I_2 are the average x-ray intensities in and out of the strip regions, respectively, then noise rms amplitudes in these regions are ~ $\sqrt{I_1}$ and $\sqrt{I_2}$, assuming a monochromatic x-ray spectrum. Since the signal's optical depth is the natural logarithm of its intensity, the variation of a signal from its averaged value in terms of the optical depth will be proportional to $1/\sqrt{I_1}$ and $1/\sqrt{I_2}$ after a series expansion of the logarithm, retaining only the first term. It is assumed that the number of x-ray photons per pixel is greater than 1, which is necessary to justify such an analysis. The fact that there is more noise in the optical depth in the attenuated strip region with fewer x-ray photons (rms

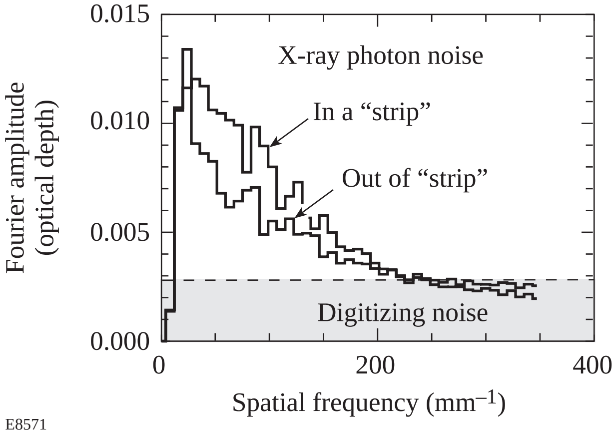

Figure 76.42
System noise. The measured noise level for two portions of a radiograph through and around the 25-μm-CH_2 strip target.

amplitude $\sim 1/\sqrt{I_1}$) than in the region out of the strip (rms amplitude $\sim 1/\sqrt{I_2}$) supports the suggestion of the photon-statistical nature of the noise.

Wiener Filtering

Using the measured system sensitivity, resolution, and noise, we recovered the imprinted perturbations from the radiographic images. A broad spectrum of imprinted features has been generated by laser nonuniformities with spatial frequencies up to 430 mm^{-1}. These initial imprinted nonuniformities in our experiments come from the nonuniformities in drive-laser beams used with distributed phase plates (DPP's).[14] The RT instability has growth rates and saturation effects that depend upon spatial frequency. In addition, the resolution of the radiographic system begins to cut off spatial frequencies above ~70 mm^{-1}. As a result, the detected signal resides in a narrow range of spatial frequencies ~10 to 70 mm^{-1}.

We analyzed 400-μm-square sections of the radiographic images of the target by converting them to measured optical depth, compensating for the backlighter envelope using a fourth-order, two-dimensional polynomial fit. The signal nonuniformity is expressed as the power per mode in optical depth by Fourier transforming the resulting optical depth.

A Wiener filter was developed to recover the true signal from the resulting images.[15] If $C(\mathbf{f})$ is the signal plus noise measured by the system, $C(\mathbf{f}) = S(\mathbf{f}) + N(\mathbf{f})$, then the restored signal $P(\mathbf{f})$ is

$$P(\mathbf{f}) = \frac{C(\mathbf{f})}{M_{\text{sys}}} \frac{|S(\mathbf{f})|^2}{|S(\mathbf{f})|^2 + |N_{\text{avg}}(\mathbf{f})|^2}, \qquad (15)$$

where M_{sys} is total system MTF, $|N_{\text{avg}}(\mathbf{f})|^2$ is the average or Wiener noise spectrum, and $|S(\mathbf{f})|^2$ is the measured signal power spectrum. The average noise spectrum $|N_{\text{avg}}(\mathbf{f})|^2$ and system MTF have been measured as described above; the only unknown is $|S(\mathbf{f})|^2$, the measured signal power spectrum. In this technique, the signal is compared to the measured noise spectrum, and only points that are greater than twice the amplitude of that noise are considered first, i.e.,

$$|S(\mathbf{f})|^2 = |C(\mathbf{f})|^2 - |N_{\text{avg}}(\mathbf{f})|^2,$$

for (16)

$$|C_{\text{re}}(\mathbf{f})| \text{ or } |C_{\text{im}}(\mathbf{f})| > 2|N_{\text{avg}}(\mathbf{f})|,$$

where $|C_{\text{re}}(\mathbf{f})|$ and $|C_{\text{im}}(\mathbf{f})|$ are real and imaginary parts of the measured signal with noise. Due to the statistical nature of the noise spectrum, the signal that is less than twice the noise amplitude can be treated in three primary manners: (a) rejected (i.e., set to 0), (b) considered to be uniformly distributed between zero and twice the noise level, or (c) set equal to twice the noise level. These options are used to provide the uncertainties of the measured signal. At higher spatial frequencies (>70 mm^{-1}) the detector response is falling rapidly, so the signal-to-noise level is greatly reduced and the error bars are larger.

The thin solid line in Fig. 76.43(a) shows the power per mode of the noise. The thick solid line represents the power per mode of the image at ~2 ns. These two lines are almost the same at high spatial frequencies > 80 mm^{-1}, suggesting that the

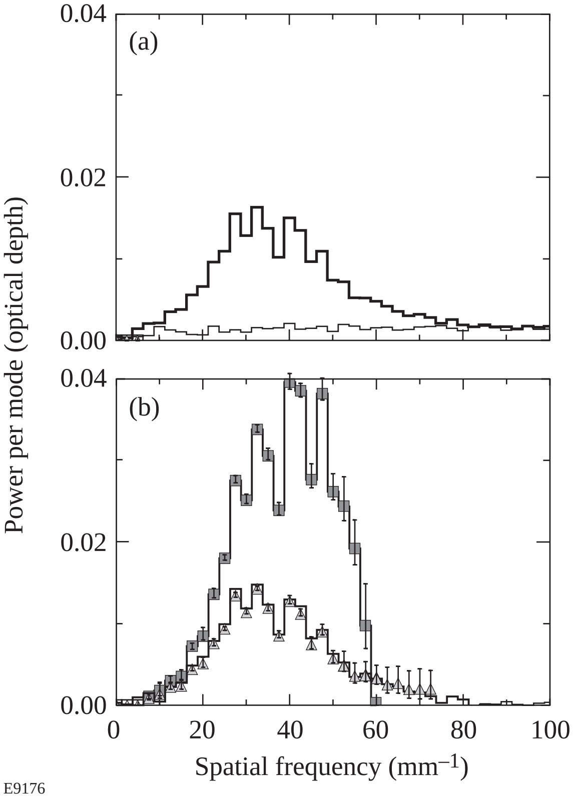

Figure 76.43
(a) Power per mode of the noise (thin solid line) and power per mode of the signal plus noise of the driven foil image at 2 ns. (b) Power per mode of target modulations versus spatial frequency. This is calculated using a Wiener filter, assuming MTF = 1 (triangles), calculated by subtracting the noise power per mode from the power per mode of the signal plus noise (lower solid line that agrees with triangles), and calculated using a Wiener filter, assuming a measured MTF (squares).

noise dominates at these spatial frequencies in the 2-ns image. There is a significant level of signal at lower spatial frequencies, however, which must be separated from noise.

The result of the Wiener filter[15] is shown in Fig. 76.43(b). To demonstrate the effect of noise reduction, we set the MTF = 1 (i.e., no resolution compensation) in Eq. (15); this is shown as the triangles in Fig. 76.43(b). The lower solid line shows the data obtained by simply subtracting the noise power per mode [the thin solid line in Fig. 76.43(a)] from the measured power per mode of signal plus noise [the thick solid line in Fig. 76.43(a)]. The agreement between these curves indicates that the noise compensation portion of the Wiener filter behaves reasonably. The upper curve in Fig. 76.43(b) depicts the result using the proper MTF and represents the fully processed data used as our experimental results.

Conclusions

By properly characterizing our detection system, we have simplified the complex relation between radiographic images and the optical depth in the target. Using measured aspects of the system, we have generated linear approximations of the system response that apply to our conditions. We measured the sensitivity and the resolution and demonstrated that they remain constant for the duration of the experiment. Using measured noise spectra, we have constructed a Wiener filter that enables us to distinguish the signal from noise and to reconstruct that signal by deconvolving system MTF. This technique is routinely applied to the analysis of our experiments.

ACKNOWLEDGMENT

This work was supported by the U.S. Department of Energy Office of Inertial Confinement Fusion under Cooperative Agreement No. DE-FC03-92SF19460, the University of Rochester, and the New York State Energy Research and Development Authority. The support of DOE does not constitute an endorsement by DOE of the views expressed in this article.

REFERENCES

1. D. K. Bradley, J. A. Delettrez, R. Epstein, R. P. J. Town, C. P. Verdon, B. Yaakobi, S. Regan, F. J. Marshall, T. R. Boehly, J. P. Knauer, D. D. Meyerhofer, V. A. Smalyuk, W. Seka, D. A. Haynes, Jr., M. Gunderson, G. Junkel, C. F. Hooper, Jr., P. M. Bell, T. J. Ognibene, and R. A. Lerche, Phys. Plasmas **5**, 1870 (1998).
2. S. G. Glendinning *et al.*, in *Applications of Laser Plasma Radiation II*, edited by M. C. Richardson and G. A. Kyrala (SPIE, Bellingham, WA, 1995), Vol. 2523, pp. 29–39.
3. T. R. Boehly, V. A. Smalyuk, D. D. Meyerhofer, J. P. Knauer, D. K. Bradley, C. P. Verdon, and D. Kalantar, in *Laser Interaction and Related Plasma Phenomena*, edited by G. H. Miley and E. M. Campbell (American Institute of Physics, New York, 1997), Vol. 406, pp. 122–129.
4. J. P. Knauer, C. P. Verdon, D. D. Meyerhofer, T. R. Boehly, D. K. Bradley, V. A. Smalyuk, D. Ofer, P. W. McKenty, S. G. Glendinning, D. H. Kalantar, R. G. Watt, P. L. Gobby, O. Willi, and R. J. Taylor, in *Laser Interaction and Related Plasma Phenomena*, edited by G. H. Miley and E. M. Campbell (American Institute of Physics, New York, 1997), Vol. 406, pp. 284–293.
5. T. Endo *et al*., Phys. Rev. Lett. **74**, 3608 (1995).
6. R. Ishizaki and K. Nishihara, Phys. Rev. Lett. **78**, 1920 (1997).
7. D. H. Kalantar, M. H. Key, L. B. Da Silva, S. G. Glendinning, B. A. Remington, J. E. Rothenberg, F. Weber, S. V. Weber, E. Wolfrum, N. S. Kim, D. Neely, J. Zhang, J. S. Wark, A. Demir, J. Lin, R. Smith, G. J. Tallents, C. L. S. Lewis, A. MacPhee, J. Warwick, and J. P. Knauer, Phys. Plasmas **4**, 1985 (1997).
8. B. A. Remington *et al.*, Phys. Fluids B **4**, 967 (1992).
9. An earlier version of *LILAC* is described in E. Goldman, Laboratory for Laser Energetics Report No. 16, University of Rochester (1973).
10. B. A. Remington *et al*., Rev. Sci. Instrum. **63**, 5080 (1992).
11. J. D. Wiedwald *et al*., in *Ultrahigh- and High-Speed Photography, Videography, Photonics, and Velocimetry '90*, edited by L. L. Shaw, P. A. Jaanimagi, and B. T. Neyer (SPIE, Bellingham, WA, 1990), Vol. 1346, pp. 449–455.
12. H. F. Robey, K. S. Budil, and B. A. Remington, Rev. Sci. Instrum. **68**, 792 (1997).
13. C. J. Pawley, A. V. Deniz, and T. Lehecka "Noise and Sensitivity in X-Ray Framing Cameras," to be published in the Review of Scientific Instruments.
14. Y. Lin, T. J. Kessler, and G. N. Lawrence, Opt. Lett. **20**, 764 (1995).
15. L. R. Rabiner and B. Gold, *Theory and Application of Digital Signal Processing* (Prentice-Hall, Englewood Cliffs, NJ, 1975).

Collisionless Damping of Localized Plasma Waves in Laser-Produced Plasmas and Application to Stimulated Raman Scattering in Filaments

Stimulated Raman scattering (SRS), an instability that converts laser light incident on a plasma into plasma waves and lower-frequency scattered photons, has been a major concern in laser fusion research for many years. The scattered photons represent wasted energy, and the plasma waves can produce suprathermal electrons that penetrate and preheat the target core, thereby preventing efficient implosion. Interest in SRS has intensified in recent years as experiments with higher laser intensities and longer-scale-length plasmas, intended to simulate laser–plasma interaction conditions in the National Ignition Facility (NIF), have yielded SRS reflectivities as high as 25%.[1] Furthermore, for many years theoretical models of SRS have had difficulty accounting for several aspects of the experimental observations: SRS is often observed at incident intensities well below the theoretical threshold; the spectrum of the scattered light is broader and extends to shorter wavelengths than theory predicts; and anomalous spectral and temporal structure is observed.[2] More recently it has been found that "beam smoothing," which involves small increases in the spatial and/or temporal bandwidth of the incident laser light, effectively suppresses the SRS instability,[3,4] while theory predicts that much larger increases in the bandwidth, comparable to the instability growth rate, would be required for such suppression.

To account for the discrepancies in the threshold and spectrum, it was proposed some time ago[5,6] that SRS is not occurring in the bulk plasma, but rather in intense light filaments formed from hot spots in the incident laser beam by the self-focusing instability. Intensities in such filaments could easily surpass SRS thresholds, even if the average beam intensity was well below the threshold, and the higher intensity would be expected to drive SRS over a broader range of wavelengths. The more recent experimental observations add further support to this hypothesis: Filamentation can be suppressed by much lower bandwidths than would be required to suppress SRS directly, and the anomalous spectral and temporal features may be accounted for by the temporal evolution of the waveguide mode structure in the filament. A thorough discussion of the anomalies in SRS experiments and how they can be explained by filamentation is presented in Afshar-rad *et al.*,[7] along with direct observational evidence for the occurrence of SRS in filaments. It should be pointed out that this interpretation of the experimental observations has great potential significance for NIF since it suggests that the bandwidth already incorporated in the NIF design to improve irradiation uniformity may also be sufficient to suppress or greatly reduce SRS.

The experimental evidence for the connection between filamentation and SRS is especially compelling for the short-wavelength portion of the SRS spectrum. Recently reported experiments[1,3,4] on the Nova laser at LLNL studied a 351-nm laser beam interacting with a preformed plasma at a temperature of ~3 keV. The density profiles of these plasmas have a large central region at densities of about 10% n_{crit} and fairly sharp boundaries. LASNEX simulations of these targets, in concert with the laser interactions postprocessor (LIP),[8] predicted a narrow SRS spectrum at ~600 nm, whereas observations showed a much broader spectrum extending to shorter wavelengths. In some cases without beam smoothing, this part of the spectrum dominated, with a peak near 450 nm. Substantial scattering at these wavelengths requires long regions of very-low-density plasma, which do not appear in the hydrodynamic simulations but could exist in a filament. This part of the spectrum is strongly peaked in the backscatter direction and is greatly diminished by increased bandwidth:[4] further indications that this scattering is associated with filamentation. The beam-deflection phenomenon, observed in many of these experiments and associated with filamentation in theory and simulations,[9,10] provides independent evidence that filamentation is occurring in these plasmas.

One remaining difficulty with this interpretation concerns the damping of SRS at these wavelengths. The parametric nature of the SRS instability requires that the participating electromagnetic and electrostatic waves satisfy frequency- and wave-vector–matching conditions:

$$\omega_0 = \omega + \omega_s , \quad k_0 = k + k_s ,$$

where (ω_0,k_0), (ω_s,k_s), and (ω,k) are the frequency and wavenumber pairs of the incident and scattered electromagnetic waves and the plasma wave, respectively. In the fluid approximation the dispersion relations for these three waves are

$$\begin{aligned}\omega_0^2 &= \omega_p^2 + c^2k_0^2,\\ \omega_s^2 &= \omega_p^2 + c^2k_s^2,\\ \omega^2 &= \omega_p^2 + 3v_T^2k^2 = \omega_p^2\left(1+3k^2\lambda_{\mathrm{D}}^2\right),\end{aligned}$$

where ω_p is the plasma frequency, v_T is the electron thermal velocity, and λ_{D} is the Debye length. Short-wavelength scattering requires that ω and therefore ω_p be small so that $\omega_s \approx \omega_0$. Consequently, the thermal dispersion term becomes significant, with $k\lambda_{\mathrm{D}}$ of order 1. It is well known that for electrostatic waves in homogeneous plasmas Landau damping becomes very strong when $k\lambda_{\mathrm{D}} \geq 0.4$. This suggests that the plasma wave associated with short-wavelength SRS will be heavily Landau damped, and, in fact, in this case SRS is more properly referred to as stimulated Compton scattering (SCS), which has a much lower growth rate and correspondingly higher threshold; thus, significant scattering would not be expected in this range of wavelengths. One possible explanation, recently proposed by Afeyan *et al.*,[11] is that thermal transport across steep temperature gradients, produced by inverse bremsstrahlung absorption in intense hot spots in the laser beam, produces a modified non-Maxwellian electron distribution function (MDF) in the hot spot with a depleted high-energy tail. Since the high-energy electrons are responsible for Landau damping, this would result in a reduced damping in the hot spots, allowing SRS to occur. The thermal-electron mean free path in these plasmas, however, is typically much larger than the size of the laser hot spots, and the mean free path for the high-energy electrons is even longer, so it is not clear that the required steep gradient in the high-energy electron population could be sustained. Moreover, recent experiments[12] using random phase plates suggest that hot spots alone, without self-focusing, cannot account for the levels of SRS observed.

In this article we propose an alternative explanation. We investigate the collisionless damping of plasma waves propagating in a bounded region of plasma, such as the interior of a filament, and find that it can be much smaller than expected on the basis of the infinite-medium Landau theory, even with a Maxwellian electron distribution. Using a simple model of a filament and its internal modes, we then apply these results to SRS in filaments.

Linear Collisionless Damping of Localized Plasma Waves

SRS occurs when plasma waves originating in noise are amplified by their interaction with the laser field. The initiation and early growth of the instability thus depend on the behavior of small-amplitude plasma waves, so for the purpose of analyzing SRS thresholds and growth rates, a linear treatment of the plasma waves suffices. Furthermore, in the plasmas of interest here, the mean free paths and collision times are much longer than the spatial and temporal scales of interest, so the plasma may be regarded as collisionless. We will therefore be interested in the collisionless damping of localized small-amplitude plasma waves. This process is often referred to as "transit-time damping" since it results from the transfer of energy from the wave to particles transiting the localization volume. Although the analysis presented here is self-contained, we treat transit-time damping in filaments using the method presented in greater generality in an earlier article.[13]

Since we are interested in filaments, we will analyze plasma waves confined in a cylindrical geometry (though the extension to other geometries will be evident and the case of slab geometry is treated in Appendix A). For simplicity, we consider only azimuthally symmetric waveguide modes ($\ell = 0$) for the electromagnetic and electrostatic waves in the cylinder. While self-consistent radial intensity and density profiles for filaments can be calculated numerically,[6] it is adequate for our purposes to consider a simple filament model consisting of a circular cylinder with a sharp boundary at radius R, as shown in Fig. 76.44. The density n_0 inside the filament is assumed to be significantly lower than that outside the filament, so that waveguide modes for the light and plasma waves have negligible fields extending outside the cylinder. Pressure balance is provided by the ponderomotive potential Ψ_0 of the laser light propagating in the filament. The size and intensity of filaments likely to form in laser-produced plasmas and the properties of the corresponding waveguide modes will be discussed further below.

Inside the filament the electron distribution function is

$$f_0(\mathbf{r},\mathbf{v}) = \frac{n_0}{(2\pi)^{3/2}v_T^3}\,e^{-v^2/2v_T^2},$$

where $v_T^2 = k_BT_0/m$. Consider a phase-space volume element dV containing a group of co-moving particles passing through the filament. We represent the motion of each particle by the motion of its oscillation center, neglecting the oscillation amplitude of the particle in the laser field as small compared to the length scales over which the fields vary. Since we are taking the equilibrium ponderomotive potential inside the filament to be uniform, the particle trajectories can then be represented as straight lines within the filament, as shown in Fig. 76.44. Each particle thus acquires an energy ΔE in time $\Delta t = 2\sqrt{R^2 - b^2}\big/v_\perp$, where b is the impact parameter of the particle and $v_\perp$ is the velocity component perpendicular to the cylinder axis. This energy, which may be positive or negative, is acquired as the particle interacts with the plasma wave trapped in the filament. To conceptually simplify the analysis we take this wave to be a standing wave and we assume that the energy removed from the wave by damping is replaced by a driving process, such as SRS, so that the wave has a constant amplitude. Then, since f_0 is even in $\mathbf{v}$, it is clear that the time-reversed process, in which the particles in a time-reversed phase-space element dV^* interact with the filament, acquiring energy $-\Delta E$ in time Δt, is also occurring. Since we are neglecting collisions, phase-space volume is conserved, $|dV^*| = |dV|$, and the net rate at which energy is transferred to the particles associated with dV is

$$\Delta P = \Delta E\left[f_0(E)\,dV - f_0(E+\Delta E)\,dV^*\right]\big/\Delta t$$

$$\cong -\frac{(\Delta E)^2}{\Delta t}\frac{\partial f_0}{\partial E}\,dV\,.$$

Integration of this quantity over the phase space within the filament then gives *twice* the collisionless damping rate of the plasma wave since the phase space is effectively included twice in the integration (both forward and backward in time).

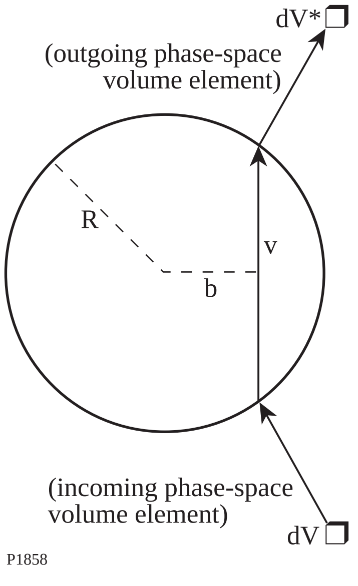

Figure 76.44
Geometry of cylindrical filament model. *R* is the cylinder radius, *v* and *b* are the electron velocity and impact parameter, respectively, and *dV* denotes a six-dimensional phase-space volume element.

First we calculate the energy acquired by a particle interacting with the filament. Inside the filament the potential satisfies the longitudinal plasma-wave dispersion relation, so assuming azimuthal symmetry for simplicity, we can write the potential as

$$\phi(r,z,t) = AJ_0(kr)\,\cos\left(k_z z + \alpha\right)\cos\left(\omega t + \beta\right), \qquad (1)$$

where A is the infinitesimal wave amplitude, J_0 is the zeroth-order Bessel function, k_z and ω are the axial wave number and frequency of the wave, and α and β are arbitrary constants representing the spatial and temporal phases of the wave, to be averaged over below. The boundary condition is $J_0(kR) = 0$, so k may be any of a discrete set of wave numbers determined by the roots of the Bessel function. We relate ω and k by the fluid plasma dispersion relation

$$\omega^2 = \omega_p^2 + 3\left(k_z^2 + k^2\right)v_T^2\,.$$

The main kinetic correction to this relation is an imaginary component of ω resulting from the damping we are about to calculate; corrections to the real frequency will result only in a small shift in the resulting SRS spectrum and will be neglected here. Let $t = 0$ be the time when the particle is closest to the cylinder axis. Its change in energy in crossing the filament is then obtained by integrating over the unperturbed orbit:

$$\Delta E = -e\int_{-t_0}^{t_0}\mathbf{v}\cdot\nabla\phi(\mathbf{r},t)\,dt\,,$$

where $t_0 = \sqrt{R^2 - b^2}\big/v_\perp$. The total derivative of the potential is

$$\frac{d}{dt}\phi\left[\mathbf{r}(t),t\right] = \mathbf{v}\cdot\nabla\phi\left[\mathbf{r}(t),t\right] + \frac{\partial}{\partial t}\phi\left[\mathbf{r}(t),t\right],$$

so the above integral can be written

$$\Delta E = -e\int_{-t_0}^{t_0}\left\{\frac{d}{dt}\phi\left[\mathbf{r}(t),t\right] - \frac{\partial}{\partial t}\phi\left[\mathbf{r}(t),t\right]\right\}dt.$$

The potential seen by the particle is the same before and after passing through the filament, so

$$\int_{-t_0}^{t_0}\frac{d}{dt}\phi\left[\mathbf{r}(t),t\right]dt = 0$$

and

$$\Delta E = e\int_{-t_0}^{t_0}\frac{\partial}{\partial t}\,\phi\left[\mathbf{r}(t),t\right]dt.$$

Substituting the form of the potential, we have

$$\begin{aligned}\Delta E &= -e\,\omega A\int_{-t_0}^{t_0} J_0\left[kr(t)\right]\cos\left[k_z v_z t + \alpha\right]\sin(\omega t + \beta)dt\\ &= -e\,\omega A\left\{\cos\alpha\sin\beta\int_{-t_0}^{t_0} J_0\left[kr(t)\right]\cos k_z v_z t\cos\omega t\right.\\ &\qquad\left.-\sin\alpha\cos\beta\int_{-t_0}^{t_0} J_0\left[kr(t)\right]\sin k_z v_z t\sin\omega t dt\right\}.\end{aligned}$$

Squaring and averaging over the phases α and β gives

$$\begin{aligned}\left\langle\Delta E^2\right\rangle = \frac{\omega^2 e^2 A^2}{4}&\left\{\left[\int_{-t_0}^{t_0} J_0\left[kr(t)\right]\cos k_z v_z t\cos\omega t dt\right]^2\right.\\ &\left.+\left[\int_{-t_0}^{t_0} J_0\left[kr(t)\right]\sin k_z v_z t\sin\omega t dt\right]^2\right\}.\end{aligned}$$

Defining the integrals

$$I_\pm \equiv \int_{-t_0}^{t_0} J_0\left[kr(t)\right]\cos\left[(\omega \pm k_z v_z)t\right]dt,$$

we have

$$\left\langle\Delta E^2\right\rangle = \frac{\omega^2 e^2 A^2}{8}\left(I_+^2 + I_-^2\right) = \frac{\omega^2 e^2 A^2}{4}I_+^2,$$

where the last form follows from the symmetry: $f_0(v_z) = f_0(-v_z)$, so waves propagating in both directions along the axis must be equally damped. Changing the integration variable to $s = kv_\perp t$,

$$\begin{aligned}I_\pm &= \frac{1}{kv_\perp}\int_{-k\sqrt{R^2-b^2}}^{k\sqrt{R^2-b^2}} J_0\left[\sqrt{(kb)^2+s^2}\right]\\ &\qquad\times\cos\left[\frac{\omega \pm k_z v_z}{kv_\perp}s\right]ds\\ &= \frac{1}{kv_\perp}G\left(kR, kb, \frac{\omega \pm k_z v_z}{kv_\perp}\right),\end{aligned}$$

where we have defined the function

$$G(x,y,z) = \int_{-\sqrt{x^2-y^2}}^{\sqrt{x^2-y^2}} J_0\left(\sqrt{y^2+s^2}\right)\cos(zs)\,ds,$$

which must be evaluated numerically.

Next we must integrate the above expression for $\left\langle\Delta E^2\right\rangle$ over the six-dimensional phase space inside the cylinder. Note that it depends on the particle coordinates and velocities only through the two quantities kb and $w_\pm \equiv (\omega \pm k_z v_z)/kv_\perp$. The total power being transferred to particles in a length L of filament is

$$\begin{aligned}P = \int_0^L dz\int_{-\infty}^{\infty} dv_z\int_0^{\infty} dv_\perp v_\perp&\\ \times\int_0^R drr\int_0^{2\pi} d\theta_r\int_0^{2\pi} d\theta_v&\left[-\frac{1}{2}\frac{\left\langle\Delta E^2\right\rangle}{\Delta t}\frac{\partial f_0}{\partial E}\right],\end{aligned}\tag{2}$$

where the factor 1/2 in the integrand compensates for the double-counting of phase space, as noted above. Because of the rotational symmetry, all particle orbits with the same impact parameter b and speed $|v|$ must make the same contribution to $\left\langle\Delta E^2\right\rangle$, so the quantity in square brackets in (2) depends on r, θ_r, and θ_v only through the impact parameter b. We can therefore transform the last three integrals in the above expression to a single integral over b. First we transform the angles θ_r and θ_v to

$$\begin{aligned}\theta_+ &\equiv \theta_v + \theta_r,\\ \theta_- &\equiv \theta_v - \theta_r.\end{aligned}$$

By shifting portions of the region of angular integration by 2π in θ_r or θ_v, the integral over $[0, 2\pi]$ in θ_r and θ_v becomes an integral over $[0, 4\pi]$ in θ_+ and $[-\pi,\pi]$ in θ_-, as shown in

Fig. 76.45(a). Using the Jacobian $\partial\left(\theta_r,\theta_v\right)/\partial\left(\theta_+,\theta_-\right)=1/2$, we see that the angular integration is transformed as

$$\int_0^{2\pi} d\theta_r \int_0^{2\pi} d\theta_v \to \frac{1}{2}\int_0^{4\pi} d\theta_+ \int_{-\pi}^{\pi} d\theta_- .$$

Next we use

$$\theta_- = \sin^{-1}\frac{b}{r}, \qquad \frac{\partial\theta_-}{\partial b} = \frac{1}{\sqrt{r^2-b^2}}, \quad \text{for } 0 \le \theta_- \le \frac{\pi}{2}.$$

As shown in Fig. 76.45(b), there are four values of θ_- in $[-\pi,\ \pi]$ for each value of r and b. Because of the cylindrical symmetry these values of θ_- are all physically equivalent, so we can combine the above results to obtain the transformation

$$\int_0^{2\pi} d\theta_r \int_0^{2\pi} d\theta_v \int_0^R dr r$$

$$\to 4 \cdot \frac{1}{2}\int_0^{4\pi} d\theta_+ \int_0^R db \int_b^R dr r \frac{1}{\sqrt{r^2-b^2}}$$

$$\to 8\pi \int_0^R db \sqrt{R^2-b^2} .$$

After this transformation, the expression for the power is

$$P = 4\pi L \int_{-\infty}^{\infty} dv_z \int_0^{\infty} dv_\perp v_\perp \int_0^R db$$

$$\times \sqrt{R^2-b^2}\left[-\frac{\left\langle \Delta E^2 \right\rangle}{\Delta t}\frac{\partial f_0}{\partial E}\right], \qquad (3)$$

where we have done the z-integral using the fact that $\left\langle \Delta E^2 \right\rangle$ is independent of z.

Using

$$\frac{\partial f_0}{\partial E} = -\frac{n_0}{(2\pi)^{3/2} m v_T^5} e^{-v^2/2v_T^2}, \qquad \Delta t = \frac{2\sqrt{R^2-b^2}}{v_\perp},$$

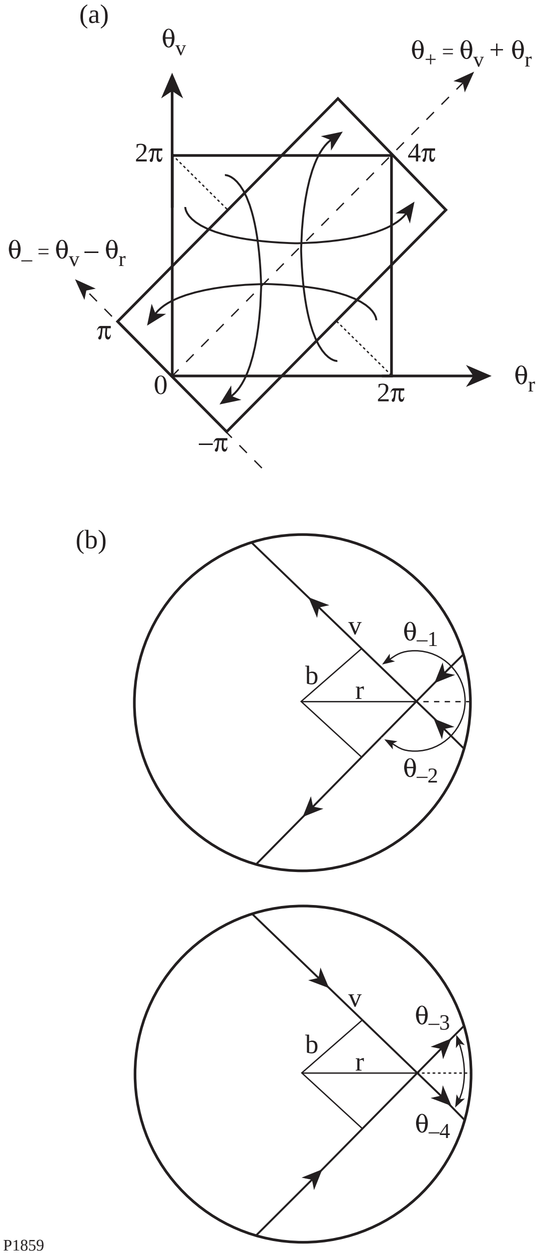

Figure 76.45
Illustration of variable and range transformations used in converting the integral in Eq. (2) to the form in Eq. (3). The angles θ_i in (b) are measured from the dashed extension of r.

and

$$\left\langle \Delta E^2 \right\rangle = \frac{\omega^2 e^2 A^2}{4k^2 v_\perp^2} G^2\left(kR, kb, \frac{\omega + k_z v_z}{k v_\perp}\right),$$

this becomes

$$P = \frac{n_0 \omega^2 e^2 A^2 L}{4(2\pi)^{1/2} m v_T^5 k^2}$$

$$\times \int_{-\infty}^{\infty} dv_z \int_0^{\infty} dv_\perp \int_0^R db G^2\left(kR, kb, \frac{\omega + k_z v_z}{k v_\perp}\right) e^{-v^2/2v_T^2} .$$

As an aside, we now verify that the above expression gives the familiar result for Landau damping of a plane electrostatic wave as $R \to \infty$. This result can be established in full generality (including finite radial and azimuthal wave numbers) by methods analogous to those employed for slab and spherical geometries in Ref. 14, but the analysis is fairly complex. Since we are interested here in the application to SRS backscatter, we can simplify matters by considering only the special case where the $R \to \infty$ limit is a plane wave with wave number k_z propagating in the z direction ($k = 0$). To simplify the calculation, we take the limit $k \to \infty$ first, and then let $R \to \infty$, so that the cylinder contains a plane wavefront for all $r < R$. This means the boundary conditions will not be satisfied as we take this limit, but this doesn't affect the result since the boundary's contribution to the damping vanishes as it recedes to infinity. For small x, y we have

$$G(x,y,z) \cong \int_{-\sqrt{x^2-y^2}}^{\sqrt{x^2-y^2}} \cos zs\, ds = \frac{2}{z} \sin\left(\sqrt{x^2 - y^2}\, z\right),$$

so

$$\lim_{k \to 0} \frac{1}{k^2} G^2\left(kR, kb, \frac{\omega + k_z v_z}{k v_\perp}\right)$$

$$= \frac{4 v_\perp^2}{\left(\omega + k_z v_z\right)^2} \sin^2\left[\frac{\sqrt{R^2 - b^2}}{v_\perp}\left(\omega + k_z v_z\right)\right].$$

Now the quantity $\sqrt{R^2 - b^2} / v_\perp$ in the argument of the sine function above is half the time a particle spends in the cylinder; it becomes large as R becomes large, except for the relatively small number of particles that just graze the boundary of the cylinder. Since the relative contribution of the boundary becomes insignificant as $R \to \infty$, we may regard $\sqrt{R^2 - b^2} / v_\perp$ as large for all particles of interest. With this assumption, and using

$$\lim_{\alpha \to \infty} \frac{\sin^2 \alpha x}{\alpha x^2} = \pi \delta(x) \text{ with } \alpha = \sqrt{R^2 - b^2} \;\; v_\perp ,$$

we have

$$\lim_{k \to 0} \frac{1}{k^2} G^2\left(kR, kb, \frac{\omega + k_z v_z}{k v_\perp}\right)$$

$$= \frac{4\pi\sqrt{R^2 - b^2}}{k_z} v_\perp \delta\left(v_z + \frac{\omega}{k_z}\right),$$

so that

$$P = \frac{4\pi n_0 \omega^2 e^2 A^2 L}{4(2\pi)^{1/2} m v_T^5 k_z}$$

$$\times \int_0^{\infty} dv_\perp v_\perp \int_0^R db \sqrt{R^2 - b^2}$$

$$\times \int_{-\infty}^{\infty} dv_z \delta\left(v_z + \frac{\omega}{k_z}\right) e^{-v^2/2v_T^2}$$

$$= \frac{\omega_p^2 \omega^2 A^2 L}{4(2\pi)^{1/2} v_T^5 k_z} e^{-\frac{\omega^2}{2k_z^2 v_T^2}}$$

$$\times \int_0^{\infty} dv_\perp v_\perp e^{-v_\perp^2/2v_T^2} \int_0^R db \sqrt{R^2 - b^2}$$

$$= \frac{\omega_p^2 \omega^2 A^2 L}{4(2\pi)^{1/2} v_T^3 k_z} \frac{\pi R^2}{4} e^{-\frac{\omega^2}{2k_z^2 v_T^2}} .$$

The energy density in a traveling electrostatic plasma wave $E_0 \cos(kx - \omega t)$ is $E_0^2 / 8\pi$; superimposing two such waves to give a standing wave doubles the amplitude and the energy, so the energy density in a standing wave $E_0 \cos kx \cos \omega t$ is $E_0^2 / 16\pi$. In our case, $E_{\max} = k_z A$, so the wave energy in a portion of a cylinder of radius R and length L is

$$W = \frac{1}{16} k_z^2 R^2 L A^2 ,$$

and the amplitude damping rate γ of a plane plasma wave is then given by

$$\frac{\gamma}{\omega} = \frac{1}{2} \frac{P}{\omega W} = \sqrt{\frac{\pi}{8}} \frac{\omega_p^2 \omega}{k_z^3 v_T^3} e^{-\frac{\omega^2}{2 k_z^2 v_T^2}} ,$$

in agreement with the usual expression for Landau damping.[14]

Returning to the finite radius problem, we can perform one more integration analytically by transforming variables

$$v_z , v_\perp \to u , w ,$$

where

$$u = \sqrt{\frac{k}{k_z}} v_\perp , \qquad w = \frac{\omega + k_z v_z}{k v_\perp} , \qquad v_\perp = \sqrt{\frac{k_z}{k}} u ,$$

$$v_z = \sqrt{\frac{k}{k_z}} u w - \frac{\omega}{k_z} , \qquad \frac{\partial (v_z , v_\perp)}{\partial (u , w)} = u ,$$

and

$$v^2 = \left(\frac{k_z}{k} + \frac{k}{k_z} w^2 \right) u^2 - 2 \frac{\omega}{k_z} \sqrt{\frac{k}{k_z}} w u + \frac{\omega^2}{k_z^2} ,$$

and then

$$P = \frac{n_0 \omega^2 e^2 A^2 L}{4 (2\pi)^{1/2} m v_T^5 k^2} e^{-\frac{\omega^2}{2 v_T^2 k_z^2}}$$

$$\times \int_0^R db \int_{-\infty}^{\infty} dw G^2 (kR, kb, w) \int_0^{\infty} du u e^{-\beta u^2 - \gamma u} ,$$

where

$$\beta = \frac{1}{2 v_T^2} \left(\frac{k_z}{k} + \frac{k}{k_z} w^2 \right) , \qquad \gamma = - \frac{\omega}{k_z v_T^2} \sqrt{\frac{k}{k_z}} w .$$

The integral over u can be carried out using the identity[15]

$$\int_0^{\infty} du u e^{-\beta u^2 - \gamma u} = \frac{1}{2\beta} e^{\frac{\gamma^2}{8\beta}} D_{-2} \left(\frac{\gamma}{\sqrt{2\beta}} \right) ,$$

where D is the parabolic cylinder function, which in this case can be expressed in terms of the error function Φ using

$$D_{-2}(z) = e^{\frac{z^2}{4}} \sqrt{\frac{\pi}{2}} \left\{ \sqrt{\frac{2}{\pi}} e^{-\frac{z^2}{2}} - z \left[1 - \Phi \left(\frac{z}{\sqrt{2}} \right) \right] \right\} .$$

The remaining integrations must be carried out numerically; for this purpose it is convenient to make the integration limits finite by changing the integration variable w to ζ:

$$\zeta = \frac{\gamma}{\sqrt{2\beta}} = - \frac{\omega / k_z v_T}{\sqrt{\frac{k_z^2}{k^2} + w^2}} w ,$$

$$w = - \frac{k_z}{k} \frac{\zeta}{\sqrt{\omega^2 / k_z^2 v_T^2 - \zeta^2}} .$$

Then we have

$$dw = - \frac{k_z}{k} \frac{\omega^2 / k_z^2 v_T^2}{\left(\omega^2 / k_z^2 v_T^2 - \zeta^2 \right)^{3/2}} d\zeta ,$$

$$\frac{1}{2\beta} = v_T^2 \frac{k}{k_z} \left(1 - \frac{k_z^2 v_T^2}{\omega^2} \zeta^2 \right) .$$

Combining these results with the above expression for P and letting $x = kb$ gives

$$P = C I \left(kR , \frac{\omega}{k_z v_T} \right) ,$$

where

$$C = \frac{n_0 \omega^2 e^2 A^2 L}{8 m k^3 v_T^3} e^{-\frac{\omega^2}{2 k_z^2 v_T^2}}$$

and

$$I\left(kR,\frac{\omega}{k_z v_T}\right)=\int_0^{kR}dx\int_{-\frac{\omega}{k_z v_T}}^{\frac{\omega}{k_z v_T}}d\zeta$$

$$\times\frac{\sqrt{\frac{2}{\pi}}-\zeta e^{\zeta^2/2}\left[1-\Phi\left(\frac{\zeta}{\sqrt{2}}\right)\right]}{\left(\frac{\omega^2}{k_z^2 v_T^2}-\zeta^2\right)^{1/2}}\,G^2\left[kR,x,w(\zeta)\right].$$

The average energy density of the plasma waves in the cylinder is

$$\left\langle\frac{E^2}{4\pi}\right\rangle_{t,z}=\frac{1}{4\pi}\left\langle(\nabla\phi)^2\right\rangle_{t,z}$$

$$=\frac{A^2}{16\pi}\left[k^2J_0'^2(kr)+k_z^2J_0^2(kr)\right],$$

so the energy in a length L of the cylinder is

$$W=\frac{1}{8}LA^2\int_0^R r\left[k^2J_0'^2(kr)+k_z^2J_0^2(kr)\right]dr\,.$$

Using

$$\int sJ_n^2(s)\,ds=\frac{s^2}{2}\left[J_n^2(s)-J_{n-1}(s)J_{n+1}(s)\right],$$

$$J_0'(s)=J_{-1}(s)=-J_1(s),$$

and the boundary condition $J_0(kR)=0$, we have

$$W=\frac{A^2L}{16}\left(\frac{k_z^2}{k^2}+1\right)(kR)^2J_1^2(kR);$$

thus, the amplitude damping rate is given by

$$\frac{\gamma}{\omega}=\frac{1}{2}\frac{P}{\omega W}=\frac{1}{4\pi}\frac{\omega_p^2\omega}{\left(\frac{k_z^2}{k^2}+1\right)k^3v_T^3(kR)^2J_1^2(kR)}$$

$$\times e^{-\frac{\omega^2}{2k_z^2v_T^2}}I\left(kR,\frac{\omega}{k_z v_T}\right).$$

In terms of the plane-wave Landau result given above, this is

$$\frac{\gamma}{\omega}=\left(\frac{\gamma}{\omega}\right)_{\text{Landau}}$$

$$\times\frac{1}{\sqrt{2\pi^3}}\frac{k_z/k}{1+k^2/k_z^2}\frac{1}{(kR)^2J_1^2(kR)}I\left(kR,\frac{\omega}{k_z v_T}\right).\tag{4}$$

Stimulated Raman Scattering in Filaments

In this section we analyze SRS in filaments using the simple sharp-boundary cylindrical model of the previous section (Fig. 76.44). We determine the filament parameters (radius, etc.) most likely to produce short-wavelength SRS and then estimate the collisionless damping in these filaments using the results of the previous section.

We assume that the pump and backscattered electromagnetic waves propagate as waveguide modes in the filament, so their dispersion relations can be written

$$\omega_0^2=\omega_p^2+c^2\left(k_{0r}^2+k_{0z}^2\right),\tag{5}$$

$$\omega_s^2=\omega_p^2+c^2\left(k_{sr}^2+k_{sz}^2\right),\tag{6}$$

where the subscripts r and z denote the radial and axial wave numbers and the boundary conditions require $J_0\left(k_{0r}R\right)=J_0\left(k_{sr}R\right)=0$, where R is the filament radius. The ponderomotive force arising from the beating of the pump and scattered waves drives an electrostatic plasma response. We assume that this response is largest when the frequency and wave numbers of the plasma wave satisfy the fluid dispersion relation

$$\omega^2 = \omega_p^2 + 3v_T^2\left(k_r^2 + k_z^2\right), \tag{7}$$

where again $J_0\left(k_r R\right) = 0$. This approximation will be good as long as the damping rate is much smaller than the frequency ω. As in the previous section, we assume that the SRS process is near threshold, i.e., the pump replaces the energy lost to damping of the scattered waves, so that the frequencies and wave numbers of all the modes can be taken as real. Then the frequencies and axial wave vectors satisfy the matching conditions

$$\omega_0 = \omega_s + \omega\,, \tag{8}$$

$$k_{0z} = k_{sz} + k_z\,. \tag{9}$$

Coupling between the modes is strongest for the lowest-order (smallest radial wave number) modes;[6] since in this simple model all modes have the same boundary condition $J_0\left(k_{0r} R\right) = J_0\left(k_{sr} R\right) = J_0\left(k_r R\right) = 0$, the strongest coupling is obtained by taking

$$k_{0r} = k_{sr} = k_r = j_{01}/R,$$

where $j_{01} \cong 2.4048$ is the smallest root of J_0.

Light propagates in a waveguide mode in the filament because the density inside the filament, n_0, is lower than that outside, N_0. The difference in plasma pressures inside and outside the filament must be balanced by the ponderomotive force of the light confined in the filament. The required intensity in the filament will be a minimum when the increment in density across the filament boundary is the minimum required to confine the pump wave, or

$$\frac{N_0}{n_c} - \frac{n_0}{n_c} = \frac{c^2 k_{0r}^2}{\omega_0^2}. \tag{10}$$

Since the scattered waves are of lower frequency than the pump, they are also confined to the filament when condition (6) holds.

If we are now given the background temperature T_0, density N_0, and pump wavelength $\lambda_0 = 2\pi c/\omega_0$, Eqs. (5)–(10) are six equations determining the six unknowns $\omega_p^2 = 4\pi n_0 e^2/m$, k_{0z}, k_{sz}, k_z, ω, and R in terms of the scattered-light wavelength $\lambda_s = 2\pi c/\omega_s$. We can solve them numerically to obtain in particular the filament radius and density as a function of SRS wavelength, as shown in Figs. 76.46(a)–76.46(b) for the typical experimental parameters $N_0/n_c = 0.1$, $T_0 = 3$ keV, and λ_0 = 351 nm. The SRS spectrum corresponding to these

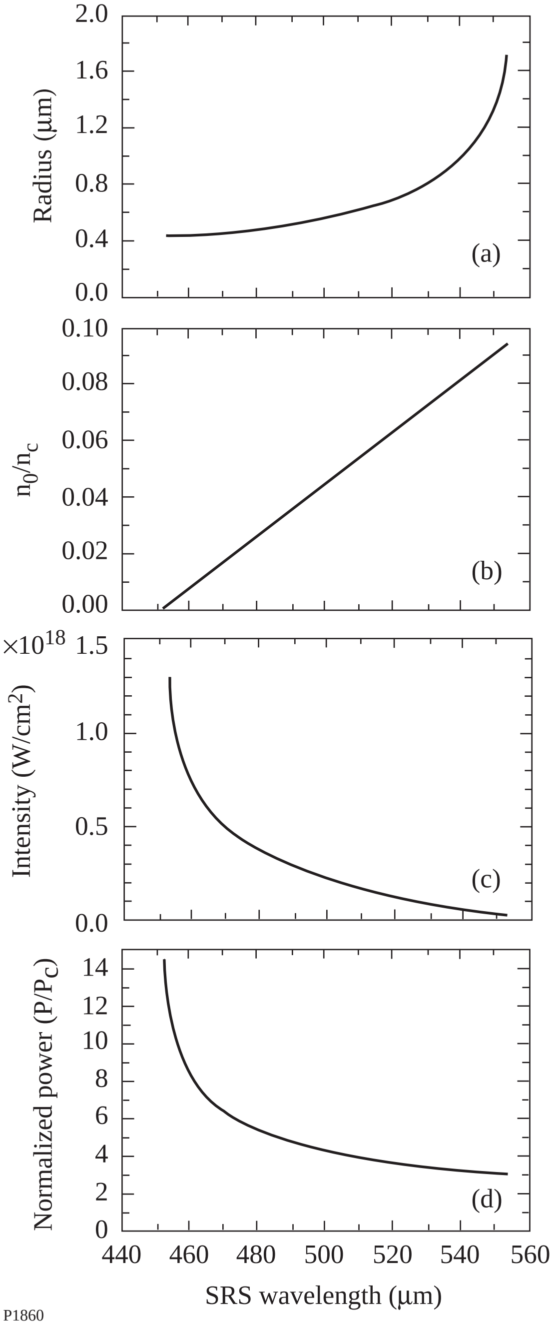

Figure 76.46
Parameters of the filament model as determined in the **Stimulated Raman Scattering in Filaments** section, plotted against the SRS emission wavelength. The filament radius is plotted in (a), the interior density in (b) (for an exterior density of one-tenth critical), the interior light intensity in (c), and the normalized power in the filament in (d).

parameters extends from about 450 nm to about 550 nm. The density plot shows that longer wavelengths would require $N_0/n_c = 0.1$, while shorter wavelengths lead to unphysical negative densities inside the filament. Note that over most of the spectrum the required filament radii tend to be quite small—of the order of a few collisionless skin depths or about a micron for these parameters.

By using the condition that the ponderomotive force balance the difference in plasma pressures inside and outside the filament, we can obtain the intensity and power in the filament. The pressure balance condition is $n_0 = N_0 e^{-v_0^2/4v_T^2}$, where v_0 is the oscillatory velocity of an electron in the electric field of the filament

$$v_0 = eE_{\max}/m\omega_0 \cong 25.6\sqrt{I\left(\mathrm{W/cm^2}\right)}\lambda_0(\mu\mathrm{m})\ \mathrm{cm\ s^{-1}} \qquad (11)$$

with I being the intensity in the filament and λ_0 the laser wavelength. Solving for the intensity yields

$$I\left(\mathrm{W/cm^2}\right) \cong 1.1 \times 10^{13} \frac{T_0(\mathrm{eV})}{\lambda_0^2(\mu\mathrm{m})} \ln\left(\frac{N_0}{n_0}\right).$$

These intensities are plotted in Fig. 76.46(c). Since in our simplified model the intensity is uniform in the interior of the filament, the power in the filament is obtained by multiplying the intensity by πR^2 and is shown in Fig. 76.46(d) as the normalized power P_N (usually denoted by N in the literature;[16] we use the present notation to avoid confusion with the number density). The normalized power is in general defined by

$$P_N \equiv \frac{e^2}{8\pi m \omega_0^2 T_0} \frac{\omega_p^2}{c^2} \iint_A \left|E^2\right| dx dy,$$

where the integration is over the cross-sectional area of the filament.

The normalized power and the filament radius normalized to the collisionless skin depth are useful in comparing our simple filament model with what might be expected of actual filaments. Recently Vidal and Johnston[17] have published some nonlinear simulations of the breakup of laser beams into filaments in plasmas. They find that comparatively long-lived filaments typically tend to form with radii of a few collisionless skin depths and normalized powers P_N in the range of 2 to 15. Larger filaments tend to break up into several smaller filaments within this range; smaller filaments cannot form because of diffraction. From Figs. 76.46(a) and 76.46(d) we see that the filaments our model predicts for short-wavelength SRS have parameters within this range. So we may conclude that, at least in terms of gross parameters such as size and intensity, our model is not an unreasonable representation of the filaments likely to be involved in SRS.

The collisionless damping rate for the plasma mode associated with each SRS wavelength, as calculated in the **Linear Collisionless Damping** section, is shown in Fig. 76.47. For comparison we also show the damping rate for a plasma wave in a homogeneous plasma that would give the same SRS wavelength. Details of the calculation of the damping rate in homogeneous plasmas is given in the Appendix. From Fig. 76.47 we see that for longer wavelengths (corresponding to filaments of large radius) the damping rates approach the homogeneous Landau result, but for shorter wavelengths the smaller radius results in a much-reduced damping as compared to the homogeneous case.

The growth rate for SRS in a filament is readily calculated from the coupled wave equations for the waveguide modes;[6] it is largest when the plasma response is taken to be the fundamental mode (i.e., $k = j_{01}/R$) and is then the same as for a plane-wave pump of the same intensity in a homogeneous plasma. The linear, undamped, homogeneous SRS growth rate γ_0 at high pump intensities is given by[14]

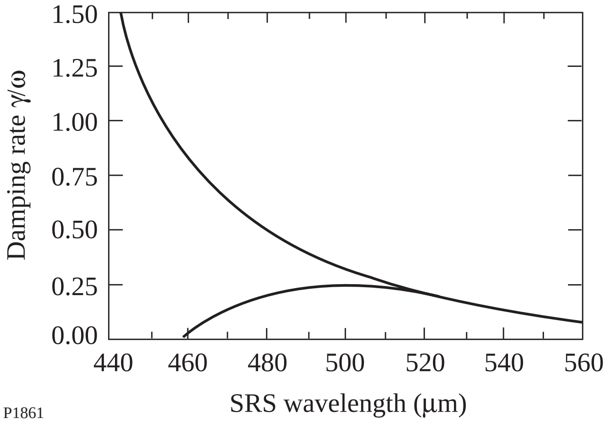

Figure 76.47
Damping rates for plasma waves giving rise to SRS, plotted against the wavelength of the SRS light produced. The upper curve gives the results for a homogeneous plasma, the lower for the filament model in the **Stimulated Raman Scattering in Filaments** section.

$$\frac{\gamma_0}{\omega_0} \cong \sqrt{\frac{\omega_p}{\omega_0}\frac{v_0}{c}}.$$

From Fig. 76.46(c) and Eq. (11) we see that $\gamma_0/\omega_0 \approx 0.1$ in the parameter regime of interest to us. This means that the instability will reach nonlinear saturation within a few tens of laser periods temporally and within a few tens of wavelengths spatially, i.e., the spatial and temporal length scales of the SRS interaction are typically much smaller than those of the filament. This justifies the use of an infinitely long, steady-state filament model to study SRS. The high intensities and low damping within the filament also mean that the SRS threshold arising from damping[14]

$$\gamma_0 > \sqrt{\gamma_e \gamma_s}$$

is greatly exceeded, where γ_e and γ_s are the damping rates of the plasma and electromagnetic waves, respectively. Finally, the comparatively low damping of the plasma wave justifies the use of the plasma-wave dispersion relation for the plasma response in these calculations, since for low damping SRS will dominate stimulated Compton scattering.

Conclusions

Discrepancies have long been noted between observations of SRS and theories premised on relatively homogeneous plasmas and uniform laser irradiation. Foremost among these are the onset of SRS at intensities well below the predicted thresholds and the presence of SRS at short wavelengths, which should in theory be suppressed by Landau damping. Many of these discrepancies can be accounted for if the SRS is actually occurring in high-intensity, self-focused light filaments, but this interpretation is still open to the objection that the short-wavelength scattering requires low plasma densities and thus should still be suppressed by Landau damping. We have shown that if short-wavelength SRS is generated in filaments, the Landau damping of the corresponding plasma waves is greatly reduced relative to the damping that would occur if the SRS were being generated outside the filamentary context. This removes the primary objection to the filamentation hypothesis as the explanation for the anomalous SRS observations and suggests that if filamentation is suppressed, for example, by beam-smoothing schemes intended to improve irradiation uniformity, the SRS instability should then be well described by classical theories. One especially important implication of this is that the effective observational threshold for SRS should be significantly increased if filamentation is suppressed by beam smoothing, so that at NIF intensities, for example, SRS would not be significant.

ACKNOWLEDGMENT

This work was supported by the U.S. Department of Energy Office of Inertial Confinement Fusion under Cooperative Agreement No. DE-FC03-92SF19460, the University of Rochester, and the New York State Energy Research and Development Authority. The support of DOE does not constitute an endorsement by DOE of the views expressed in this article.

APPENDIX: Calculation of Collisionless Damping for SRS in Homogeneous Plasmas

For purposes of comparison with our results for the damping of longitudinal waveguide modes in filaments, we also showed in Fig. 76.47 the corresponding damping rates for plane waves in homogeneous plasmas. Since these damping rates are typically much larger and can be comparable to the real frequency, the use of the usual small-damping approximation[14] to Landau damping is not justified. To calculate these damping rates we therefore use the exact expression for the plasma dielectric response function in a Maxwellian plasma:

$$\varepsilon(k,\omega) = 1 + \frac{1}{(k\lambda_\mathrm{D})^2}\left[1 + \Omega Z(\Omega)\right]; \tag{A1}$$

where

$$\Omega \equiv \frac{\omega}{\sqrt{2}kv_T} = \frac{1}{\sqrt{2}}\left(1 - \frac{\omega_s}{\omega_0}\right)\left(\frac{n_0}{n_c}\right)^{-\frac{1}{2}} \frac{1}{k\lambda_\mathrm{D}}, \tag{A2}$$

and where Z denotes the plasma dispersion function,[18] ω_s is the SRS scattered light frequency, n_0 is the homogeneous plasma electron density, v_T is the electron thermal velocity, λ_D is the Debye length, and n_c is the critical density at the laser frequency ω_0. The normal modes are given by the values of k and ω for which $\varepsilon(k,\omega) = 0$. These are the modes that propagate in the absence of a driver, and for a Maxwellian plasma they are damped, i.e., ω has an imaginary component, corresponding to the Landau damping, and the wave amplitude decreases with time. Here, however, we are interested in the steady-state response of a driven plasma wave, corresponding to the situation where SRS is at threshold; i.e., the power provided by the pump wave (the laser beam) exactly compensates for the power lost to damping. (Once above threshold, the instability grows so rapidly that the damping becomes irrelevant.) The plasma response at a given frequency may then be regarded as a driven damped harmonic oscillator, reaching maximum amplitude at that point in the plasma where $\left|\varepsilon(k,\omega)\right|$ is a minimum. SRS can occur at a range of plasma densities below quarter-critical density. Underdense plasmas typically include such a range of plasma densities but are close to isothermal; thus, we regard the temperature as being fixed and look for the values of n_0/n_c and $k\lambda_d$ that minimize $\varepsilon(k,\omega)$. From (A1) and (A2), since ω_s is known, this minimization provides a relation between the two unknowns n_0/n_c and $k\lambda_d$, which we can write by expressing $k\lambda_d$ as a function of n_0/n_c:

$$k\lambda_{\mathrm{D}}\left(\frac{n_0}{n_c}\right)=x \quad \text{such that}$$

$$\left|\varepsilon\left[x,\Omega\left(x,\frac{n_0}{n_c}\right)\right]\right| \le \left|\varepsilon\left[x',\Omega\left(x',\frac{n_0}{n_c}\right)\right]\right| \quad \text{for all } x', \qquad \text{(A3)}$$

where we have used (A2) to represent Ω as a function of $k\lambda_d$ and n_0/n_c.

We obtain another relation between these unknowns from the dispersion relations of the pump and scattered light waves and the frequency and wave-number matching conditions for SRS:

$$\omega_0^2=\omega_p^2+c^2k_0^2, \qquad \omega_s^2=\omega_p^2+c^2k_s^2;$$
$$\omega=\omega_0-\omega_s, \qquad k=k_0-k_s, \quad k_+=k_0+k_s,$$

where (ω_0,k_0) and (ω_s,k_s) are the frequency and wave number of the pump and scattered EM waves, respectively. Subtracting the two dispersion relations gives

$$\omega_0^2-\omega_s^2=c^2\left(k_0^2-k_s^2\right)=c^2k_+k, \quad \text{so } k_+=\frac{\omega_0^2-\omega_s^2}{c^2k}.$$

Adding the two dispersion relations then yields

$$1+\frac{\omega_s^2}{\omega_0^2}=2\frac{n_0}{n_c}+\frac{1}{2}\left[\frac{c^2k^2}{\omega_0^2}+\frac{\left(1-\frac{\omega_s^2}{\omega_0^2}\right)^2}{\frac{c^2k^2}{\omega_0^2}}\right]. \qquad \text{(A4)}$$

Next we can write

$$\frac{c^2k^2}{\omega_0^2}=\frac{c^2}{v_T^2}\frac{\omega_p^2}{\omega_0^2}\frac{v_T^2k^2}{\omega_p^2}=\left(\frac{v_T^2}{c^2}\right)^{-1}\frac{n_0}{n_c}\left(k\lambda_{\mathrm{D}}\right)^2, \qquad \text{(A5)}$$

and since the temperature, or equivalently v_T, is assumed known, combining (A4) and (A5) gives another relation between $k\lambda_{\mathrm{D}}$ and n_0/n_c, which along with (A3) can be solved numerically to obtain these unknowns and thus determine k. The Landau damping rate, which may also be regarded as the rate of transfer of energy from the wave to the resonant particles, is then given by

$$\frac{\gamma}{\omega}=\frac{1}{2}\,\mathrm{Im}\left[\varepsilon(k,\omega)\right].$$

Using (A1) and the formula for the Z function of a real argument

$$Z(x)=e^{-x^2}\left[i\sqrt{\pi}-2\int_0^x e^{t^2}\,dt\right],$$

this is

$$\frac{\gamma}{\omega}=\sqrt{\frac{\pi}{8}}\,\frac{\omega_p^2\omega}{k^3v_T^3}\,e^{-\frac{\omega^2}{2k^2v_T^2}}. \qquad \text{(A6)}$$

This is the damping rate for SRS in a homogeneous plasma, as plotted in Fig. 76.47. It should be noted that while (A6) is identical to the Landau damping rate usually obtained for normal modes $\left[\varepsilon(k,\omega)=0\right]$ under the assumption of weak damping, for driven modes with ω real it is valid even for strong damping.

REFERENCES

1. J. C. Fernández *et al*., Phys. Plasmas **4**, 1849 (1997).
2. A. Simon, W. Seka, L. M. Goldman, and R. W. Short, Phys. Fluids **29**, 1704 (1986), and references therein.
3. B. J. MacGowan *et al*., Phys. Plasmas **3**, 2029 (1996).
4. D. S. Montgomery *et al*., Phys. Plasmas **3**, 1728 (1996).
5. K. Tanaka, L. M. Goldman, W. Seka, M. C. Richardson, J. M. Soures, and E. A. Williams, Phys. Rev. Lett. **48**, 1179 (1982).

6. R. W. Short, W. Seka, and R. Bahr, Phys. Fluids **30**, 3245 (1987), and references therein.
7. T. Afshar-rad *et al*., Phys. Fluids B **4**, 1301 (1992).
8. R. L. Berger, E. A. Williams, and A. Simon, Phys. Fluids B **1**, 414 (1989).
9. R. W. Short, R. Bingham, and E. A. Williams, Phys. Fluids **25**, 2302 (1982).
10. D. E. Hinkel, E. A. Williams, and C. H. Still, Phys. Rev. Lett. **77**, 1298 (1996).
11. B. B. Afeyan, A. E. Chou, J. P. Matte, R. P. J. Town, and W. L. Kruer, Phys. Rev. Lett. **80**, 2322 (1998).
12. C. Labaune *et al*., Phys. Plasmas **5**, 234 (1998).
13. Laboratory for Laser Energetics LLE Review **75**, 200, NTIS document No. DOE/SF/19460-246 (1998). Copies may be obtained from the National Technical Information Service, Springfield, VA 22161.
14. W. L. Kruer, *The Physics of Laser Plasma Interactions*, Frontiers in Physics, Vol. 73, edited by D. Pines (Addison-Wesley, Redwood City, CA, 1988).
15. I. S. Gradshteyn and I. M. Ryzhik, *Table of Integrals, Series, and Products*, edited by A. Jeffrey (Academic Press, New York, 1980), p. 337.
16. J. F. Lam, B. Lippmann, and F. Tappert, Phys. Fluids **20**, 1176 (1977).
17. F. Vidal and T. W. Johnston, Phys. Rev. Lett. **77**, 1282 (1996).
18. B. D. Fried and S. D. Conte, *The Plasma Dispersion Function* (Academic Press, New York, 1961).

LLE’s Summer High School Research Program

During the summer of 1998, 11 students from Rochester-area high schools participated in the Laboratory for Laser Energetics’ Summer High School Research Program. The goal of this program is to excite a group of high school students about careers in the areas of science and technology by exposing them to research in a state-of-the-art environment. Too often, students are exposed to “research” only through classroom laboratories, which have prescribed procedures and predictable results. In LLE’s summer program, the students experience all of the trials, tribulations, and rewards of scientific research. By participating in research in a real environment, the students often become more excited about careers in science and technology. In addition, LLE gains from the contributions of the many highly talented students who are attracted to the program.

The students spent most of their time working on their individual research projects with members of LLE’s technical staff. The projects were related to current research activities at LLE and covered a broad range of areas of interest including optics, spectroscopy, chemistry, diagnostic development, and materials science (see Table 76.III).

The students attended weekly seminars on technical topics associated with LLE’s research. Topics this year included lasers, fusion, holography, nonlinear optics, global warming, and scientific ethics. The students also received safety training, learned how to give scientific presentations, and were introduced to LLE’s resources, especially the computational facilities.

The program culminated with the High School Student Summer Research Symposium on 26 August at which the students presented the results of their research to an audience including parents, teachers, and LLE staff. The students also prepared written reports, which were bound into a permanent record of their work. These reports are available by contacting LLE.

Ninety-three high school students have participated in the program since it began in 1989. The students this year were selected from approximately 60 applicants.

In 1997, LLE added a new component to its high school outreach activities: an annual award to an Inspirational Science Teacher. This award honors teachers who have inspired High School Program participants in the areas of science, mathematics, and technology and includes a $1000 cash prize. Teachers are nominated by alumni of the High School Program. The 1998 award was presented at the symposium to Mr. David Crane, a chemistry teacher from Greece Arcadia High School. Mr. Crane was nominated by Robert Dick, a participant in the 1991 Program. Mr. Dick wrote that Mr. Crane’s “academic competence, curiosity, and enthusiasm toward teaching allow him to motivate students who would, otherwise, fall through the cracks. Mr. Crane attracted students who wouldn’t typically take difficult science courses.” He added, “Mr. Crane would stay after normal school hours to host an informal lecture and lab, just to satisfy our curiosity.”

Ms. Donna Essegian, principal of Greece Arcadia High School, added, “He is dedicated to his students. ...He is a continuous learner himself and has served this way as a model for students that science is an evolving subject.” Mr. Terry Kessler, an LLE scientist who was taught by Mr. Crane, remembered, “The science teacher tandem at Greece Arcadia High School, consisting of Mr. David Crane (chemistry) and Mr. Claude Meyers (physics), has encouraged many of us to follow our curiosities in science and to pursue lifelong learning.”

Table 76.III: High School Students and Projects—Summer 1998.

Student	High School	Supervisor	Project
Steven Corsello	Pittsford Mendon	K. Marshall	Computer-Aided Design and Modeling of Nickeldithiolene Near-IR Dyes
Peter Grossman	Wilson Magnet	S. Craxton	Group Velocity Effects in Broadband Frequency Conversion on OMEGA
Joshua Hubregsen	Pittsford Sutherland	S. Jacobs	A Study of Material Removal During Magnetorheological Finishing (MRF)
Neil Jain	Pittsford Sutherland	M. Guardalben	Phase-Shifting Algorithms for Nonlinear and Spatially Nonuniform Phase Shifts
Leslie Lai	Pittsford Mendon	M. Wittman	The Use of Design-of-Experiments Methodology to Optimize Polymer Capsule Fabrication
Irene Lippa	Byron-Bergen	K. Marshall	Synthesis of Nickeldithiolene Dyes and Their Solubility in a Nematic Liquid Crystal Host
Phillip Ostromogolsky	Brighton	F. Marshall	Investigation of X-Ray Diffraction Properties of a Synthetic Multilayer
Michael Schubmehl	The Harley School	R. Epstein	An Analysis of the Uncertainty in Temperature and Density Estimates from Fitting Model Spectra to Data
Joshua Silbermann	Penfield	P. Jaanimagi	Automated CCD Camera Characterization
Abigail Stern	The Harley School	J. Knauer	Design and Testing of a Compact X-Ray Diode
Amy Turner	Churchville-Chili	S. Craxton	Ray Tracing Through the Liquid Crystal Point Diffraction Interferometer (LCPDI)

FY98 Laser Facility Report

The OMEGA facility saw substantial improvements in effectiveness at executing experimental objectives for FY98. To extend operations to meet increased demand for shots on OMEGA, UR/LLE hired additional staff to support multishift operations. Starting in May, after training was completed, we began to shoot targets for 12 h each target shot day, three shot days per week. Tailoring the facility operations crew to an uninterrupted 12-h shot shift matches staffing to the routine of OMEGA shot cycles. LLE continues to "block schedule" experiments by week to minimize the number of configuration changes and provide a sufficient run time to mitigate occasional system nonavailabilities.

Advances in individual beam and beam-to-beam uniformity have been a UR/LLE priority for the FY98 period. The technological improvements to the diagnostics—the P510 multichannel streak cameras and amplifier small-signal-gain instrumentation—are two key elements necessary for developing and characterizing power balance between beams. Both systems are currently on-line diagnostics and are being utilized to maintain OMEGA at 3%–4% rms IR beam balance. LLE has also improved the as-built reliability of the power conditioning system by upgrading the high-voltage switches and trigger systems. The decreased pre-fire fault rate has improved target irradiation repeatability substantially from the beam-to-beam uniformity standpoint. Another amplifier performance issue, the premature failure of the flash lamps, has been mitigated through the development of new lamp designs. Approximately 50% of the 6800 lamps are now a higher-reliability "hard seal" configuration.

For single-beam uniformity enhancements, long-lead procurements were initiated in FY98 to fabricate beam-smoothing optics for OMEGA. During FY98 a KDP crystal vendor has been fabricating birefringent wedges for distributed polarization rotator[1] deployment on the 60 beams. LLE anticipates permanently deploying DPR optics on OMEGA in the second quarter of FY99. Perhaps the greatest uniformity improvement to the on-target profile of individual OMEGA beams was the installation of a full complement of 60 ion-etched DPP optics,[2] deployed in January 1998. These optics provide a circularly symmetric and highly repeatable individual beam profile on target which, when combined with SSD, allows OMEGA to approach the individual beam uniformity goals set for the system. Future single-beam uniformity improvements are anticipated to come through increases in SSD modulation frequency and bandwidth. During FY98 a project to frequency convert greater bandwidths with a second-harmonic mixer (KDP) was initiated.

Progress in the experimental area this year included the integration of the sixth and final 10-in. manipulator (TIM) and activation of several new diagnostics. New diagnostic capability for FY98 included activation of two charged-particle spectrometers, a time-resolved flat-field XUV spectrometer, an XUV Cassegrain telescope, an imaging XUV framing camera, a neutron bang-time diagnostic, a streaked optical pyrometer, and new streaked XR spectrometers. Many of these instruments were developed and fielded in conjunction with other organizations, including LLNL, LANL, NRL, MIT, and the University of Maryland. Other improvements in the experimental area include qualification of the facility for use in Stockpile Stewardship Program experiments and numerous enhancements to diagnostic timing command/control.

Many of the minor laser and experimental facility improvements are significantly easier to dovetail into the schedule since the extended shift operations schedule was implemented. Much of the maintenance work previously scheduled on the 0400 shift prior to shots has been moved to the Friday/Monday period, facilitating an earlier availability of the system for shots each day. Table 76.IV summarizes some of the tangible gains made from switching to the extended operations scenario. In conclusion, the shot effectiveness of two weeks of extended operations exceeds the capacity provided by three weeks of the former single-shift schedule. There were a total of 882 target shots in FY98, and it can be expected that the facility will support over 1300 target shots in FY99.

Table 76.IV: OMEGA operations shifted to extended hours in FY98.

	Prior to Extended Operations	Extended Operations
FY98 average number of shots/shot week	17	26
FY98 average number of shots/shot day	5.2	9.8
Average time of day for the first shot	11:47 AM (1/96 to 5/98)	10:20 AM
Total target shots for FY98: 882		

REFERENCES

1. Laboratory for Laser Energetics LLE Review **45**, 1, NTIS document No. DOE/DP/40200-149 (1990). Copies may be obtained from the National Technical Information Service, Springfield, VA 22161; Y. Kato, unpublished notes (1984).
2. Laboratory for Laser Energetics LLE Review **74**, 71, NTIS document No. DOE/SF/19460-241 (1998). Copies may be obtained from the National Technical Information Service, Springfield, VA 22161.

National Laser Users' Facility News

FY98 Experiments

During FY98 progress was made in several NLUF programs: EUV and XUV measurements of early-time plasmas (Hans Griem and Ray Elton, University of Maryland); x-ray spectroscopy of high-density plasmas (Charles Hooper *et al.*, University of Florida); spectral measurements of fusion-reaction charged particles (Richard Petrasso, Massachusetts Institute of Technology); neutron detector calibration (Stephen Padalino, State University of New York at Geneseo); high-resolution imaging of laser targets (John Seely *et al.*, Naval Research Laboratory); and radiation ablation measurements of hohlraum targets (David Cohen, University of Wisconsin).

Figure 76.48 shows a photograph of the installation of a charged-particle spectrometer (CPS 2) developed under LLE funding and now operating on the OMEGA system. CPS 2 is the second of two charged-particle spectrometers fielded by the MIT group on OMEGA. During FY98 the MIT group with funding from NLUF and in collaboration with LLE and LLNL scientists used these spectrometers to measure fusion-product charged particles and high-energy ablator ions. In one series of experiments, fuel temperature and capsule areal density were measured simultaneously by these spectrometers.

In addition to NLUF-supported programs, several indirect-drive target programs, also coordinated through the NLUF Manager, were carried out on OMEGA by groups from LANL and LLNL. These experiments included campaigns on hohlraum symmetry, tetrahedral hohlraums, double-shell capsules, opacity, and point-backlighter tests. Finally, a direct-drive cylinder experiment was fielded by LANL in collaboration with LLE.

FY99 Proposals

Fifteen proposals were submitted to NLUF for FY99. This represents a new record in submissions as well as requested funding (funding requests were more than two-and-a-half times the amount of available funding from DOE—$700,000). A DOE technical evaluation panel chaired by the NLUF Manager and including Dr. Michael Cable (LLNL), Dr. Allan Hauer (LANL), Prof. Tudor Johnston (INRS), and Dr. Ramon Leeper (SNL) reviewed the proposals at a meeting held on 24 April 1998 and recommended approval of nine proposals for funding (see Table 76.V). Twelve graduate students and seven undergraduates will participate in the NLUF programs approved for funding in FY99.

U206

Figure 76.48
Photograph taken during the installation of the second of two charged-particle spectrometers on OMEGA.

Table 76.V: Approved FY99 NLUF Proposals.

Principal Investigator	Affiliation	Proposal Title
D. Cohen	University of Wisconsin, Madison	Development of X-Ray Tracer Diagnostics for Radiatively Driven Copper-Doped Beryllium Ablators
H. Baldis	University of California at Davis	Supenova Hydrodynamics on the OMEGA Laser
H. Baldis	University of California at Davis	Studies of Dynamic Properties of Shock Compressed Solids by *in-situ* Transient X-Ray Diffraction
R. Petrasso	Massachusetts Institute of Technology	Charged-Particle Spectroscopy on OMEGA: First Results, Next Steps
H. Griem	University of Maryland	Soft X-Ray Spectroscopy Measurements of Plasma Conditions at Early Times in ICF Experiments on OMEGA
S. Padalino	SUNY Geneseo	Charged-Particle Spectroscopy on OMEGA: First Results, Next Steps (a joint program with R. Petrasso)
S. Padalino	SUNY Geneseo	Neutron Yield Measurements via Aluminum Activation
C. Hooper	University of Florida	Absorption Spectroscopy, Broadband Emission Survey and the Radiator-Plasma State
B. Afeyan	Polymath Associates	Optical Mixing Controlled Stimulated Scattering Instabilities on OMEGA

Publications and Conference Presentations

Publications

E. L. Alfonso, S.-H. Chen, R. Q. Gram, and D. R. Harding, "Properties of Polyimide Shells Made Using Vapor Phase Deposition," J. Mater. Res. **13**, 2988 (1998).

A. Babushkin, R. S. Craxton, S. Oskoui, M. J. Guardalben, R. L. Keck, and W. Seka, "Demonstration of the Dual-Tripler Scheme for Increased-Bandwidth Third-Harmonic Generation," Opt. Lett. **23**, 927 (1998).

R. Betti, "Beta Limits for the $N = 1$ Mode in Rotating-Toroidal-Resistive Plasmas Surrounded by a Resistive Wall," Phys. Plasmas **5**, 3615 (1998).

M. B. Campanelli and D. J. Smith, "A Wideband Optical Monitor for a Planetary-Rotation Coating System," in *Optical Interference Coatings*, Vol. 9, 1998 OSA Technical Digest Series (Optical Society of America, Washington, DC, 1998), pp. 426–429.

T. J. B. Collins, H. L. Helfer, and H. M. Van Horn, "Accretion Disk and Boundary Layer Models Incorporating OPAL Opacities," Astrophys. J. **502**, 730 (1998).

E. M. Korenic, S. D. Jacobs, S. M. Faris, and L. Li, "Color Gamut of Cholesteric Liquid Crystal Films and Flakes by Standard Colorimetry," Color Res. Appl. **23**, 210 (1998).

S. J. McNaught, J. P. Knauer, and D. D. Meyerhofer, "Photoelectron Initial Conditions for Tunneling Ionization in a Linearly Polarized Laser," Phys. Rev. A **58**, 1399 (1998).

S. Papernov, A. W. Schmid, and D. Zaksas, "Characterization of Freestanding Polymer Films for Application in 351-nm, High-Peak-Power Laser Systems," Opt. Eng. **37**, 677 (1998).

D. J. Smith, J. A. Warner, and N. LeBarron, "Uniformity Model for Energetic Ion Processes Using a Kaufman Ion Source," in *Optical Interference Coatings*, Vol. 9, 1998 OSA Technical Digest Series (Optical Society of America, Washington, DC, 1998), pp. 8–11.

A. R. Staley, D. J. Smith, R. C. Eriksson, and R. P. Foley, "Counter-Rotating Planetary Design Increases Production Capacity for Large Rectangular Substrates," in the *41st Annual Technical Conference Proceedings* (Society of Vacuum Coaters, Albuquerque, NM, 1998), pp. 193–196.

Forthcoming Publications

E. L. Alfonso, S.-H. Chen, R. Q. Gram, D. R. Harding, and F. Y. Tsai, "Fabrication of Polyimide Shells by Vapor Phase Deposition for Use as ICF Targets," to be published in Fusion Technology.

A. Babushkin, J. H. Kelly, C. T. Cotton, M. Labuzeta, M. Miller, T. A. Safford, R. G. Roides, W. Seka, I. Will, M. D. Tracy, and D. L. Brown, "Compact Nd^{3+}-Based Laser System with Gain G_{ss} 10^{13} and 20-J Output Energy," to be published in SPIE's Proceedings of Solid State Lasers for Application (SSLA) to Inertial Confinement Fusion, 3rd Annual International Conference, Monterey, CA, 7–12 June 1998.

R. Betti, V. Lobatchev, and R. L. McCrory, "Feedout, Secular Distortion, and R-T Seeding Induced by Long-Wavelength Perturbations in Accelerated Planar Foils," to be published in Physical Review Letters.

T. R. Boehly, R. L. McCrory, C. P. Verdon, W. Seka, S. J. Loucks, A. Babushkin, R. E. Bahr, R. Boni, D. K. Bradley, R. S. Craxton, J. A. Delettrez, W. R. Donaldson, R. Epstein, D. Harding, P. A. Jaanimagi, S. D. Jacobs, K. Kearney, R. L. Keck, J. H. Kelly, T. J. Kessler, R. L. Kremens, J. P. Knauer, D. J. Lonobile, L. D. Lund, F. J. Marshall, P. W. McKenty, D. D. Meyerhofer, S. F. B. Morse, A. Okishev, S. Papernov, G. Pien, T. Safford, J. D. Schnittman, R. Short, M. J. Shoup III, M. Skeldon, S. Skupsky, A. W. Schmid, V. A. Smalyuk, D. J. Smith, J. M. Soures, M. Wittman, and B.Yaakobi, "Inertial Confinement Fusion Experiments with OMEGA—a 30-kJ, 60-Beam UV Laser," to be published in the Proceedings of the 1997 IAEA Conference, Osaka, Japan, 10–14 March 1997.

T. R. Boehly, A. Babushkin, D. K. Bradley, R. S. Craxton, J. A. Delettrez, R. Epstein, T. J. Kessler, J. P. Knauer, R. L. McCrory, P. W. McKenty, D. D. Meyerhofer, S. Regan, W. Seka, S. Skupsky, V. A. Smalyuk, R. P. J. Town, and B. Yaakobi, "Laser-Uniformity and Hydrodynamic-Stability Experiments at the OMEGA Laser Facility," to be published in Laser and Particle Beams.

S.-H. Chen, B. M. Conger, J. C. Mastrangelo, and A. S. Kende, "Synthesis and Optical Properties of Thermotropic Polythiophene and Poly(P-Phenylene) Derivatives," to be published in Macromolecules.

S.-H. Chen, J. C. Mastrangelo, B. M. Conger, and D. Katsis, "Design, Synthesis, and Potential Application of Glass-Forming Functional Organic Materials," to be published in the Proceedings of the 6th International Polymer Conference, Kusatsu, Japan, 20–24 October 1997 (invited).

T. J. B. Collins, A. Frank, J. E. Bjorkman, and M. Livio, "Supernova 1987A: Rotation and a Binary Companion," to be published in Astrophysical Journal.

T. J. B. Collins, H. L. Helfer, and H. M. VanHorn, "A Model for QPO's in CV's Based on Boundary-Layer Oscillations," to be published in Astrophysical Journal, Letters.

B. M. Conger, J. C. Mastrangelo, D. Katsis, and S.-H. Chen, "Fluorescence of Pyrenyl and Carbazolyl Derivatives in Isotropic and Helically Aligned Solid Films," to be published in the Journal of Physical Chemistry A.

S. Cremer, C. P. Verdon, and R. D. Petrasso, "Tertiary Proton Diagnostics in Future ICF Experiments," to be published in Physics of Plasmas.

M. Currie, R. Sobolewski, and T. Y. Hsiang, "Subterahertz Signal Crosstalk in Transmission Line Interconnects," to be published in Applied Physics Letters.

F. Dahmani, J. C. Lambropoulos, A. W. Schmid, S. J. Burns, and C. Pratt, "Nanoindentation Technique for Measuring Residual Stress Field Around a Laser-Induced Crack in Fused Silica," to be published in the Journal of Materials Science.

F. Dahmani, J. C. Lambropoulos, A. W. Schmid, S. Papernov, and S. J. Burns, "Fracture of Fused Silica with 351-nm-Laser-Generated Surface Cracks," to be published in the Journal of Materials Research.

F. Dahmani, A. W. Schmid, J. C. Lambropoulos, and S. J. Burns, "Laser-Fluence and Laser-Pulse Number Dependence of Birefringence and Residual Stress near Laser-Induced Cracks in Fused Silica," to be published in Applied Optics.

F. Dahmani, A. W. Schmid, J. C. Lambropoulos, and S. J. Burns, "Lifetime Prediction of Laser-Precracked Fused Silica Subjected to Subsequent Cyclic Laser Pulses," to be published in the Journal of Materials Science.

V. N. Goncharov, "Ablation Front Oscillations During the Shock Transit Time," to be published in Physical Review Letters.

K. Green, W. Seka, M. D. Skeldon, R. L. Keck, A. V. Okishev, and R. Sobolewski, "Improving the Microwave Bandwidth of Photoconductive Switches Used in the OMEGA Pulse-Shaping System," to be published in SPIE's Proceedings of Solid State Lasers for Application (SSLA) to Inertial Confinement Fusion, 3rd Annual International Conference, Monterey, CA, 7–12 June 1998.

K. S. Il'in, I. I. Milostnaya, A. A. Verevkin, G. N. Gol'tsman, E. M. Gershenzon, and R. Sobolewski, "Ultimate Quantum Efficiency of a Superconducting Hot-Electron Photodetector," to be published in Applied Physics Letters.

S. D. Jacobs, W. I. Kordonski, and H. M. Pollicove, "Precision Control of Aqueous Magnetorheological Fluids for Finishing of Optics," to be published in the Proceedings of ERMR 1997, Yonezawa, Japan, 22–25 July 1997.

S. D. Jacobs, H. M. Pollicove, W. I. Kordonski, and D. Golini, "Magnetorheological Finishing (MRF) in Deterministic Optics Manufacturing," to be published in the Proceedings of ICPE '97, Taipei, Taiwan, 20–22 November 1997.

D. Katsis, A. W. Schmid, and S.-H. Chen, "Mechanistic Insight into Circularly Polarized Photoluminescence from a Chiral-Nematic Film," to be published in Liquid Crystals.

J. P. Knauer, R. Betti, D. K. Bradley, T. R. Boehly, T. J. B. Collins, V. N. Goncharov, P. W. McKenty, D. D. Meyerhofer, V. A. Smalyuk, C. P. Verdon, S. G. Glendinning, D. H. Kalantar, and R. G. Watt, "Single-Mode Rayleigh-Taylor Growth-Rate Measurements with the OMEGA Laser System," to be published in Physics of Plasmas.

E. M. Korenic, S. D. Jacobs, S. M. Faris, and L. Li, "Cholesteric Liquid Crystal Flakes—a New Form of Domain," to be published in Molecular Crystals and Liquid Crystals.

E. M. Korenic, S. D. Jacobs, S. M. Faris, and L. Li, "Cholesteric Liquid Crystal Transmission Profile Asymmetry," to be published in Molecular Crystals and Liquid Crystals.

M. Lindgren, M. Currie, C. Williams, T. Y. Hsiang, P. M. Fauchet, R. Sobolewski, S. H. Moffat, R. A. Hughes, J. S. Preston, and F. A. Hegmann, "Intrinsic Picosecond Response Times of Y-Ba-Cu-O Superconducting Photodetectors," to be published in Applied Physics Letters.

M. Lindgren, W.-S. Zeng, M. Currie, R. Sobolewski, S. Cherednichenko, B. Voronov, and G. N. Gol'tsman, "Picosecond Response of a Superconducting Hot-Electron NbN Photodetector," to be published in Applied Superconductivity.

J. A. Marozas, "The Cross-Phase Modulation Between Two Intense Orthogonally Polarized Laser Beams Co-Propagating through a Kerr-like Medium," to be published in SPIE's Proceedings of Solid State Lasers for Application (SSLA) to Inertial Confinement Fusion, 3rd Annual International Conference, Monterey, CA 7–12 June 1998.

F. J. Marshall and G. R. Bennett, "A High-Energy X-Ray Microscope for ICF," to be published in the Review of Scientific Instruments.

K. L. Marshall, J. Haddock, N. Bickel, D. Singel, and S. D. Jacobs, "Angular-Scattering Characteristics of Ferroelectric Liquid Crystal Electro-Optical Devices Operating in the TSM and ESM Modes," to be published in Applied Optics.

K. L. Marshall, A. L. Rigatti, G. L. Mitchell, J. A. Pathak, A. R. Staley, and J. A. Warner, "An Aqueous Sol-Gel Coating for Epoxy Surfaces," to be published in Optical Interference Coatings, 1998 OSA Technical Digest.

R. L. McCrory and J. M. Soures, "Status of Direct-Drive Inertial Confinement Fusion Research at the Laboratory for Laser Energetics," to be published in the Proceedings of the 2nd Symposium on Current Trends in International Fusion Research: Review and Assessment, Washington, DC, 10–14 March 1997 (invited).

P. W. McKenty, "Direct-Drive Capsule Requirements for the National Ignition Facility and OMEGA Laser Systems," to be published in Fusion Technology.

P. W. McKenty and M. D. Wittman, "Characterization of Thick Cryogenic Layers Using an Interferometric Imaging System," to be published in Fusion Technology.

B. Nodland and C. J. McKinstrie, "Propagation of a Short Laser Pulse in a Plasma," to be published in Physical Review E.

A. V. Okishev, M. D. Skeldon, and W. Seka, "Multipurpose, Diode-Pumped Nd:YLF Laser for OMEGA Pulse Shaping and Diagnostics Applications," to be published in SPIE's Proceedings on Solid State Lasers for Application (SSLA) to Inertial Confinement Fusion, Monterey, CA, 7–12 June 1998.

R. W. Short and A. Simon, "Collisionless Damping of Localized Plasma Waves in Laser-Produced Plasmas and Application to Stimulated Raman Scattering in Filaments," to be published in Physics of Plasmas.

R. W. Short and A. Simon, "Landau Damping and Transit-Time Damping of Localized Plasma Waves in General Geometries," to be published in Physics of Plasmas.

M. D. Skeldon, A. V. Okishev, R. L. Keck, W. Seka, and S. A. Letzring, "An Optical Pulse Shaping System Based on Aperture-Coupled Stripline for OMEGA Pulse Shaping Applications," to be published in SPIE's Proceedings of Solid State Lasers for Application (SSLA) to Inertial Confinement Fusion, 3rd Annual International Conference, Monterey, CA, 7–12 June 1998.

M. D. Skeldon, R. Saager, and W. Seka, “Quantitative Pump-Induced Wavefront Distortions in Laser-Diode- and Flash-Lamp-Pumped Nd:YLF Laser Rods,” to be published in the IEEE Journal of Quantum Electronics.

V. A. Smalyuk, T. R. Boehly, D. K. Bradley, V. N. Goncharov, J. A. Delettrez, J. P. Knauer, D. D. Meyerhofer, D. Oron, and D. Shvarts, “Saturation of the Rayleigh-Taylor Growth of Broad-Bandwidth Laser-Imposed Nonuniformities in Planar Targets,” to be published in Physical Review Letters.

V. A. Smalyuk, T. R. Boehly, D. K. Bradley, J. P. Knauer, and D. D. Meyerhofer, “Characterization of an X-Ray Radiographic System Used for Laser-Driven Planar Target Experiments,” to be published in the Review of Scientific Instruments.

D. J. Smith, J. A. Warner, N. E. LeBarron, T. J. Kessler, S. LaDelia, J. P. Knauer, D. D. Meyerhofer, D. Oron, and D. Shvarts, “The Development of Ion-Etched Phase Plates,” to be published in Applied Optics.

R. Sobolewski, “Ultrafast Dynamics of Nonequilibrium Quasiparticles in High-Temperature Superconductors,” to be published in Superconducting and Related Oxides: Physics and Nanoengineering III.

E. A. Startsev and C. J. McKinstrie, “Relativistic Ponderomotive Dynamics of a Test Particle in a Plasma,” to be published in Physical Review E.

B. Yaakobi, F. J. Marshall, and D. K. Bradley, “Pinhole-Array X-Ray Spectrometer for Laser-Fusion Experiments,” to be published in Applied Optics.

B. Yaakobi, F. J. Marshall, and D. K. Bradley, “Kα Cold Target Imaging and Preheat Measurement Using Pinhole-Array X-Ray Spectrometer,” to be published in the Review of Scientific Instruments.

B. Yaakobi and F. J. Marshall, “Imaging the Cold, Compressed Shell in Laser Implosions Using the Kα Fluorescence of a Titanium Dopant,” to be published in the Journal of Quantitative Spectroscopy and Radiative Transfer.

L. Zheng and D. D. Meyerhofer, “Self- and Cross-Plate Modulation Coefficients in a KDP Crystal Measured by a Z-Scan Technique,” to be published in the Journal of the Optical Society of America B.

J. D. Zuegel and W. Seka, “Upconversion and Reduced $^4F_{3/2}$ Upper-State Lifetime in Intensely Pumped Nd:YLF,” to be published in Applied Optics: Lasers, Photonics, & Environmental Optics.

Conference Presentations

S. J. McNaught and D. D. Meyerhofer, “Precision Measurement of Electron Initial Conditions for Tunneling Ionization in an Elliptically Polarized Laser,” Sixteenth International Conference on Atomic Physics, Windsor, Ontario, Canada, 3–7 August 1998.

D. T. Goodin, N. B. Alexander, I. Anteby, W. A. Baugh, G. E. Besenbruch, K. K. Boline, L. C. Brown, W. Engli, J. F. Follin, C. R. Gibson, D. R. Harding, E. H. Hoffmann, W. Lee, L. Lund, J. E. Nasise, A. Nobile, K. R. Schultz, and R. Stemke, “Status of the Design and Testing of the OMEGA Cryogenic Target System (OCTS),” 20th Symposium on Fusion Technology, Marseille, France, 7–11 September 1998.

The following presentations were made at the 1998 Applied Superconductivity Conference, Palm Springs, CA, 13–18 September 1998:

R. Adam, R. Sobolewski, W. Markowitsch, C. Stockinger, W. Lang, J. D. Pedarnig, and D. Bauerle, “Time and Temperature Evolution of the Photodoping Effect in Y-Ba-Cu-O Josephson Junctions and Thin Films.”

R. Adam, M. Currie, R. Sobolewski, O. Harnack, and M. Darula, “Subpicosecond Measurements of Y-Ba-Cu-O Josephson Junction and Microbridge Integrated Structures.”

M. Currie, D. Jacobs-Perkins, R. Sobolewski, and T. Y. Hsiang, “Subpicosecond Measurements of Single-Flux-Quantum Pulse Interactions.”

M. Currie, D. Jacobs-Perkins, R. Sobolewski, and T. Y. Hsiang, "High-Frequency Crosstalk in Superconducting Microstrip Waveguide Interconnects."

K. S. Il'in, I. I. Milostnaya, A. A. Verevkin, G. N. Gol'tsman, M. Currie, and R. Sobolewski, "Quantum Efficiency and Time-Domain Response of NbN Superconducting Hot-Electron Photodetectors."

The following presentations were made at the CEA-DOE Meeting, Bruyeres-le-Chatel, France, 14 September 1998:

R. L. McCrory, "The LLE Program Tests Critical Concepts of the Direct-Drive Ignition Demonstration Effort."

D. D. Meyerhofer, "Charged Particle Spectrometer (CPS) as Core Diagnostic for OMEGA Implosions."

W. Seka, "Beam Smoothing and Laser Imprinting."

The following presentations were made at the XXX Annual Symposium on Optical Materials for High Power Lasers, Boulder, CO, 28 September–1 October 1998:

F. Dahmani, J. C. Lambropoulos, S. Burns, S. Papernov, and A. W. Schmid, "How Small Stresses Affect 351-nm Damage Onset in Fused Silica."

O. M. Efimov, L. B. Glebov, S. Papernov, A. W. Schmid, and E. Van Stryland, "Laser-Induced Damage of Photo-Thermo-Refractive Glasses for Optical Holographic Elements Writing."

A. L. Rigatti, D. J. Smith, A. W. Schmid, S. Papernov, and J. H. Kelly, "Damage in Fused-Silica Spatial-Filter Lenses on the OMEGA Laser System."

D. J. Smith, J. A. Warner, N. LeBarron, and S. LaDelia, "Production of Distributed Phase Plates Using an Energetic Ion Process."

UNIVERSITY OF
ROCHESTER